STUDIA
UNIVERSITATIS BABEŞ-BOLYAI

PHYSICA

(40)2

1995

CLUJ-NAPOCA

Anul XL 1995

STUDIA
UNIVERSITATIS BABEŞ-BOLYAI

PHYSICA

2

Editorial Office 3400 CLUJ-NAPOCA str M Kogălniceanu nr 1 Telefon 196681

CONTENTS







STUDIA UNIVERSITATIS "BABES-BOLYAI", PHYSICA, XL, 2, 1995

PARAMAGNETIC CENTERS INDUCED BY GAMMA IRRADIATION IN B_2O_3-GeO_2 GLASSES

M PETEANU[1], L COCIU[1], I ARDELEAN[1]

ABSTRACT Borogermanate glasses of the system B_2O_3-GeO_2 subjected to gamma irradiation, were studied by means of EPR Irradiation induced centers, revealing structural and compositional details of the matrix were detected Both electron- and hole-centers were identified. These are electron trapped at a hydrogen compensated germanium ion centers, boron oxygen hole centers; electron trapped at an oxygen vacancy centers

Introduction The scientific interest concerning the structure of borogermanate glasses is justified by their technical applications [1, 2] The system B_2O_3-GeO_2 was less studied The purpose of our research was to prepare stable vitreous matrices corresponding to this system, to check its structural stability when subjected to irradiation, and to improve its properties if the detected structural damages would be too large The investigation technique was EPR.

Our results concerning the paramagnetic centers detected in irradiated borogermanate glasses by means of EPR, and the revealed compositional and structural details, are reported as follows.

Experimental. Glasses of the system B_2O_3-GeO_2 were prepared by melting the corresponding oxide mixtures in an electric heated furnace, at 1250°C. Sintercorundum crucibles were used After 0 5 h of stabilizing at this temperature, the molten material was rapidly quenched in air, on a stainless-steel plate. Typical glasses, in both aspect and structure were obtained The X-rays diffraction analysis did not show any crystalline phase.

Irradiation was performed at room temperature by using a ^{60}Co unit.

EPR absorption spectra were detected at room temperature by using a JES-3B equipment, in X-frequency band, and 100 kHz field modulation.

Results and discussion. Prior to irradiation the studied samples did not show any EPR absorption

The spectral structures detected after irradiations by means of EPR, are well resolved complex ones and, as will be pointed out latter, may be regarded as a superposition of several

[1] *Babeş-Bolyai University, Faculty of Physics, 3400 Cluj-Napoca, Romania*

contributions

Defect formation occurs at low γ doses suggesting ionization processes

The EPR absorption spectrum corresponding to a sample irradiated at about $15 \cdot 10^6$ Gy is presented in Fig 1 There are the marginal lines of a hyperfine doublet (1), and a central set of sharper lines (2), partially covered by a very intense absorption line (3) By comparing the EPR parameter values (line height, linewidth, intensity, g factor values, etc) and the shape of the absorption line composing the spectrum, it was possible to made distinction between these types of spectra superimposed in the final pattern The lines of the doublet (1) are separated at about 120 G, and differ in shape, suggesting that hyperfine anisotropy contributes significantly to the observed broadening The corresponding g tensor is axial, and the calculated values are $g_{\parallel} = 2.0006$ and $g_{\perp} = 1\ 9987$. The sharper central lines (2), separated at about 14 G, are components of a hyperfine structure due to interactions with the nucleus of boron atom. This structure overlaps with the wings of the intense central line (3), which is a characteristic pattern for a center with S = 1/2, and an axially symmetric g tensor having the values $g_{\parallel} = 2\ 0033$ and $g_{\perp} = 1\ 9976$

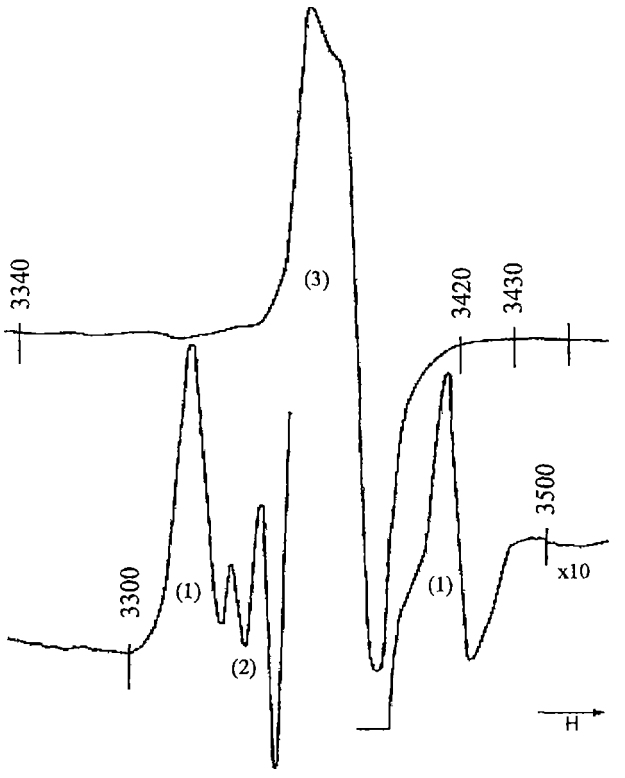

Fig. 1 EPR absorption pattern of B_2O_3-GeO_2 glasses after γ irradiation at a dose of $15 \cdot 10^6$ Gy

This distinction was also pointed out by the specific evolution of the absorption lines as increasing the dose of irradiation, and during a thermal treatment in a bleaching experiment The evolution of the EPR absorption pattern as rising the irradiation dose was followed with respect to that of a "standard" sample This was a fragment of the investigated glass previously subjected to irradiation ($4\ 5 \cdot 10^6$ Gy), and preserved as reference Another fragment was progressively

irradiated and after each stage of irradiation its spectrum was line-by-line compared to that of the standard, simultaneously recorded The resulted evolutions are presented in Fig 2. According to the diagrams in Fig 2 the absorptions (1) and (3) tend to saturate after a dose of $6 \cdot 10^6$ Gy, while the absorptions (2) did not reach saturation even at a dose of $15 \cdot 10^6$ Gy

When thermal treated, the absorptions corresponding to (2) disappear after 250°C, and those corresponding to (3) disappear at annealing temperatures of about 270°C.

The paramagnetic centers giving rise to the above mentioned EPR absorptions, were identified as

(1) - an electron trapped by the Ge atom, interacting with the nucleus of a charge compensating hydrogen

The hydrogenic origin of a 119 G hyperfine doublet observed in a variety of irradiated vitreous silica samples was proved by Vitko [3] by using various means of deuteration. The most satisfactory model suggested by his study attributes the 119 G doublet to an electron trapped at a hydrogen-compensated substitutional germanium impurity The compensating hydrogen might not be present at the defect site prior to irradiation but subsequently migrates there The case of a fourfold coordinated Ge^{4+} substitutional for Si, was studied by Weil [4], the charge compensation being supplied by two alkali or two hydrogen ions Irradiation results in the formation of $Ge^{3+}H^+$ (H^+) with g values of 2 00115, 1 99623, 1 99456 respectively and a large temperature dependent H hyperfine splitting Such defects involving large hydrogen hyperfine splitting may explain the 119 G doublet [3].

In our glasses H ion could be nearer the Ge^{4+} with a larger resulting hyperfine splitting

(2) - the boron oxygen hole center having the characteristic hyperfine structure due to boron, giving rise to a four-line spectrum

In low alkali borates trapped hole centers were found to be stable at room temperature. These yield a "five line plus a shoulder" spectrum [5], synthesized by Griscom et al [6] using $g_1 = 2\,002$, $g_2 = 2\,010$ and g_3 showing a distribution about 2 035 The model of the so called boron-oxygen-hole-center consistent with these parameters and with the associated ~10 G hyperfine coupling constant was a hole trapped at a bridging oxygen connecting a three-coordinated boron with a four-coordinated one [5, 6]. As the alkali content rised above 25 mol % the five-line plus a shoulder spectrum turned into a four-line spectrum assigned by Lee and Bray [7] to a hole on a (BO_4) oxygen as distinct from a bridging oxygen Griscom [8] showed that both four-line and five-line spectra can be synthesized using spin Hamiltonians differing in minor ways (the g_1 value and the width of the g_3 distribution function) This implies that a single center perturbed progressively by environmental changes might be responsible for both spectra.

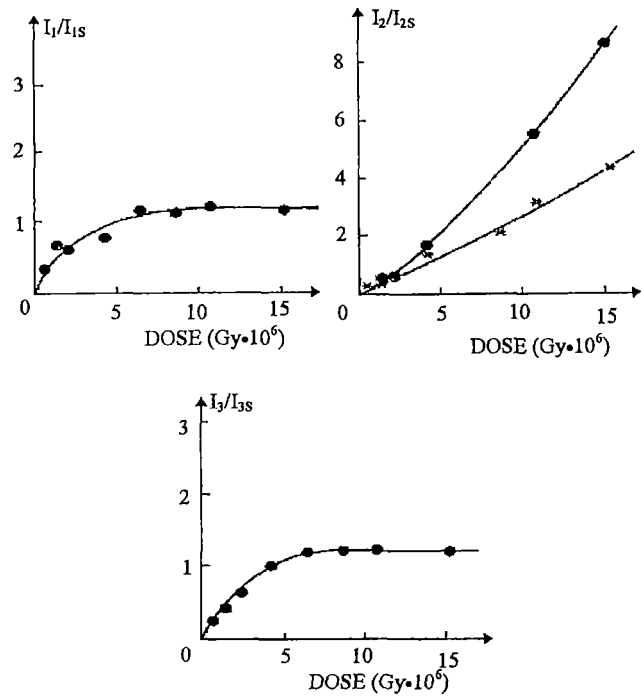

Fig. 2. Defects formation dependence on the dose of irradiation. The intensity of each absorbtion line was related to a corresponding line in a "standard" spectrum chosen as reference

The structure labeled (2) in our spectra was identified as a four line BOHC by comparing it with the spectrum corresponding to an irradiated borate glass. The similarity was evident in both shape and hyperfine splitting of the two spectra.

(3) - the GeE' defect having the unpaired electron at a nonbridging orbital of Ge with an oxygen vacancy

The paramagnetic state of GeO_2 in glass and the powdered crystalline phases, after irradiation, were investigated by Weeks and Purcell [9, 10] A characteristic powder pattern for a center with S = 1/2 and an axially symmetric g tensor, having $g_{\parallel} = 2\ 0016$ and $g_{\perp} = 1.9957$ was detected as being characteristic to all glass and hexagonal crystal-phase specimens for irradiations at room temperature. It was proposed the model of an electron trapped at an oxygen vacancy [9] It was assumed that only one of the sp^3 hybrid orbitals of Ge at an oxygen vacancy furnishes the trapping level, that is, the overlap of the sp^3 orbital from the other Ge ion is small Thus, the g tensor at a trapped electron (S = 1/2) should be axial and $g_{\parallel}$ approximately equal to the free electron g value

The axial symmetry and the values of $g_{\parallel}$ for the experimentally detected line of our samples, agree resonably with the previously reported data [9, 10]

According to diagrams in Fig 2 the Ge-involving centers reach rapidly their maximum concentration in the matrix during irradiation The B-involving ones accumulate progressively when prolonged the irradiation process

Defect formation was inhibit by small amounts of paramagnetic ions, namely Cu^{2+}, dissolved into the matrix [12] Both boron and germanium environments were strongly influenced Because of the gradual removal of the four-coordinated borons and of the oxygen vacancies when

Cu^{2+} progressively enter the matrix, the concentration of the paramagnetic centers induced by irradiation diminished rapidly, until their total disappearance

Conclusions. Prior to irradiation the samples corresponding to the B_2O_3-GeO_2 vitreous system did not show any EPR absorption

The EPR spectra detected after γ irradiation are typical for the irradiation-induced paramagnetic defects, in both shape and EPR parameter values

Defect formation occurs at low γ doses suggesting ionization processes

The structure of the recorded spectra is a complex one, and may be interpreted as a superposition of contributions These are due to several types of paramagnetic centers

The hyperfine doublet of lines separated at about 120 G was identified as arising from an electron trapped at a hydrogen compensated germanium ion center, evidencing amounts of dissolved hydrogen in our samples

The sharp central hyperfine structure was identified as being a four-line boron oxygen hole center, after comparisons with the absorptions due to a γ-irradiated borate system

The central intense line is due to the GeE' paramagnetic center, arising as electron trapped at an oxygen vacancy.

REFERENCES

1 Y Dimitriev, E Kashchieva, M Koleva, J Mat Sci 16, 3045 (1981)
2 Y Dimitriev, V.Dimitrov, E Gatev, E Kashchieva, H Petkov, J Non-Cryst Solids 95&96, 937 (1987)
3 J Vitko Jr , J Appl Phys. 49(1), 5530 (1978)
4 J A Weil, J. Chem. Phys 55, 4685 (1975)
5 S Lee, P J Bray, J. Chem Phys 39, 8863 (1963)
6 D L Griscom, P C.Taylor, D A Ware, P J Bray, J. Chem Phys 48, 5158 (1968)
7 S Lee, P J Bray, J Chem Phys 40, 2982 (1964)
8 D L Griscom, J Non-Cryst. Solids 13, 251 (1973)
9 R A Weeks, T.Purcell, J Chem. Phys 43, 483 (1965)
10 T Purcell, R A Weeks, Phys Chem. Glasses 10, 198 (1969)
11 H Kawazoe, J. Non-Cryst. Solids 71, 231 (1985)
12 M.Peteanu, L Cociu, I Ardelean, J Mat Sci Technol 11, 1 (1995)

STUDIA UNIVERSITATIS "BABES-BOLYAI", PHYSICA, XL, 2, 1995

ELECTRON PARAMAGNETIC RESONANCE OF Mn^{2+} IONS IN Bi_2O_3-GeO_2 GLASSES

M. PETEANU,[1] I. ARDELEAN[1], S. FILIP[2], I. TODOR[1], G. SALVAN[1],

ABSTRACT. Structural details of bismuth-germanate glasses of the Bi_2O_3-GeO_2 system were investigated by means of the EPR of Mn^{2+} ions within a large range of concentrations The paramagnetic ions distribution in the matrix, as involved in several types of structural units, revealed isolated ions entering the matrix in low-symmetric vicinities, and complex clusterized aggregates of manganese A great structural stability of the matrix in accumulating MnO was evidenced

Introduction. When EPR absorptions are detected in oxide vitreous systems containing manganese, these are due to Mn^{2+} ($3d^5$, $^6S_{5/2}$) paramagnetic ions Generally, at low impurifying levels, Mn^{2+} enter the system as involved in structural units building the network thus ordering the matrix in their vicinity In such cases the dopant ions are magnetically isolated When the structural units involving Mn^{2+} are structurally alike to each other, the hyperfine structure (hfs) due to the interaction with the nuclear spin ($I = 5/2$) is well resolved The resolution is preserved when the individual width of components of the hyperfine sextet does not exceed the separation between them The ligand field fluctuations cause the components broadening and consequently the loosing of resolution Another mechanism of the absorption line broadening is the dipolar interaction, which increases with the paramagnetic ions concentration increasing

Over a certain concentration range the network sites available for such isolated impurities are occupied, so the next manganese enter the matrix as network modifier The involved structures are more complicated and become clustered formations of ions at higher concentrations. During the dopant ions accumulation in the vitreous matrix, the initially accepted ions vicinities deteriorate, the hfs resolution is compromised, and the absorption line is progressively overlapped by the large envelope resulted from all contributions

Depending on the glass composition, the structural units containing Mn^{2+} may be highly symmetric giving absorptions centered at $g \cong 2.0$ values In the spin hamiltonain the Zeeman term is the principal one, all other acting as perturbations Such absorptions characterize the spectrum of Mn^{2+} ions in alkali-borate systems, they are intense and show a well resolved hfs [1-6]

[1] *"Babes-Bolyai" University, Faculty of Physics, 3400 Cluj-Napoca, Romania*
[2] *University of Oradea, Department of Physics, 3700 Oradea, Romania*

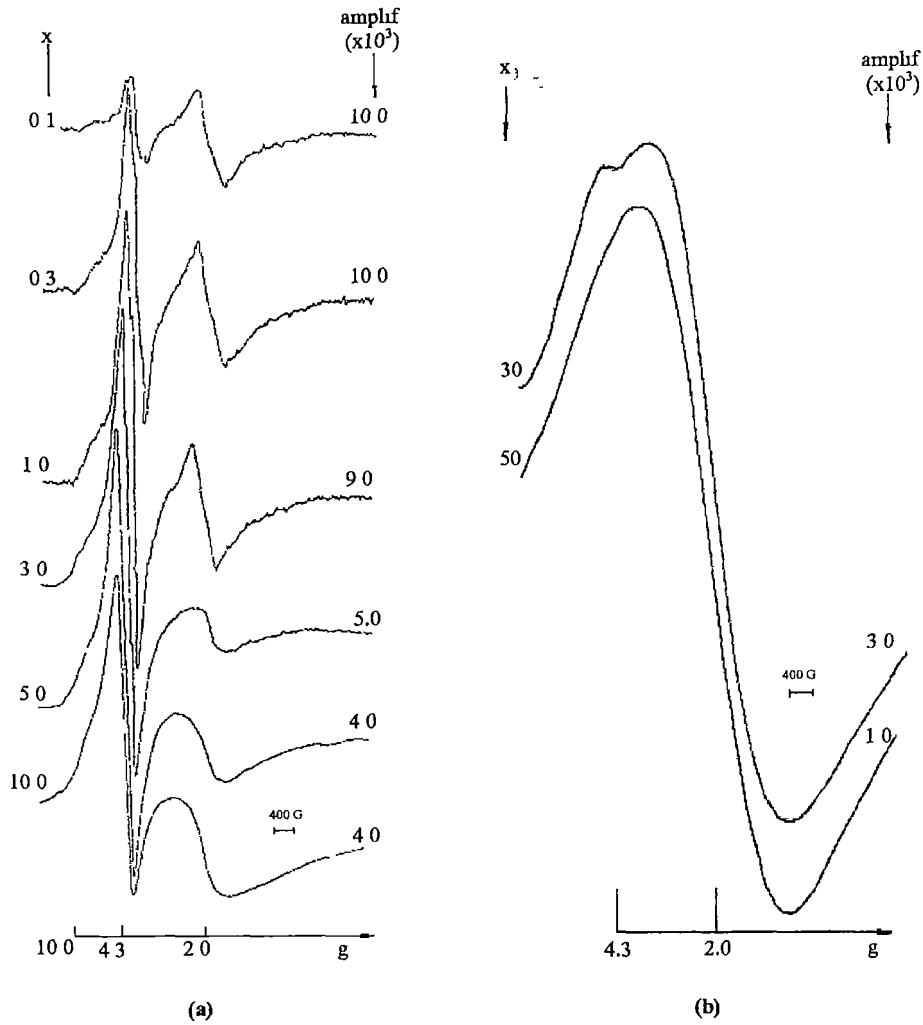

Fig 1 Spectral features of the EPR absorption of Mn^{2+} in xMnO (1-x)[Bi_2O_3 GeO_2] glasses at low content (a) and high content (b) of manganese

The distorted versions of these structural units may also be involved, and for the very distorted vicinities the absorptions centered at g ≅ 4 3 values arise There are several low-symmetric vicinities giving rise to such absorptions [7] The theoretical approach for these resonances accounts for the strong ligand field effects In the spin hamiltonian describing the Mn^{2+} state, the term corresponding to the crystalline field interaction is taken as principal, the others, including the Zeeman one, act as perturbations [8-11] The hfs of the g ≅ 4 3 absorption was reported in chalcogenide glasses [12-14] Schreurs [9] was the first to observe the hfs resolved at absorptions with g >>2.002, in oxide vitreous matrices having a complex

composition In tellurite systems previously investigated by us [15, 16] we detected intense absorptions at g ≅ 4 3 having the hfs very well resolved, on a short concentration range Their width and intensity abruptly decreased for x > 1 mol % MnO. Interesting results concerning the local structure of the magnetically active Mn^{2+} centers in halide and chalcohalide glasses were recently obtained [17-19]

In the past few years glass systems based on heavy-metal oxides (bismuth and/or lead) were investigated [20]. They are characterized by high density, high refractive index, high thermal expansion, low transformation temperature and excellent infrared transmission Since the network bond strengths of heavy-metal oxide glasses are relatively weak compared to those of silicate and borate glasses, the glass forming regions are comparatively limited [20-22] Nakamura et al investigated the magnetic properties of the rapidly quenched samples from the Bi_2O_3-Li_2O-Fe_2O_3 [23] and Bi_2O_3-CuO-Fe_2O_3 [24] systems Dimitriev and Mihailova [25] investigated the glass formation in the binary systems Bi_2O_3-CuO, Bi_2O_3-MnO and Bi_2O_3-TiO_2 The glass formation and magnetic properties of xMO (1-x)[Bi_2O_3 PbO] with M = Cu, Fe, Mn or Cr [26-29] and xCuO (1-x)[Bi_2O_3 GeO_2] [30] glasses, were also investigated by Ardelean et al

We report in this paper the EPR studies of xMnO·(1-x)[Bi_2O_3·GeO_2] glasses with 0 < x ≤ 50 mol % in order to obtain further informations about the manganese ions distribution in oxide glasses.

Experimental. Glasses of the system xMnO (1-x)[Bi_2O_3·GeO_2] were prepared by using reagent grade oxides, within a large concentration range, i e 0 1 ≤ x ≤ 50 mol % The oxide mixtures were molten in sintered corundum crucibles, at 1250°C, in an electrically heated furnace. The molten material was homogenized at this temperature during 10 minutes, then quenched at room temperature on a stainless steel plate Typical glasses were obtained

EPR measurements were performed at room temperature by using a JES-3B spectrometer, in the X frequency band, and 100 kHz field modulation. Powdered samples were studied in tubular sample-holders of the same calibre Identical quantities of sample were investigated

Results and discussions. Glasses of the system xMnO (1-x)[Bi_2O_3 GeO_2] were investigated by means of EPR in a large concentrations range, namely 0 1 ≤ x ≤ 50 mol % The detected absorptions, due to Mn^{2+} ions, are presented in Fig 1. The EPR spectrum consists mainly in absorptions centered at g ≅ 4 3 and g ≅ 2 0 values, their prevalence

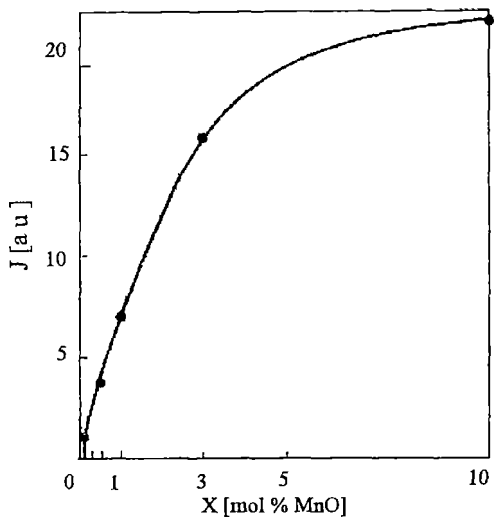

Fig 2 The line-intensity dependence on the manganese content of the sample, for absorptions at g ≅ 4 3

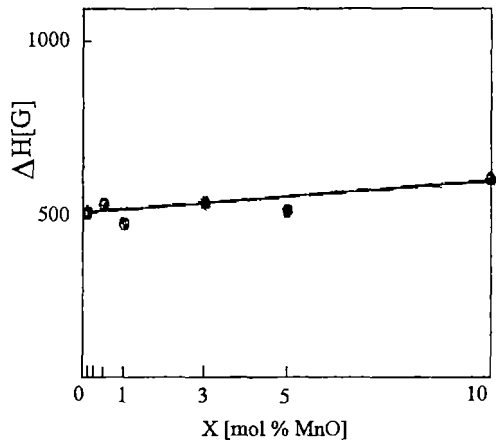

Fig. 3. The line-width evolution of the absorptions at g ≅ 4 3 with the MnO content of the sample

depending on the manganese content of the sample This spectral structure corresponding to lower MnO content, reduces to a single absorption line at the upper limit of the investigated concentration range (Fig. 1 b).

According to Fig 1 a. at low manganese content (0 1 ≤ x ≤ 1 mol % MnO) the characteristic hfs is well resolved for the g ≅ 4.3 absorption. The resolution is loosed when increasing concentration due to the already mentioned broadening mechanisms The separation between the hfs lines increases progressively with the magnetic field, suggesting second order effects to be taken into account in an accurate theoretical approach The hyperfine constant seems to be less affected by the concentration variations within 0 1 ≤ x ≤ 10 mol % MnO

No hfs was detected at absorptions centered at g ≅ 2 0

The EPR parameters of the absorption line, i.e the line-height I, the line-width ΔH, and the intensity approximated as $J = I(\Delta H)^2$, also depend on the MnO content of the sample Their evolution is plotted in Figs 2 to 5 According to Figs 2 and 4 there is a good correlation between the intensities variation of the two absorbtion lines allowing us to follow the Mn^{2+} ions distribution in specific structural units Up to 3 mol % MnO the intensity of the g ≅ 4 3 absorption increases almost linearly This increasing attenuates for x > 3 mol % but the absorption line is still intense and well resolved even after 10 mol % MnO being completely removed only for x>30 mol % MnO (Fig 1 b).

Contrarily to this evolution, the absorption at $g \cong 2\,0$ increases very slowly in the $0\,1 \leq x \leq 3$ mol % concentration range. This increasing is more pronounced after 5 mol % MnO, and appreciable for $x > 10$ mol % MnO, as may be seen in Fig. 4

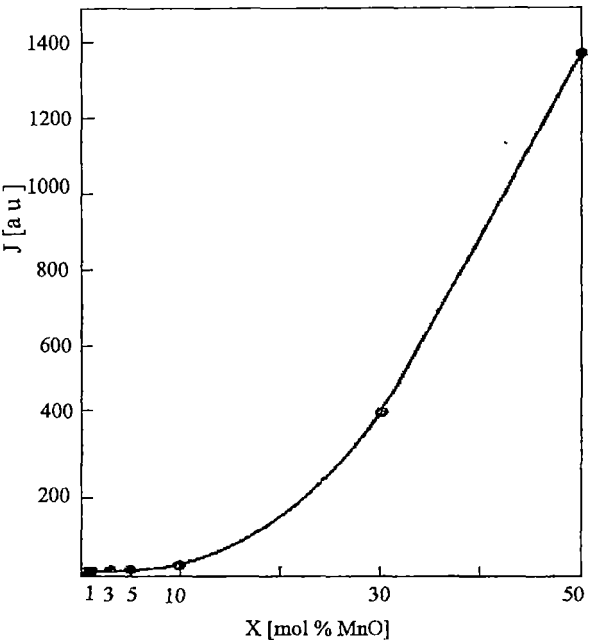

Fig. 4. Line-intensity evolution for the $g \cong 2.0$ absorptions of Mn^{2+} ions in $xMnO\ (1-x)[Bi_2O_3 \cdot GeO_2]$ within $0\,1 \leq x \leq 50$ mol %

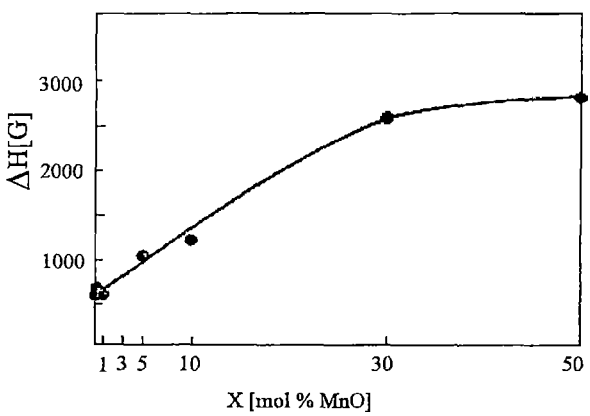

Fig 5. Line-width dependence for the $g \cong 2\,0$ absorptions of Mn^{2+} ions in $xMnO\ (1-x)[Bi_2O_3\ GeO_2]$ vitreous matrices, within $0\,1 \leq x \leq 50$ mol %

The line-width of the $g \cong 4\,3$ absorption is practically independent on concentration (Fig 3), whereas that corresponding to the $g \cong 2\,0$ absorption increases with the MnO content in the sample. The slope of this increasing changes for $x > 30$ mol % MnO due to narrowing effects (Fig 5)

The relative weight of the two absorptions in the spectrum is given in Fig.6 by comparing their intensities at various concentrations. This may give informations on the relative weight of the structural units involving Mn^{2+} as vicinities specific for the $g \cong 4\,3$ and $g \cong 2.0$ absorptions

According to the previously mentioned considerations the $g \cong 4\,3$ absorptions are due to magnetically isolated Mn^{2+} ions, in distorted sites of low-symmetry The features of these absorptions and their evolution when Mn^{2+} ions accumulate in the studied matrix pointed out a great similitude in structure and symmetry of the aggregates involving manganese Consequently the hfs

characte-ristic to Mn^{2+} is very well resolved up to 1 mol % MnO The spectrum preserve the same structure along a wide range of concentration, the g ≅ 4.3 absorption remaining clearly resolved, and distinct from that at g ≅ 2 0, and its width practically does not depend on concentration The structural stability of the matrix at the progressive doping with manganese was revealed as a distinct characteristic of the investigated system.

The g ≅ 2 0 absorption being a broaden structureless line may be attributed to Mn^{2+} ions involved in clustered formations Their distribution in such sites becomes more important after the complete occupancy of the previous discussed ones, i e for compositions having x > 10 mol % MnO. This may be observed in Figs. 2, 4 and 6 which evidence a perfect correlation in evolution of intensities corresponding to the two absorptions, at different steps of the matrix doping One may follow, consequently, the distribution of paramagnetic ions in structural aggregates composing the matrix, when concentration increases within the investigated range At the upper limit of this, the major contribution is due to formations resulted as dopant ions agglomerations into the matrix The slight narrowing of the absorption line (Fig 5) suggests exchange mechanisms to be taken into account for such compositions involving clusterized ions

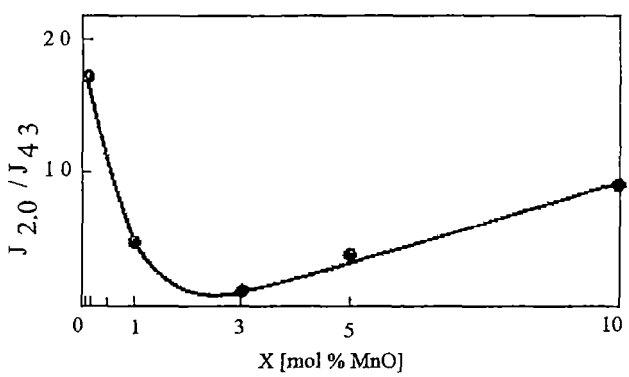

Fig. 6 Concentration dependence of the Mn^{2+} ions distribution on sites specific to the two EPR absorptions, at g ≅ 4 3 respectively g ≅ 2 0

Conclusions. Glasses of the system xMnO (1-x)[Bi_2O_3 GeO_2] show EPR absorption spectra due to Mn^{2+} ions, in a large range of concentra-tions, i.e 0 1≤ x ≤ 50 mol % MnO

Up to x = 10 mol % manganese enter the matrix as involved in structural units where strong ligand-field effects are preponderant This results in g ≅ 4 3 absorptions characte-ristic for isolated ions in low-symmetric sites There is a great structural stability of the matrix in accumulating Mn^{2+} ions in such positions, attested by the wide compositional range in which the g ≅ 4 3 absorptions show intense and well resolved traces

Within the low concentrations range the characteristic hfs due to the interaction with the nuclear spin I = 5/2 is very well resolved at the g ≅ 4 3 line, due to the great structural

similarity of the aggregates involving manganese Ligand field fluctuations in the Mn^{2+} vicinity alter the hfs resolution for x > 1 mol % MnO

Broaden, unresolved lines were detected at g ≅ 2.0 due to clusters of ions, when manganese enter the matrix agglomerated in disordered vicinities They play an important part in the spectral structure for x > 10 mol % MnO and dominate at the upper limit of the investigated concentration range For such compositions the superexchange interactions slightly narrow the absorption line

REFERENCES

1 D L Griscom, R E Griscom, J Chem Phys. 47, 2711 (1967)
2 A V de Vijn, R F Van Balderen, J Chem Phys 16, 4 (1967)
3. D Loveridge, S Parke, Phys. Chem Glasses 12, 29 (1967)
4 P C Taylor, P J Bray, J Phys Chem Solids 33, 43 (1972)
5 M Peteanu, Al Nicula, Studia Univ Babes-Bolyai, Physica 1, 63 (1981)
6 I Ardelean, Gh Ilonca, M Peteanu, Solid State Commun 52(2), 147 (1984)
7 M Peteanu, Al Nicula, Studii si Cercet de Fizica 31 (1), 15 (1982)
8 T Castner, G S Newell, W C.Holton, C P Slichter, J Chem. Phys 32, 668 (1960)
9 J W H Schreurs, J Chem Phys 69, 2151 (1978)
10 Al Nicula, M Peteanu, Rev Roum de Physique 26 (8-9), 1047 (1981)
11 D L Griscom, Glass Science and Technology 48, 151 (1990)
12 R C Nicklin, C P Poole, H A Farach, J Chem Phys 68, 2579 (1973)
13 V H Lazukin, I V Chepeleva, E A Zhilinskaya, A.P.Cernov, Phys Status Solidi (b) 69, 399 (1975)
14 IVChepeleva, E.AZhilinskaya, V.HLazukin, APCernov, VIOlkhovski, Phys Status Solidi (b) 82, 189 (1977)
15 M Peteanu, I Ardelean, Al Nicula, Rev Roum de Physique 28, 47 (1983)
16 M Peteanu, I Ardelean, S Filip, D.Alexandru, Romanian Journal of Physique (to be published)
17 V Cerny, B Petrova, M Frumar, J Non-Cryst Solids 125, 17 (1990)
18 B Petrova, M Frumar, E Cernoskova, V Cerny, J Non-Cryst Solids 161, 316 (1993)
19 V Cerny, B Frumarova-Petiova, J. Non-Cryst Solids 192 & 193, 165 (1995)
20 W H Dumbaugh and J C Lapp, J Am Ceram Soc 75, 2315 (1992)
21 K Nassau, D L.Chadwick, J Am Ceram Soc 65,486 (1982)
22 K.Nassau, D L Chadwick, J Am Ceram Soc 66, 332 (1983)
23 S Nakamura, Y Hirotsu, N.Ichinose, Japan J Appl Phys 30A, 986 (1991)
24 S Soeya, S Nakamura, N Ichinose, J Appl Phys 68, 2875 (19992)
25 Y B Dimitriev, V T Mihailova, J Mat Sci Lett 9, 125 (1990)
26 I Ardelean, S Simon, V Simon, O Cozar, J Mat Sci Lett 12, 1031 (1993)
27 I Ardelean, G Ilonca, O Cozar, V Simon, S Filip, Mat. Lett. 21, 321 (1994)
28 I Ardelean, G Ilonca, V Simon, S Filip, V Ioncu, Solid State Commun (in press)
29 I Ardelean, O Cozar, V Simon, S Filip, J Mag Mag Mat (in press)
30 I Ardelean, O Cozar, S Filip, V.Pop, I.Cenan, (to be published)

STUDIA UNIVERSITATIS "BABES-BOLYAI", PHYSICA, XL, 2, 1995

EFFECT OF Mn SUBSTITUTION FOR Cu ON THE ELECTRICAL PROPERTIES OF THE (Bi,Pb):2223 SUPERCONDUCTOR

A.V. POP[1]

ABSTRACT. The partial substitution of Mn for Cu on the electrical properties of $(Bi_{1.6}Pb_{0.4})(Sr_{1.8}Ba_{0.2})Ca_2(Cu_{1-x}Mn_x)O_y$ $(0 \le x \le 0.05)$ has been investigated by electrical resistance The zero resistivity transition temperature $T_c(\rho=0)$ decreases with increasing Mn concentration and the samples are characterized by a linear temperature dependence of the electrical resistance Below T_c, the resistance curves indicate the presence of weak links The influence of the Mn ions on the inter- and intragrain superconducting transition are discussed

Introduction. Transport and magnetic properties of Bi-Pb-Sr-Ca-Cu-O ceramics are qualitatively similar to those observed in YBaCuO, indicating the presence of some weak links These may be responsible for the current dependence of the resistivity transition curves [1]. The intergranular transport critical current density is limited by the weak link behavior of the grain boundaries [2] This deletrious influence of grain boundaries is believed to be due to the shortness of the coherence length x in these cuprate oxides. The substitution of Cu by other 3d elements should produce substantial changes in the electric and magnetic properties of the compound, useful to elucidate the mechanism of superconductivity in these materials.

In this paper the effect of the Cu substitution by Mn on the "2223" superconducting phase was investigated by electrical resistivity measurements

Experimental. The bulk samples of nominal composition $(Bi_{1.6}Pb_{0.4})(Sr_{1.8}Ba_{0.2})Ca_2(Cu_{1-x}Mn_x)O_y$ were prepared by the conventional solid state reaction. The qualitative X-Ray diffraction analysis performed with a DRON-2 equipment confirmed the predominant "2223" phase for x=0,x=0 02 Mn and 90%"2223" in the x=0 05 Mn sample The presence of about 5% "2212" phase was detected in the x=0 05 sample along with a small amount of Ca_2PbO_4.

No EPR signals related to some paramagnetic ions were observed at room temperature in our bulk samples

The electrical resistance was measured by the standard four lead technique between 77 and 290 K by using a Keithley 220 programmable current device and a Keithley 182 sensitive digital voltmeter

[1] *"Babes-Bolyai" University, Faculty of Physics, 3400 Cluj-Napoca, Romania*

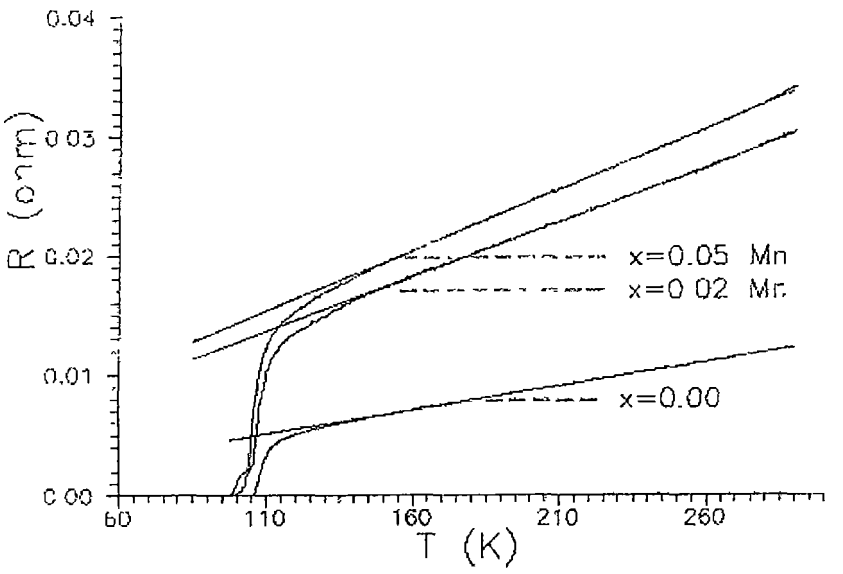

Fig. 1. The temperature dependence of the electrical resistance for the x=0.00, 0 02 and x=0 05 Mn samples

Results and discussion. The temperature dependencies of the electrical resistance R(T) for the samples x=0 00, 0 02 and x=0 05 are shown in Fig 1 , a, b and c In the 180-290 K range, these samples are characterized by a linear temperature dependence of the resistance

$$R_n=R(0)+a\bullet T \qquad (1)$$

By using the measured room temperature resistivity $\rho_0=\rho(290K)$ and the parameters R(0) and a, found by a linear regression on the data, the residual resistivity $\rho(0)$ and the temperature coefficient of the resistivity, $d\rho/dT$ were obtained (Table 1) In Table 1 one may observe an increase in $\rho(0)$ with increasing x which may be due to the Mn ions

The measured resistivity above T_c is related to the intrinsic resistivity in the **ab** plane of an

$$\rho(T)=\frac{1}{p}\left(\rho_{ab}+\rho_{ct}\right) \qquad (2)$$

ideal single crystal, ρ_{ab} by [3].

The fact that $\rho(T)$ depends only on $\rho_{ab}(T)$ is due to the c-axis orders of magnitude larger resistivity The coefficients p and r_{ct} associated with the sample polycrystalinity are extracted for each sample by assuming $\rho_{ab}(T) \cong C\times T$, where $C=d\rho_{ab}/dT=1\ 4\ m\Omega cm/K$ is the slope of resistivity for the "2212" single crystal [4] This approximate value was tentatively considered in the absence

were obtained.

Table 1. The concentration dependences of the superconducting critical transition temperatures and some parameters obtained from resistivity measurements

x	T_c [K]	$T_c(r=0)$ [K]	$\rho(0)$ [mΩ×cm]	a [mΩ×cm/K]	p	ρ_{ct} [mΩ×cm]
0 00	109.0	106.0	87	4 4	0 32	27
0 02	106 5	100 0	375	9 7	0 14	52
0 05	105.2	97 5	430	9 9	0.14	62

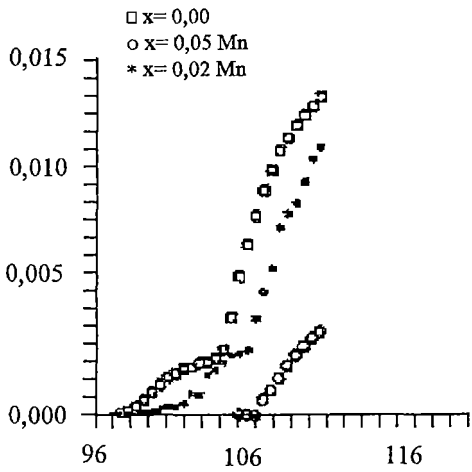

Fig 2 The tails near T_c in the R(T) dependence

The coefficient p is associated with the sample porosity (which reduces the conductive cross section) and with a path lengthening due to the random orientation of the **ab** planes of the different grains [5] The increase of ρ_{ct} with increasing x agree with the increase of contact resistance between the grains and between subgrain domains Eq (2) also shows that the intragrain critical temperature T_c concerns only the term $\rho_{ab}(T)$ associated with the grains and $T_c(\rho=0)$ concerns $\rho_{ct}(T)$. The same value $dr_{ct}/dT_c(\rho=0)\cong 4$ 1 mΩcm/K, where $\Delta r_{ct}=\rho_{ct}(x=0$ 02,0 05)-$\rho_{ct}(x=0)$ and $\Delta T_c(\rho=0)$ is the difference of zero resistivity temperature for the x=0.00 sample and x=0 02;0 05 samples respectively) suggests that the intergrain contact resistivity is similarly affected with increasing x

Fig 2 shows the shift in temperature at which the resistivity becomes zero, $T_c(\rho=0)$ as the Mn concentration increases The small tail observed in Fig. 2 is related to the weak links between the grains The dissipation below T_c and the broadening of the transition around the critical transition temperature T_c may be attributed to intergrain below T_c and intragrain weak links around T_c respectively The intragrain critical transition temperature T_c is defined as the inflection point of $\rho(T)$ i e the maximum of the first derivative

In the same substitution range, the small decrease in T_c with increasing x compared with the decrease of $T_c(\rho=0)$ suggests a concentration gradient of the Mn substituent inside the grain The energy dispersive analysis by X-rays (EDAX) measurements performed on quite similar samples by Gitsu et al [6] show that the Mn concentration at the grain boundary is substantially larger than inside the grains. The values of T_c intragrain resistive transition are very close to the T_{cG} diamagnetic transition temperature observed in the a c susceptibility measurements [7]

The ceramic high-temperature superconductors may be considered as a system of superconducting grains interconnected by three-dimensional Josephson weak-links [8]. the variation of $T_c(\rho=0)$ implies a range of weak-links characteristics for the samples investigated Thus, it can argued that the strength of the coupling between grains is larger for the undoped sample and decreases by Mn doping. The presence of Mn magnetic moments in the Josephson junctions yields a change in the phase slippage between the grains consequently reducing the Josephson current. The constant difference between $T_c(\rho=0)$ and the temperature T_p (at which the imaginary part c" from a c susceptibility presents a loss peak) denotes a completed percolation path determined by the Josephson coupling in the zero resistivity region [9]

Comparatively to the present study, in similar Cr doped samples [10] the intergrain properties are more strongly influenced in the same substitution range x while the intragrain properties are less influenced. A large broadening of the intergrain transition was observed in the Bi 2223 system doped with Sn, Sb and Ge [11,12] along with the increase of the weak-links influence. In our $(Bi_{1.6}Pb_{0.4})(Sr_{1.8}Ba_{0.2})Ca_2(Cu_{1-x}M_x)O_y$ $(0\geq x\geq 0.05)$ M=Fe,Ni the inter- and intragrain properties are similarly affected [13,14] for x£0 02. The broadening of the intragranular transition may distort the smaller but broader intergranular transition upon the nature of the 3d substituents for Cu

Conclusions. The effect of Mn doping on the normal and superconducting properties of (Bi,Pb)-(Sr,Ba)-Ca-Cu-O has been investigated

The temperature dependence of the electrical resistivity is linear above the paraconductive region The partial substitution of Mn for Cu yields a small decrease of T_c but substantially increases the residual resistivity $\rho(0)$ and the slope $d\rho/dT$ The values of the polycrystallinity coefficients p and ρ_{ct} are evaluated indicating the decrease of the percolation path length These parameters also show the different role of the inter and intragrain properties of our polycrystalline samples

The Josephson coupling between the grains decreases with increasing Mn content. This result agrees well with a c susceptibility measurements [7]

The intergranular transition shifts towards lower temperatures and the width of the intragrain transition increases with increasing dopant concentration.

REFERENCES

1 P Svoboda, P Vasek, O Smrckova, D. Sykorova, Physica **C167**, 188 (1990)
2 R L Peterson, J W Ekin, Phys Rev **B37**, 9848 (1988)
3 J Mazda, T Vidal, Phys Rev **B43**, 10560 (1991)
4 B von Hedt, W Lisseck, K. Westerholt, H Bach, Phys Rev **B49**, 9898 (1994)
5 O Cabeza, A Diaz, G Damaro, J A Veira, F Vidal, *Research Activities MIDAS Program 1990-1992*, Edited by Felix Yndurain (1993)
6 D. Gitsu, V Kantser, L.A Konopko, G Panaitov, J Superconductivity **7**, 893 (1994)
7 A V. Pop, Gh Ilonca, D. Ciurchea, V Pop, I.I Geru, Balkan Physics Letters **2**, 91 (1994)
8 M Tinkham, C J Lobb, Solid State Phys **42**, 91 (1989)
9 E Ozdas, T Firat, Phys Rev **B48**, 9754 (1993)
10 A V Pop, Gh Ilonca, D Ciurchea, V Pop, L A Konopko, I I Geru, M Todică and V Ioncu, Int J Mod. Phys **B9**, 695 (1995)
11 T W Krause, K R Nkum, W R. Datars, Physica **C210**, 333 (1993)
12 R K Nkum, W R Datars, Supercond Sci Technol **5**, 549 (1992)
13 A V Pop, Gh Ilonca, D Ciurchea, M Ye, R Deltour, I I Geru, V G Kantser, L A Konopko, Int J Mod Phys **B10**, 967 (1996)
14 A V Pop, Gh Ilonca, D Ciurchea, M Ye, I I Geru, V G Kantser, V Pop, M Todică, R Deltour, in press, J of Alloys and Compounds (1996)

STUDIA UNIVERSITATIS "BABES-BOLYAI", PHYSICA, XL, 2, 1995

BAND STRUCTURE OF $Y_2Fe_{17-x}Si_x$ COMPOUNDS

V. CRIŞAN[1]

ABSTRACT. The Y2Fe17-xSix, density of states and magnetic moments were calculated in the framework of the recursion method of Haydock The self energies and the width of the Fe 3d bands were computed from the TB-LMTO calculations for pure Y and Fe and from bulk modulus It was found that all the compounds are weak ferromagnets The Si atoms were placed in 4f crystallographic positions for x=2, and in 6g positions for x=3 The density of states for the majority and minority spin states are dominated by Fe 3d states. The Si bands are very extended and do not have significant contributions at the Fermi level The obtained magnetic moments of 2 15, 1 91 and 1 72 m_B for x=0, 2 and 3 are consistent with the experimental data

Introduction. The Y_2Fe_{17} based compounds have gained much attention as high quality magnetic materials especially when the lattice is expanded by using interstitial metalloid atoms as, C or N

In the Fe compounds the low Curie temperature is usually explained by the small Fe-Fe nearest neighbor distance of the dumbbell positions and the concomitant antiferromagnetic exchange interaction between corresponding Fe atoms. The uptake of N or C expands the lattice and in consequence enhances the Curie temperature drastically

The increase of the transition temperature can be achieved, also, by partly substitution of Fe atoms in Y_2Fe_{17}, [1], or in $Y_2Fe_{17-x}C_x$, [2], compounds with atoms as Co, Ni, Ga, Al or Si Recent experimental results show that $Y_2Fe_{17-x}Si_xN_y$ have similar properties, [3].

However, it was observed that the metalloid atoms have different effect on the lattice volume As usual in the R_2Fe_{17} compounds the yttrium atoms were used instead of rare earth, R, atoms because they have the same properties as the trivalent rare earth ions Yttrium atoms don't carry any magnetic moment and consequently we are not forced to treat the localized 4f electrons It is obvious that the Y compounds have some properties which are not the same as the rare earth ones but in our calculations they are not concludent In $Y_2Fe_{17-x}M_xC$ for x=0 and M= Al and Ga the lattice is expanded but when M=Si, Ni and Co the effect is contrary The most important change in the transition temperature was achieved by the Co substitution of Fe but this leave the lattice volume almost unchanged. So the increase of transition temperature couldn't be ascribed entirely to the magneto-volume effect.

[1] *Babes-Bolyai University, Faculty of Physics, Cluj-Napoca, Romania*

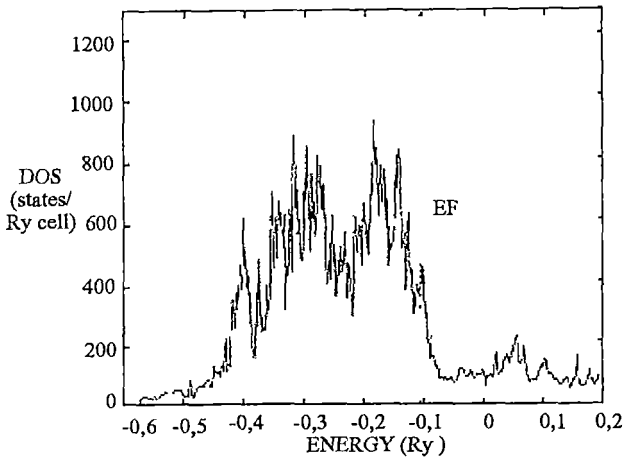

Fig 1. DOS for majority spin bands of Y_2Fe_{17}

Two explanation for the magnetic properties were used

One explain the magnetic behavior through the lattice expansion, which seems not to be the case for Si, Ni or Co atoms Moreover, the deviation from the Vegard low for M = Si compounds shows that the strength of chemical bond is varying to a large extent as function of Si content.

The other explanation ascribe the increase of transition temperature to the preferential substitution of metalloid atoms into the dumbbell sites [1] which in many cases is not confirmed by neutron, X-ray and diffraction experiments or Mossbauer data

In the present paper the density of states, (DOS), and magnetic moments were computed for experimentally determined lattice parameters The obtained magnetic moments show a good agreement with the magnetic measurements [3]

The crystalline structure The Y_2Fe_{17} compound crystallize in the Th_2Ni_{17} type of structure with $P6_3/mmc$ space group This structure was derived from CaCu5 structure type in which every third Ca atoms are substituted by a pair of Cu atoms, the so called 'dumbbell' pairs, [4] The atoms from the dumbbell positions are separated by the shortest distance in the unit cell. But the substitutions take place not always in a regular way and it is obvious that, the most common defect in these compounds is the presence of the rare earth between the dumbbell positions, and the concomitant displacement of transition metal atoms in 4e positions, but the chemical composition is preserved How the defect concentrations are affected by the transition metal substitutions is not known at present. Anyway, the effect of the defect concentration on the magnetic moments and transition temperatures is rather important even at low concentration values [5] Also present in the structure are the stacking faults in both the rhombohedral and hexagonal Y_2Fe_{17} compounds, [6,2]

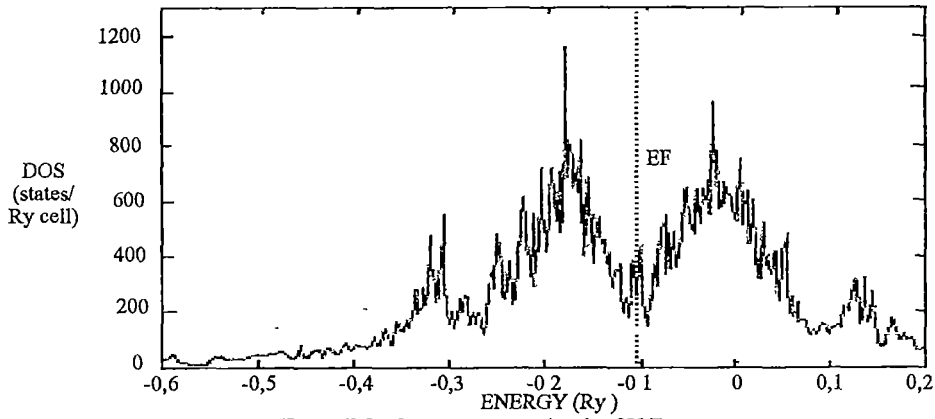

Fig. 2. DOS for minority spin bands of Y_2Fe_{17}

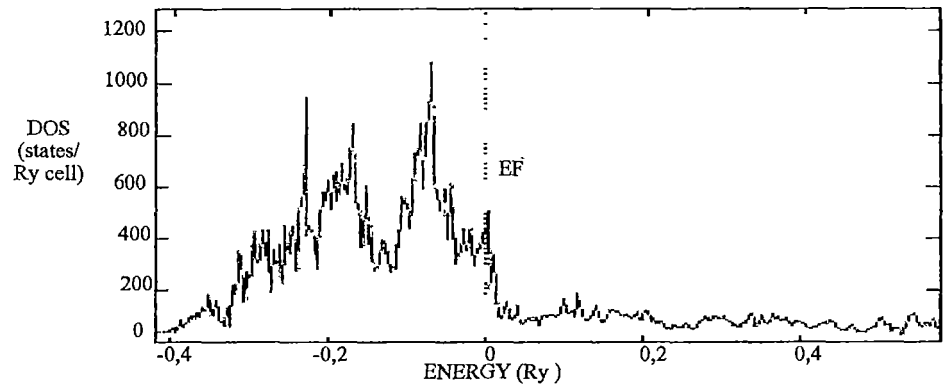

Fig. 3. DOS for majority spin bands of $Y_2Fe_{15}Si_2$

In the $Y_2Fe_{17-x}Si_x$ compounds the Si atoms substituted some of the iron atoms To explain the magnetic properties it was assumed, [1], that the Si atoms preferentially substituted the Fe atoms located in 4f positions.

But the neutron diffraction experiments [7] shows that in these compounds the assumption is no longer valid. The same results were obtained from Mossbauer experiments for Er, Nd and Tm compounds, [8,9,10] It was proved that for x<1 the substitution have the same probability for 4f and 12k positions, a little smaller for 6g and no substitution for 12j. For x>1 the rate of substitution are the same for all the atomic sites

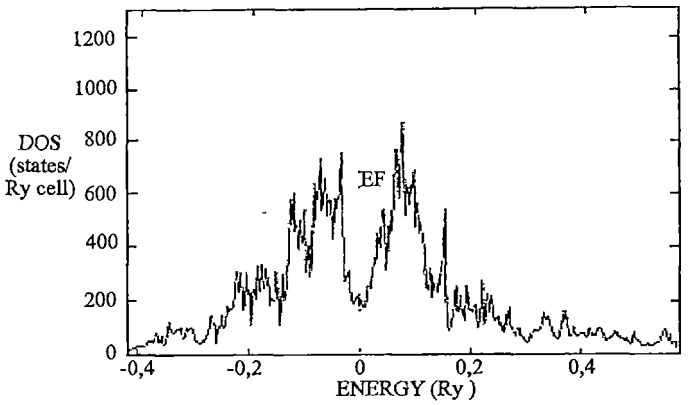

Fig. 4. DOS for minority spin bands of $Y_2Fe_{15}Si_2$

It is known, [11], that the dumbbell Fe atoms are responsible for the easy plane anisotropy X-ray diffraction analysis of aligned powders on $Er_2Fe_{15}Si_2$ indicate that the easy magnetization direction is perpendicular to the c axis for all Si

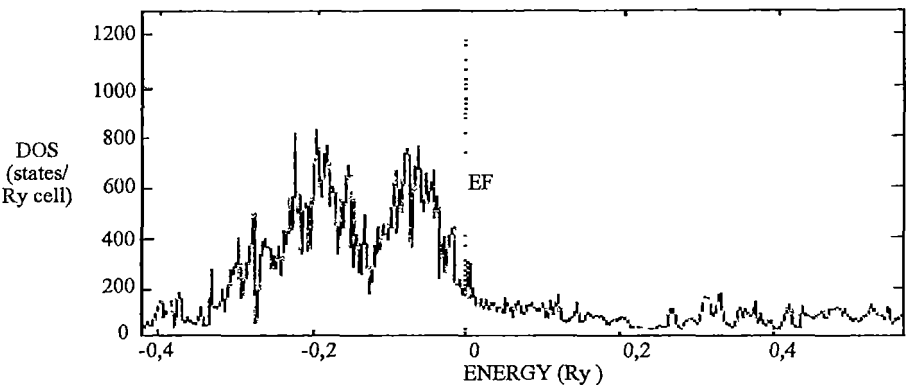

Fig 5. DOS for majority spin bands of $Y_2Fe_{14}Si_3$

concentrations

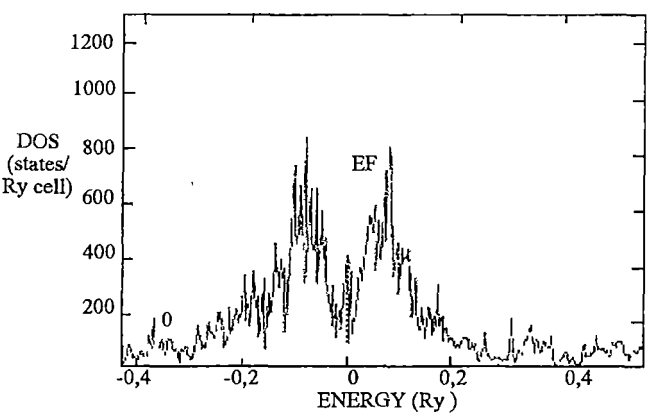

Fig 6 DOS for minority spin bands of $Y_2Fe_{14}Si_3$

Computational Method. The density of states calculations were performed using the Haydock ecursion method, [12,13], with the parameters determined with the TB-LMTO method, [15] because of the complex

atomic structure of Y2Fe17-xSix which contain 38 atoms in a unit cell and has two, (2b and 2c) non-equivalent crystallographic positions for Y atoms, and four, (4f, 6g, 12j and 12k), for Fe atoms

We used the tight-binding hamiltonian, (1), where $|i>$ and $|j>$ are d orbitals located in i

$$H = \sum_{i,j} \sum_{\mu,\upsilon} |i,\mu> t_{ij}^{\mu\upsilon} <\upsilon,j| + \sum_{i} \sum_{\upsilon} |i,\upsilon> \varepsilon_{i} <\upsilon,i| \qquad (1)$$

or j positions with μ and ν as magnetic quantum number

The transfer integrals were expressed as functions of the two center hopping integrals as function of the Wigner-Seitz radius, the distance to the nearest neighbor, and the width of the d(p) band, [14]

The Wigner - Seitz radii for the unit cell atoms, were computed from the Hartree potential calculations with the Andersen code. The values obtained from the maximum of the potential were scaled so that the total volume of the spheres are equal with the unit cell volume The resulted Wigner - Seitz radii are different from that used in other band structure calculations, (Table 1), where the radii were taken as constants for all transition metal atoms.

Table 1 The Wigner-Seitz radii for unit cell atoms, (in A)

	Y_2Fe_{17}	$Y_2Fe_{15}Si_2$	$Y_2Fe_{14}Si_3$
Y(2b)	3.373	3 361	3.378
Y(2d)	3 373	3 361	3 378
Fe[Si](4f)	2 529	2 531	2 521
Fe[Si](6g)	2 678	2.671	2 701
Fe(12j)	2 811	2 807	2 783

The basis sets of valence states used in the calculations were 4d for Y, 3d for Fe and 3p for Si atoms

The potential parameters were determined from the TB-LMTO method, [12,13]

Results and discussions

4.1. Total DOS. In Figures 1-6 the total DOS for all the compounds for non magnetic state are shown As was expected all compounds are weak ferromagnets In all compounds the total DOSs for both majority and minority -spin bands show two rather well separated peaks of bonding and antibonding character The Fermi levels are situated above the antibonding peak of majority - spin DOS and below of the minority -spin DOS antibonding peak The same form of the total DOS was reported for $Y_{23}Fe_{17}$ in [4,5], [16,17]

4.2. Local moments and local DOS In Table 2 the calculated local moments are compared with data of Mossbauer and neutron diffraction experiments as well as with other band calculations

Table 2. The computed magnetic moments for $Y_2Fe_{17-x}Si_x$, x=0,2,3

	Y(2b)	Y(2d)	Fe[Si](4f)	Fe[Si](6g)	Fe(12j)	Fe(12k)	μ/Fe	Ref
Y_2Fe_{17}	-0 28	-0.27	2 15	1 99	2.29	1.92	2 06	this work
			2 38	1 66	2 06	1 93	1.98	[5]
			2 31	1 55	1 86	1 73		[21]
	-0 47	-0 47	2 53	1 92	2 25	2 00		[16,17]
	-0 43	-0 43	2.45	2 15	2.09	2.10		[22]
							2 06	[7]
$Y_2Fe_{15}Si_2$	-0 24	-0 21	-0 07	1 72	2.29	1 95	1 99	this work
							1.83	[7]
$Y_2Fe_{14}Si_3$	-0.19	-0 20	1.91	-0 13	2.07	1 77	1.86	this work
							1 86	[7]

For Y_2Fe_{17} the Fermi level is situated in front of the antibonding DOS for up spin bands, on a local maximum formed by states of Fe(12j,12k,and 6g) atoms and not at all by Fe(4f) atoms For the minority spin bands the Fermi level is situated in a minimum of the DOS where the main contributions came from Fe(12j,12k, 6g,4f)

For $Y_2Fe_{15}Si_2$, the Fermi level is situated again in the front of the majority -spin bands DOS and in the minimum between the bonding and antibonding bands DOS As in the Y_2Fe_{17} compound the maximum is formed from Fe(12j,12k,6g) contributions The local minimum of the down spin bands DOS where the Fermi level is situated, cames from Fe(12j,12k,6g) states The Si atom states are very extended and have no significant values at the Fermi level. So the Si substitution (in 4f positions) cancel the Fe contributions to the DOS of the minority spin bands In the same time, with the increase of Si content, the DOS at the Fermi level for majority -spin bands are diminished It could explain the increase of transition temperature as regard the Y_2Fe_{17} compound

For the $Y_2Fe_{14}Si_3$ the total DOS have the same structure bonding and antibonding for both spin bands For minority -spin bands the Fermi level is situated in a valley between bonding and antibonding states but where the 4f contribution is not canceled. The Fermi level for the up tates is situated very close to an maximum Again major contribution cames from the minority -spin bands

It seems that the lattice parameters are not the crucial for the transition temperature variation It depends also on what sites the substitutions take place Together these two effects

could be important. In the spirit of Moohn and Wohlfarth spin fluctuation theory the crucial fact is the decrease of the DOS at the Fermi level So, the small increases of transition temperature for $Y_2Fe_{15}Al_2$ as compared with the increases of transition temperature in $Y_2Fe_{15}Si_2$ could be explained using the $Y_2Fe_{15}Si_2$ bands by moving the Fermi level towards the lower energy It is seen that the decreases of the DOS at the Fermi level is not so important as in the case of Si alloy, and consequently the decreases of transition temperature is not so important.

Acknowledgment. The author are indebted to helpful discussions with O.K.Andersen and O.Jepsen Our computer code is based on a TB-LMTO-ASA program developed in the group of O K.Andersen at the Max-Planck-Institut fur Festkorperforschung in Stuttgart.

REFERENCES

1 K Strnat, *Ferromagnetic Materials*, Vol 4, pg 132, eds E P.Wohlfarth and K H J Buschow (North Holland, Amsterdam, 1988)
2 K H J Buschow, T H Jacobs, W Coene, IEEE Trans Magn 26, 1364, (1990)
3 M Valeanu, N Plugaru, E Burzo, Sol State Comm 89, 519, (1994)
4 R Coehoorn, Phys Rev B39, 13072 (1989)
5 V Crisan, V Popescu, A Veines, D. Andreica, I Burda, S Cristea, J Alloys Comp, 217, 258-262, (1995)
6 C W Allen, D L Kuruzar, A E Miller, IEEE Trans Magn MAG-10, 716 (1974)
7 Chin Lin, Y -X Sun, Z -X Liu, H -W Jiang G Jiang, Solid State Communications 81, 299 (1992)
8 E E Alp, A M Umarji, S K Malik, G K Shenoy, M Q Huang, E B Bitich, W E Wallace, J Magn Magn Mat 68, 305 (1987)
9 R van Mens, J Magn Magn Mat. 61, 24 (1986)
10 P C M Gubbens, A M van der Kraan, T H Jacobs, K H J Buschow J Less, Common Metals, 159, 173 (1990)
11 M T Averbuch-Pouchot, R Chevalier, J Deportes, B Kebe, R Lemaire, J Magn. Magn Mat. 68, 190 (1987)
12 R Haydock, V Heine, M J Kelly, J Phys C 8,2591,(1975)
13 V Heine, Solid State Physics 35,1,(1980)
14 D G Pettifor, J Phys F 7,613,(1977)
15 O K Andersen, Phys Rev B12,3060,(1975)
16 S S Jaswal, IEEE Trans. Magn 28, 2322 (1992)
17 S S Jaswal, W B Yelon, G C Hadjipanayis, Y Z Wang, D J Sellmyer, Phys Rev Lett 67, 644 (1991)
18 P Mohn, K Schwarz, Physica B-C 130B, 26 (1985)
19 A Oppelt, K H J Buschow, J Phys F3, L212 (1973)
20 T Dumelow, P C Riedi, P Mohn, K Schwarz, Y Yamada, J Magn,Magn Mater, 54-57, 1081 (1986)
21 J Inoue, M Shimizu, J Phys F15, 1511 (1985)
22 B Szpunar, J A Szpunar, J Appl Phys 57, 4130 (1985)

STUDIA UNIV BABES-BOLYAI, PHYSICA, XL, 2, 1995

BAND STRUCTURE OF UCr_4C_4 AND UW_4C_4 COMPOUNDS

V. CRIŞAN[1]

ABSTRACT Using the TB-LMTO method the band structure parameters were determined for ternary carbides UCr_4C_4 and UW_4C_4 The parameters were used in a recursion method calculations taking into account all electronic states The compounds were found to have metallic character when the f states of uranium were considered to form band states The contributions of different orbitals at the Fermi level were determined The tungsten atoms lost 0 8 electrons, the chromium atoms 0 93 electrons per atom, and uranium atoms gain about 0 6-0 75 electrons per atom The density of states at the Fermi level in UW4C4 and UCr4C4 are 106 and 141 states/formula unit/Ry. Based on these results a three band model for the electronic states at the Fermi level was proposed.

Introduction. The actinoid - transition metal - carbon systems have been investigated especially because of their importance in nuclear reactor technology, [1]. The uranium -chromium-carbon system contains few compounds as $UCrC_2$, $U_3Cr_2C_4$ [2,3], UCr_2C4 [4], and UCr_4C_4, reported by Behrens and Jeitschko,[5]

The uranium-tungsten-carbon system contains UWC_2, [2], with isolated carbon atoms or C2 pairs, [3,6], UWC_{2-x}, [7,8,9] and UW_4C_4, [10,11] The ternary compounds UCr_4C_4 and UW_4C_4 have very high magnetic susceptibilities, which also are slight temperature dependent This behaviors were ascribed to the spin fluctuations of the mixed valent systems, [10,12]

The Crystalline Structure The crystal structure of UCr_4C_4 can be derived from that of $MoNi_4$ The positions of uranium and carbon atoms correspond to the positions of the Mo and Ni atoms in $MoNi_4$ The carbon atoms occupy distorted octahedral voids formed by four chromium and two adjacent uranium atoms The uranium atoms have 8 carbon atoms at 252 0 pm, the chromium atoms have 4 carbon atoms at 195-198 7 pm and the carbon atoms have 4 chromium atoms at195.8-198.7 pm as nearest neighbors The UW_4C_4 with tetragonal symmetry, a=832 71pm and c=313 58pm, [10], have the same atomic arrangement like UCr_4C_4 The differences consists in small distortions which lower the symmetry from I4/m to P4/m While in UCr_4C_4 all the chemical identical atoms are also identical from crystallographic point of view, in UW_4C_4 there are two different atomic positions for each chemical sort of atom in the structure There are two kinds of uranium atoms one with 8 carbon atoms as nearest neighbor at 263pm, and another with the same number of carbon atoms as nearest neighbors but at 248 pm, two kinds of tungsten

[1] *"Babes-Bolyai" University, Faculty of Physics, 3400 Cluj-Napoca, Romania*

atoms one with 4 carbon atoms as nearest neighbors at 207-219 pm and the other with 4 carbon atoms as nearest neighbor at 207-211pm, and two kinds of carbon atoms one with 4 tungsten atoms as nearest neighbors at 211-219 pm and the other also with 4 tungsten atoms as nearest neighbors at 207pm

So, going from UCr_4C_4 to UW_4C_4 the bonding of each atom will be changed in such a way that· the U-C bond will be, in UCr_4C_4, between the two U-C bonds of UW_4C_4, the tungsten atoms have different nearest neighbors, and the W-W bonding is the most affected by the splitting of the two kind of tungsten atoms

Density of States Calculations.Results Using the Hartree part of the TB-LMTO Andersen code the band parameters were computed The input valence states for the two compounds are $7s^27p^66d^15f^3$ for uranium atoms, $6s^26p^05d^45f^0$ for tungsten atoms, $2s^22p^23d^04f^0$ for carbon atoms and $4s^14p^03d^54f^0$ for chromium atoms In the crystalline structure, 2 empty spheres in UCr_4C_4 and 3 empty spheres in UW_4C_4 were accommodated

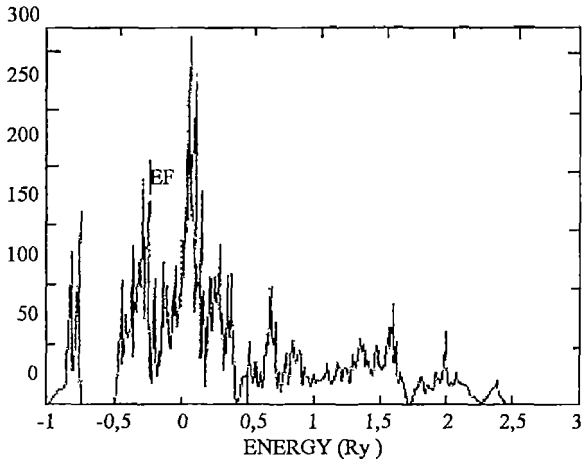

Fig 1 Total density of states, (DOS) for Ucr, C

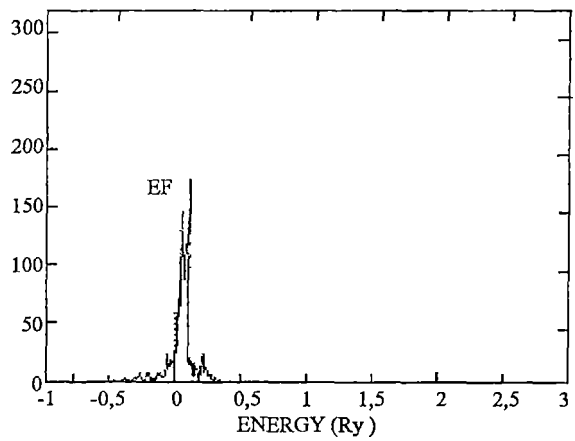

Fig 2 DOS for uranium (1-3) for Ucr,C

Taking into account the d and s states for uranium, the d, p and s for tungsten and cromium, and p and s states for carbon atoms and the determined band parameters we used the recursion method of Haydock, [13, 14] to compute the local and total

density of states It was obtained that the main contribution at the Fermi level is done by the uranium states which are situated in an interval of 0.1 Ry around the Fermi level

Unlike in the UCr_4C_4, in the UW_4C_4 compound, the unit cell contains two sorts of uranium, tungsten as well as carbon atoms From the TB-LMTO calculations it resulted that the center of the (7s) bands of one uranium atom is at the Fermi level, and of the other one is shifted with 0 08 Ry towards higher energy. The same peculiarities are seen for all 6d, 7p and 5f uranium bands.

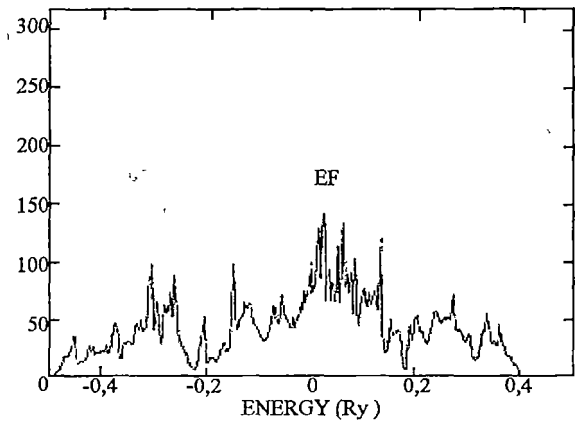

Fig 3 DOS for cromium (l=0,1,2) from UCr_4C_4

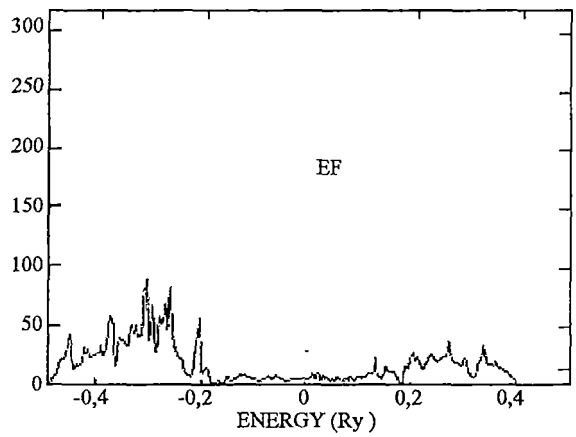

Fig 4. DOS for carbon (l=0,1) from UCr_4C_4

The s and p bands of the two sorts of tungsten atoms are no longer shifted. The same trend was observed for the C(2s) and C(2p) bands. On the other hand, the shift between the two sorts of tungsten 4d bands, 0 2 Ry, have no importance because these bands are located far away from the Fermi level It resulted that the electron occupation numbers are practically the same for the uranium and carbon atoms in the two structures, due in special to the same number of valence electrons for W and Cr atoms. It is seen that in both compounds the s states lost their electrons to a large for all the atoms Also, in both compounds the W and Cr atoms lost 0 8 electrons for each tungsten atom and 0.93 electrons for each chromium atom and the uranium atoms gain about 0 6-0 74 electrons for each atom The

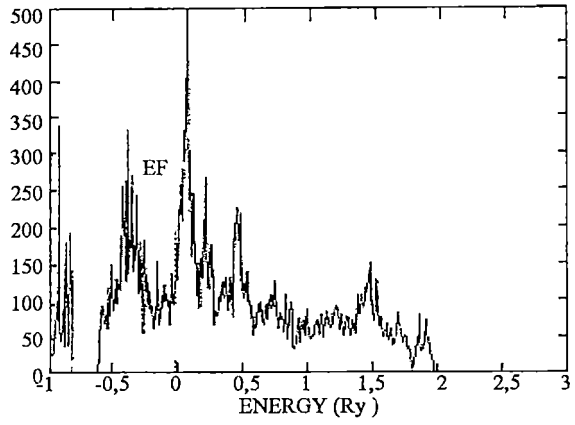

Fig 5 Total DOS for UW_4C_4

carbon atoms don't change the total valence charge per atom in the compound, but in the formation of the solid the contribution of the l=0 is diminishing and of the l=1 is growing

The total and local density of states, (DOS), are shown in Figures (1-4) for UCr_4C_4 and in Figures (5-11) for UW_4C_4 The total DOS at the Fermi level in UW_4C_4 and UCr_4C_4 are 106.81 and 141 73 states/formula unit/Ry The total DOS have a maximum just above the Fermi level for both compounds The band width of the 5f states is 0.8 Ry and of the 6d states is 0 9 Ry The most important contribution to the density of states comes from the chromium 3d states, which is four times larger than that of uranium atom The contributions of the 4s and 4p states at the Fermi level are small as well as the carbon atoms As compared with the uranium and chromium atoms the carbon contribution to the density of states at the Fermi level, is the smallest. The ratio of the total DOS at the Fermi level of the two substances is

$$\frac{N(UW4C4)}{N(UCr4C4)} = 1\ 36$$

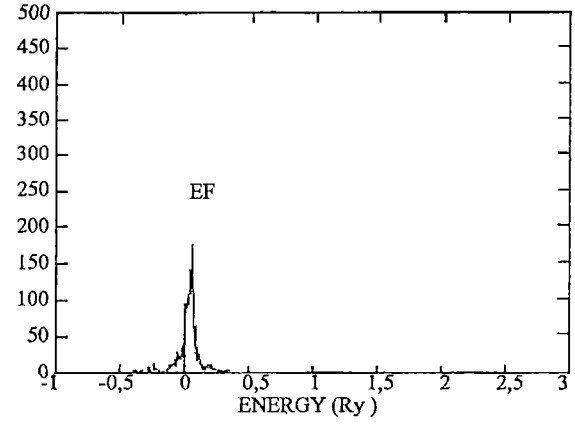

Fig 6 DOS for U1 (l=3) atom from UW_4C_4

The Three Orbital Model. Using the previous results, the DOS at the Fermi level were recalculated in the tight binding approximation by the recursion method [13, 14] in a model with one orbital per atom Due to the computational problems, as in previous calculations, the f states are replaced by d

states The model we used have one d orbital for uranium, d(xy), and for chromium atoms, d(yz), and one p orbital for carbon atoms, p(x).

The self-energies were taken from Herman-Skillmann calculations for free atoms [15] as follows·

$$\varepsilon(U) = -6.1064eV, \varepsilon(Cr) = -6\ 513eV, \varepsilon(C) = -8\ 98eV, \varepsilon(W) = -9.30376eV.$$

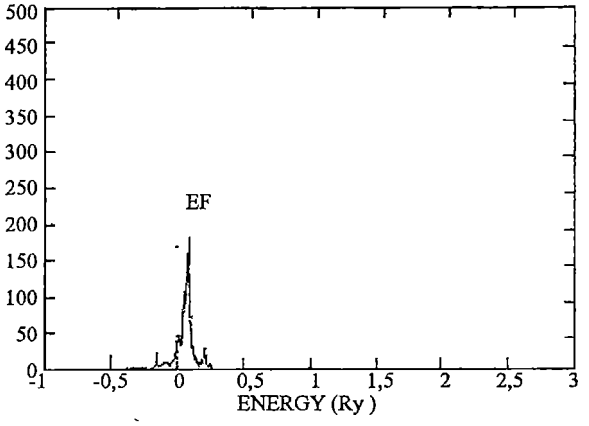

Fig 7 DOS for U2 (1-3) atom from UW_4C_4

The transfer integrals were computed in the two center approximation of Slater and Koster, using the Harrison's universal formulas [16]. The Fermi level is located in front of the peak of the Cr (W) states The uranium states are in front of the Fermi level, as resulted in previous calculations The DOSs for the UW_4C_4 compound have the same shape as those of UCr_4C_4 but the C contribution is closer to the Fermi level in the first compound The ratio of the total DOS at the Fermi level is

$$\frac{N(UW4C4)}{N(UCr4C4)} = 1.59$$

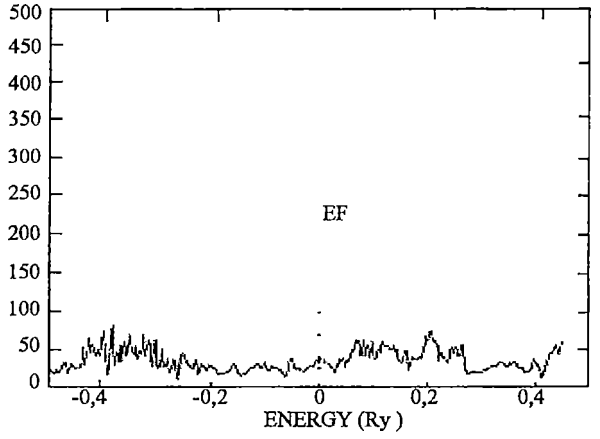

Fig 8 DOS for W1 (l=0,1,2) atom from UW_4C_4

The obtained ratio is almost the same as that resulted from full states calculations Because in our model the shape of density of states are the same as that resulted from full states calculations, it seems that a tight binding picture with one orbital/atom is rather good.

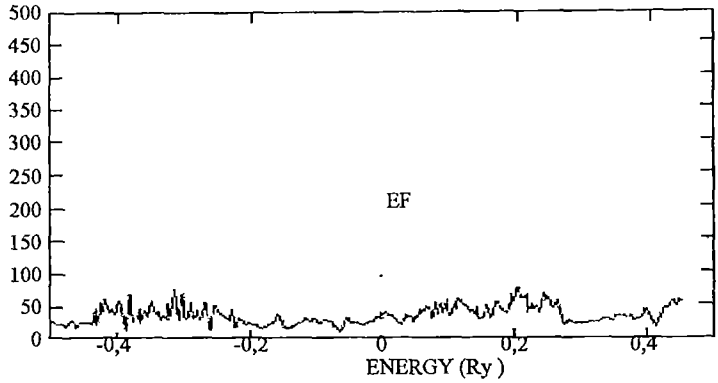

Fig 9. DOS for W2 (l=0,1,2) atom from UW_4C_4

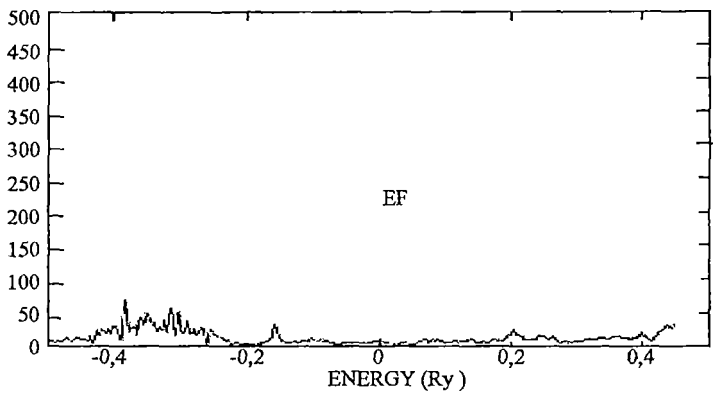

Fig. 10 DOS for C1 (l=0,1) atom from UW_4C_4

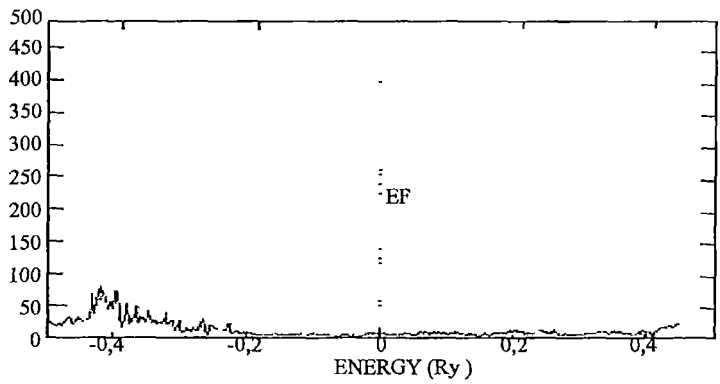

Fig 11 DOS for C2 (l=0,1) atom from UW_4C_4

Acknowledgments. The author thanks to Prof O K.Andersen for his hospitality during the visit at the Max-Planck-Institut für Festkörperforschung Stuttgart where important parts of the reported research have been accomplished The computer code for the TB-LMTO calculations was developed by the group of O K.Andersen in Stuttgart.

REFERENCES

1 H Hollec, *Binare und ternare Carbid und Nitridsysteme der Ubergangsmetalle,* Gebr Borntraeger, Stuttgart, (1984)
2 D T Cromer, A C Larson, R B Roof jr , Acta Crystallogr 17, 272 (1964)
3 W Jeitschko, R K Behren, Z Metallkde 77, 788 (1986)
4 Z M Alekseeva, O S Ivanov, in Thermodynamics of nuclear materials, vol 2, IAEA, Vienna, 247 (1980)
5 R K Behrens, W Jeitschko, Monatsh Chem 118, 43 (1987)
6 H J Clark, R Mountford, I J McColm, J Inorg Nucl Chem 34, 2729 (1971)
7 M. Ugajin, I Takahashi, J Nucl Matter 37, 303 (1970)
8 C Politis, J Nucl Matter 39, 258 (1971)
9 M Ugajin, Y Suzuki, J Shimokawa, J Nucl Mater 43, 277 (1972)
10 R K Behrens, W Jeitschko, J Less Common Met 160, 185 (1990).
11 R K Behrens, W Jeitschko, Z.Kristllogr 182, 19 (1988)
12 T Vomhof, R Pottgen, W Jeitschko, J Alloys and Compounds 196, 173 (1993)
12' R Haydock,V Heine, M J Kelly, J Phys C 8,2591 (1975)
12" V Heine, Solid State Physics 35,1 (1980)
14 F Herman, S Skillman, *Atomic Structure Calculations* , ed. Prentice -Hall Inc , London ,1963
15 W A Harrison, *Electronic Structure and Properties of Solids* ed Mir,Moscow ,1983

STUDIA UNIVERSITATIS "BABES-BOLYAI", PHYSICA, XL, 2, 1995

N.A.A OF Au, Ag, AND Cu WITH ISOTOPIC NEUTRON SOURCES AND NaI(Tl)

L.DARABAN, T.TÂRSU, T.FIAT, C.COSMA, D.BOROS[1], M.BAYER[2]

ABSTRACT. The paper advances the removing of interference problems in establishing the Au, Ag and Cu contents from archaeological silver objects, when using isotopic sources and NaI(Tl) scintillator detector. The conditions which lead to correct analysis are discussed and results are given for some antique and medieval silver coins and jewelry

Introduction. In the last decades a new science has developed archaeometry, by which the investigative techniques of archaeology have radically changed The applying of N.A A methods, offered an investigation technique which permits the coins analysis and the finding out of forgeries, jewels and weapons analysis, but first ranking the source identification of some materials used for manufacturing archaeological objects· obsidian ceramics, marble statues, coins, weapons, jewels, paintings.

The identification of sources based on impurity marks of material and source is an incontestable evidence of economical relations between different human communities

Thus, it is possible·

a) The evidence of gold sources from different geographical regions by Au/Ag diagram in relation to Bi/Ag ratio, or at silver coins the changing of raw material source or of silver title, according to the lead or iron traces [1-4]

b) The identification of obsidian sources, which in the prehistory of the world could be found on large areas (in Romania there are no obsidian sources), obtaining this way information about the areas in which this material was found in the Neolithic [5-8] as well as about the relations between the communities

c) The discovery of the sources of clay pots [9-12] and of the marble statues [13] markes it possible to establish if these had been imported or locally manufactured, after models brought from antique metropolis

d) The study of the alloys compositions and accordingly of the structural modification, which permit to furnish information about the manufacturing technology Thus, by the ore processing for the mining of silver, Mn and As evaporate with the slag, while Sb, Pb, Cu, Sn remain. Lead is the best indicator for the efficiency of the technological process,

[1] *National History of Transilvania Museum*
[2] *CMSSC - Cluj-Napoca*

and the Cu and Ni have a strong correlation with the source because of their entity in the ore-father [14]

The method of N.A.A. N A A. is most attractive for archaeological subjects because of its great sensitiveness, simplicity, rapidity and especially because it is nondestructive N A A is based on nuclear reactions which form in the sample isotopes with radioactivity directly proportional with the mass (therefore with the concentration) of the irradiated element, according to formula [15]·

$$A = N\varnothing\frac{\sigma\theta m}{M}\left[1-\exp\left(-\lambda t_{ir}\right)\right]\exp\left(-\lambda t_{dez}\right) \qquad (1)$$

where A[Bq] is the activity of the studied radioisotope, measured after disintegrating time t_{dez},

$N = 6.023\ 10^{23}$ atoms/mol (Avogadro's number),

$\varnothing$ [n/(cm^2 s)] - neutron flux which crosses the sample,

σ [cm^2] - activation cross-section

θ [%] - isotopic abundance of the activated isotope,

m [g] - the mass of pure target-element,

$\lambda\left(=\frac{\ln 2}{T_{1/2}}\right)$ - radioactive constant of the formed radioisotope, $T_{1/2}$ is the half-life of this isotope, (t_{ir} and t_{dez} are expressed in same units as $T_{1/2}$), t_{ir} - the irradiating time

If there are many radioisotopes created in the sample, the total activity is the sum of all the activities of the created radioactive isotopes:

$$A_{tot} = \sum Ai \qquad (2)$$

That's why in N A.A there are used gamma spectrometers with the purpose of apart determination of A_i activity of each created radioisotope

The difficulties in obtaining precise measurements, the differences found in scientific works between the values of activation cross-section and half-lifes, the errors in absolute measuring of activity are the main factors which affect this method. That's why [15], the most used method is the relative one, based on the relation·

$$\frac{A_{sample}}{A_{standard}} = \frac{C_{sample}}{C_{standard}} \qquad (3)$$

where A are the activities of the studied radioisotope in the sample and in the standard and C are the concentrations of this isotope

In this calculation, it must also be considered too idez, the weight of the sample and the separation efficiency (if chemical separation were made).

Nuclear reaction for the activation of Au, Ag, Cu For the determination of gold, the main nuclear reaction for the analysis is

$$^{197}Au + n\varnothing \longrightarrow {}^{198}Au + \text{prompt radiation, i e } {}^{197}Au\ (n, \gamma)\ {}^{198}Au$$

A new radioisotope (^{198}Au, with $T_{1/2}$ = 2.7 days) is formed which emits a gamma quantum with E_γ = 410 KeV (Fig 1) This nuclear reaction is produced if the sample is irradiated with thermal neutrons

But, if the irradiation is made with fast neutrons another nuclear reaction occurs ^{197}Au(n, 2n)^{196m}Au The formed radioactive isotope ($T_{1/2}$ = 10 hrs) emits several energies of gamma radiation According to [15], E_{γ_1} = 149 KeV, E_{γ_2} = 176 KeV and E_{γ_3} = 188 KeV, in keeping with [16] interest presents only the quantums E_{γ_1} = 147.8 KeV (42,5%) and E'_{γ_3} = 188 3 KeV (37.4%) for the isomer ^{196m_2}Au About E_{γ_2} the disintegration diagram of this isomere has not yet been elucidated

The nuclear reactions (n, 2n) of ^{197}Au are less studied in the scientific literature In [17] there have been studied the reactions ^{197}Au(n, 2n) ^{196}Au and ^{197}Au(n, g)^{198}Au and it has been calculated the cross-section of ^{197}Au for a neutron energy of 14 MeV In the graphic $\sigma_{n,2n} / \sigma_{n,n}$ for the nuclear reaction ^{197}Au(n, 2n)^{196}Au as a function of exciting energy of the nucleus from [18], the maximum of the curve is at 14 3 MeV.

The nuclear reactions with fast neutrons of Au, Ag, Cu have been studied in [19] and used in the determination of the content of these elements in antique coins

The study of gold activation has been approached in other papers too The radioactivity of the sample confirmed the development of the nuclear reaction ^{197}Au(n, 2n)^{196}Au It was produced the resonance reaction ^{197}Au(n, γ)^{198}Au too, with $T_{1/2}$= 2 7 days But at irradiation of gold with fast neutrons of 14 MeV, [15] points out the reaction ^{197}Au(n, p)^{197m}Pt on the gamma peak of 0 34 MeV, with $T_{1/2}$ = 80 min.

In [20] it is proved that the isotope ^{196}Au has $T_{1/2}$ = 5 5 days and that at the gold irradiation with fast neutrons an isotope with $T_{1/2}$ = 10 ± 0.5 hrs occurs

The β radiations spectrum of ^{198}Au is given in paper [21], the maximum energy being of 962 KeV

At the silver irradiation with thermal neutrons, the nuclear reactions $^{107}Ag(n, \gamma)^{108}Ag$ and $^{109}Ag(n, \gamma)^{110}Ag$ take place simultaneously (Fig 2)

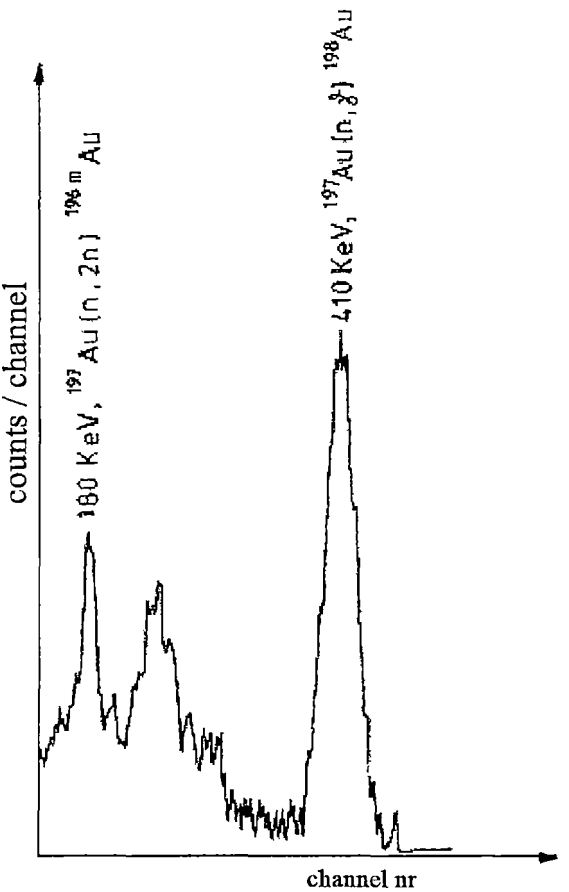

Fig 1. Gamma radiation spectrum emitted by a purely gold sample, irradiated in a mixed (fast and thermal) neutrons flux and measured by a NaI(Tl) scintillation counter of 2 x 2 inch

As a result it is formed [15] the radioisotope ^{108}Ag with $T_{1/2}$ = 2 5 min, which emits gamma quantums with the energy 632 98 KeV (100 %), 618 85 KeV (14 3 %) (therefore as a whole 0 63 MeV) and gamma quantums of 433 932 KeV (27 4 %) [16]

The disintegration diagram of ^{108}Ag given by [22] shows that it is emitted too a β^+ radiation (15 %) with the maximum energy of 780 KeV, therefore in the gamma spectrum of a silver sample it must occur too the peak of 511 KeV due to the positronic annihilation.

The nuclear reaction $^{109}Ag(n,\gamma)^{110}Ag$ which forms the radioactive isotope ^{110}Ag with $T_{1/2}$ = 24 2 sec [23] and which emits a main gamma quantum of 657 71 KeV (100 %) [16], that means the peak from 0 66 MeV (Fig. 2). The disintegration diagram is given in [22] With these nuclear reactions we shall make the silver analysis from archaeological objects, but it is worth pointing out that, according to [15] and [19], the isotope ^{108}Ag can be formed also through fast neutrons irradiation $^{109}Ag(n, 2n)^{108}Ag$, and that to the 0 511 MeV peak can contribute copper too, but also the nuclear reaction $^{107}Ag(n, 2n)^{106}Ag$, which gives ^{106}Ag with $T_{1/2}$ = 24 min (it is possible to have it on the spectrums

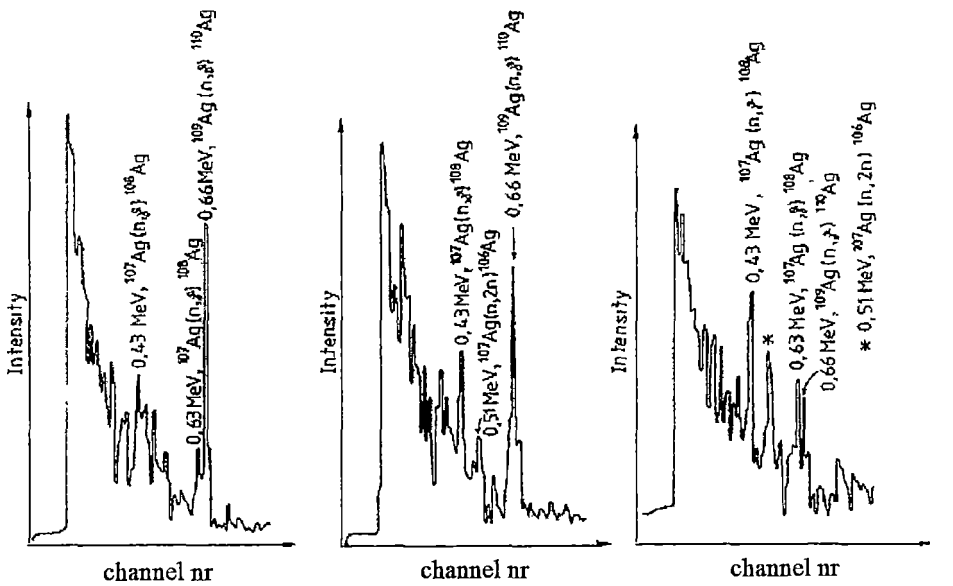

Fig. 2 Gamma radiation spectrum of a silver sample at different time moments, recorded by us with a Ge(Li) semiconductor detector, accumulated each time till 10^2 impulses (30 minutes irradiating time), a) 19 sec, 19 sec + 1min, c) 19 sec + 5 min disintegration time

from fig 2) Through irradiation with fast neutrons of 14 MeV, the following nuclear reactions are pointed out [15]

^{107}Ag(n,p)^{107m}Pd on the peak of 0.21 MeV resulting the radioisotope ^{107m}Pd with $T_{1/2}$ = 21 sec, at the energy of 0 093 MeV it contributes the reaction ^{107}Ag(n,n')^{107m}Ag having $T_{1/2}$ = 44 3 sec, and at the 0 088 MeV peak contributes with the greatest efficiency the reaction ^{109}Ag(n, n')^{109m}Ag with the half-life of the formed isomere $T_{1/2}$ = 39.2 sec

Because at silver irradiation with neutrons radioisotopes with very short half-lifes (under 1 minute) are also formed , it is necessary that the irradiated sample to be immediately measured, because otherwise in less than 7 seconds an important part of the radioactivity disappears

Copper can generate β^+ - active radioisotopes, received on the gamma peak of 0 511 MeV (fig 3) Thus, according to [15], at this energy from the spectrum of the irradiated copper with thermal neutrons, it contributes ^{64}Cu with $T_{1/2}$ = 12 8 hrs, formed through nuclear reactions ^{63}Cu(n, γ)^{64}Cu with thermal neutrons and ^{65}Cu(n, 2n)^{64}Cu with fast neutrons It contributes another β^+ - active isotope too, with $T_{1/2}$ = 9 8 min, namely ^{62}Cu, formed through fast-neutrons irradiation ^{63}Cu(n, 2n)^{62}Cu

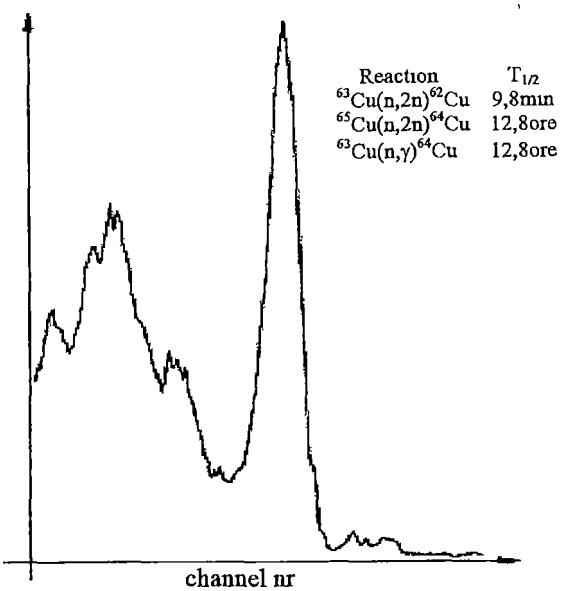

Fig. 3. Gamma radiation spectrum of irradiated copper with fast and thermal neutrons

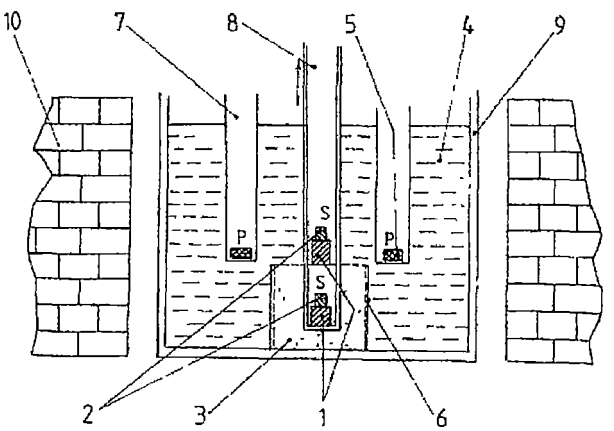

Fig. 4. Neutrons irradiation device
Disposing of neutron sources, motion mode and possibilities of samples irradiation
1 ^{241}Am-^{9}Be neutron source, 2 ^{239}Pu-^{9}Be neutron source, 3 Boric paraffine, 4 Moderator block of pure paraffine, 5 Sample for irradiation, 6 Cd-Pb covering, 7 Irradiation channels; 8 Gliding tube; 9 Iron vase, 10 Protection brick of boron paraffine

It is pointed out at the 1 17 MeV peak the nuclear reaction $^{65}Cu(n, \alpha)^{62}Co$ with $T_{1/2}$ = 13 9 min, for ^{62}Co [15] and at the 1 04 MeV peak the reaction $^{65}Cu(n, \gamma)^{66}Cu$ obtained through thermal neutrons irradiation, with $T_{1/2}$ = 5.15 min for ^{66}Cu [15], both with small efficiency

Presentation of irradiation arrangement For obtaining such nuclear reactions, the control of reaction channels can be achieved by neutron energy using a neutron irradiation arrangement like the one described in fig.4

The irradiation arrangement includes two isotopic sources of neutron one of type ^{241}Am-^{9}Be with 5 Ci activity, which debits in a 4π solid angle 1 1 x 10^7 n/s flux, and a source of type ^{239}Pu-^{9}Be of 15 Ci, with an emission of 5 5 x 10^7 n/s They emit [24]two main groups of fast-neutrons with the energy of 3 2 and 5 1 MeV, but also a fractional part of slow neutrons

In both types of sources the neutrons are obtained through bombarding beryllium with α - particles of 5 48 MeV (the case of ^{241}Am-^{9}Be source) and 5 15 MeV (the ^{239}Pu-^{9}Be

source) resulting from the nuclear reaction $^{9}Be(\alpha, n)^{12}C$ following the intermediate $^{13}C^{*}$ nucleus transition The remaing ^{12}C nucleus can remain in the exciting state of 4.43 MeV in 60% of all cases, emitting this desexcitation gamma quantum simultaneously with the corresponding neutrons

The sources are plased in a polyethylene tube, closed at an extremity, which can move them vertically from the store position up to the irradiation position, when in the lateral channels can be generated a thermal neutron flux too, after the passage through paraffin of the neutrons emitted by the source, next to the neutrons that remained fast (fig. 4)

The irradiation times differ, as a function of the analysed element, but for obtaining a maximum activity one can carry out a saturation irradiation when $t_{ir} = 3.5\ T_{1/2}$

It is obvious that other chemical elements of the sample can catch neutrons too and transform themselves in radioactive isotopes and so the radioactivity in the sample is according to relation (2) a sum of emission of many radioisotopes. That's why the radioactivity measurement of the irradiated samples can't be made through a total measurement but through gamma spectrometry, i e. measuring the intensity of gamma radiation emitted by the sample as a function of energy

Measurement conditions With the purpose of analyzing the samples irradiated with neutrons, we used a gamma radiation spectrometer, which consists in a scintillation probe with NaI(Tl) crystal of 2x2 inch coupled to an impulses selector (the monochannel selector type 20160 RFT made in GDR). The scintillation detector is protected in a lead fower for reducing the radiation background The device provides the number of impulses as a function of their amplitude (expressed in volts) either step by step (numerical system) or continuously, through integration and graphic These impulse spectrums are calibrated with gamma sources of known energies, like ^{137}Cs, ^{60}Co, ^{241}Am

Although it has a better detection sensitivity, the energetically resolution of this device is smaller than of the one using a Ge(Li) semiconductor detector, the peaks of the spectrum being much larger and that's why the interference probability with other radioisotopes is greater and a succession of analysis errors can occur.

Thus, at the 410 KeV peak of ^{198}Au can also contribute ^{116m}In with $T_{1/2} = 54$ min, occured in the nuclear reaction $^{115}In(n, \gamma)^{116m}In$, if the sample contains In traces, this element being, very easy to activate with neutrons (fig. 5) and at the neighbouring energy of 430 KeV (difficult to solve by the scintillation detector) can contribute too a peak of ^{108}Ag (see fig 2) and of ^{198}Au.

But, there have the half-life much shorter than of the radioisotope ^{198}Au and then, these interferences can be eliminated by waiting the disappearance of these radioactive isotopes by disintegration and carrying out measurements later (after some hours) only on ^{198}Au, which has $T_{1/2} = 2\ 7$ days

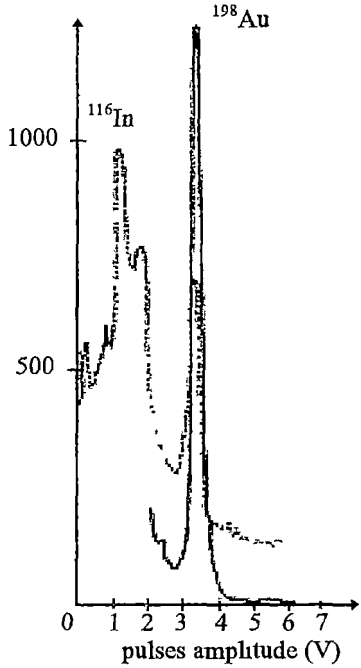

Fig 5. Radioisotopes ^{198}Au and ^{116m}In interference on the same 410 keV energy

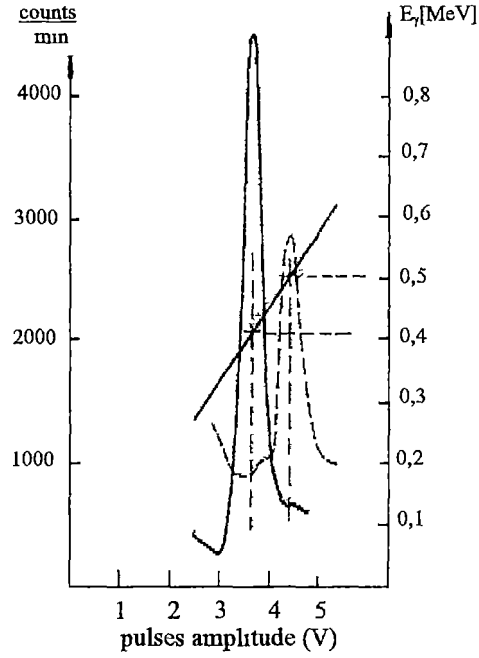

Fig. 6. Calibration line in the Au-Cu zone, makes the connection between the analysed impulses amplitude and the energy of the generating gamma radiation

Because the determined element concentration is directly proportional with the surface of the peak corresponding to the gamma radiation emitted of that isotope, it results that, if one can fit in a window from the electronic adjustment of the device, we can record only it self, determining in this way the intensity of the spectral line by counting the impulses produced by the gamma quantums.

This means that by adjusting the scales of the potentiometers of the impulse selector (in our case· 760 V probe tension and 24 x 2 dB amplification) one can determinate, for example, copper at a threshold of 4V and a 0 9 V window (fig 3) by counting for a preselected time of only 2 minutes, impulses with the amplitude between 4 0 and 4.9 V corresponding only to the 511 KeV energy emitted by the copper (fig. 6), the adjustment being made through the calibration line

For gold determination, the 410 KeV peak of ^{198}Au extends between 3 0 V and 3 9 V on the amplitude register of the monochannel selector-establishing in this way the window and the threshold of the device for the analyses. But the following thing happens· if the sample contains copper, and because this element is emitting nearly to the peak of gold, copper will introduce impulses through the inferior window, from the (3 0 + 0.9)V register (corresponding to gold) through the "Compton edge" effect, which it produces in the inferior zone of the spectrum (fig 7)

The problem to solve is how one can eliminate this interference because one can use no more the previously described technique for indium and silver, copper having a radioisotope with $T_{1/2}$ = 12 8 hrs (^{64}Cu) and if one waits for its disintegration it remains very little of the activity of ^{198}Au.

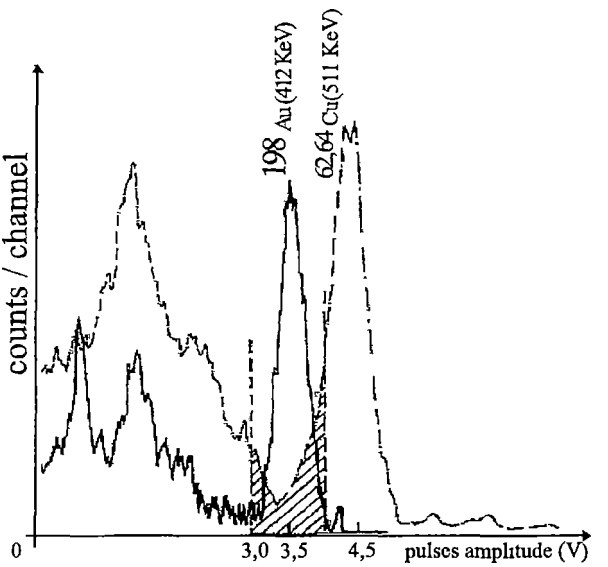

Fig. 7 The superposed spectrums of gold and copper It can be noticed how copper, in the right side of gold, introduces in the measuring zone of this, a Compton edge form istribution.

But from fig 7 can be see that the 410 KeV peak of ^{198}Au is right in the part between the 511 KeV peak of copper and the Compton edge corresponding to it, but the copper contribution in this zone isn't null

The question which occurs is. what are the conditions in which this contribution is null or, if it can't be eliminated, when can this contribution be rectified, i e extracted from the determined values for gold concentrations

By carrying out an investigation with a neutrons activied copper tablet, one can observe that the "valley" has a minimal value at a precise measurement geometry, exactly at a sample-detector distance of 1.5 cm (when the ratio photopeak-Compton edge is best too) (fig 8)

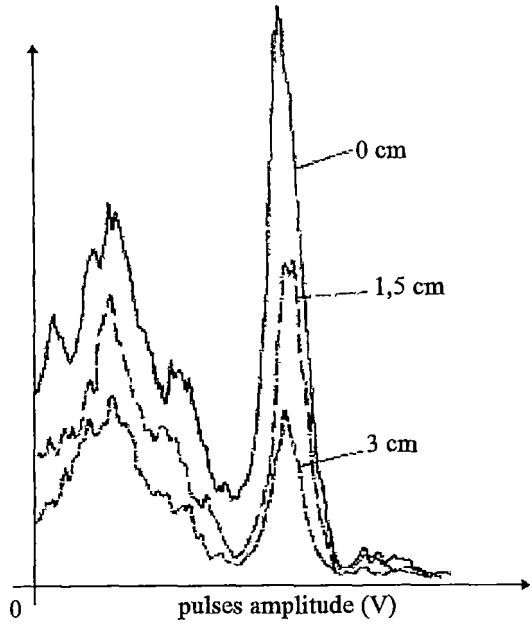

Fig. 8. The copper spectrum for different source-detector distance

If we built the ratio (for copper, fig 3) between the number of impulses counted through the gold window (3 0 – 3 9 V) arised from the pure copper, noted with $N_{Cu}^{Compton}$ and the number of impulses through the window which fits the photopeak of copper (4 0 – 4 9 V), noted with N_{Cu}, we will find a correction for the interference of copper at gold determination from other spectrums (figs 6 and 7)

For a spectrum of a gold and copper sample, from the impulses number N_{Au} of the gold photopeak one substracts the contribution of that copper which accompanied the gold, having N'_{Cu} on the photopeak and which interfers with the (3 0 – 3 9 V) of gold photopeak in this way

$$N_{Au}^{real} = N_{Au} - \frac{N_{Cu}^{Compton}}{N_{Cu}} N'_{Cu} \qquad (4)$$

In this manner one can make gold determinations in the presence of copper which accompanies it, even if this interfers in the gold window (see fig 7)

Therefore the correction is made numerical It must be standardized at fixed irradiation and disintegration times and of course, at the copper concentration from the sample The results at gold determinations are very precise.

The silver determination doesn't introduce such problems because it emits quantums of greater energy than gold and copper and so these elements can't influence photopeak of silver, with the condition that the splitting threshold of copper impulses sould be correctly chosen Therefore, in our conditions, according to figs 6 and 7, at a treshold of 5 V and a window of 1 V for the silver analysis on its two peaks of 630 KeV and 660 KeV, with the condition that copper should not prevail because than its peak extends

If it is so, the splitting threshold should be carefully increased because it occurs the risk to split the 630 KeV gamma spectral line of ^{108}Ag, too.

These adjustments and corrections being made, we passed to the N A.A of different archaeological gold and silver objects especially coins and jewels

N.A.A. of some archaeological objects The irradiating times were chosen this way for silver determination 1o minutes, for copper 24 hours and for gold 63 hours

The irradiating times are given by the expression

$$\frac{A_{sample}}{A_{standard}} = \frac{m_{sample}}{m_{standard}} \cdot \frac{1-\exp(-t_{ir\ sample}\lambda)}{1-\exp(-t_{ir\ standard}\lambda)} \qquad (5)$$

where A_{sample} and $A_{standard}$ are the radioactivities on the peaks corresponding to the analysed element, $A_{sample}/A_{standard}$ being equal to the ratio of impulses number $N_{sample}/N_{standard}$, read through the impulses selector window m_{sample} and $m_{standard}$ are the masses of determined element from sample and standard, λ - the radioactive constant of the isotope produced through neutrons irradiation of the analysed element The connection between λ and the half-life is given by the relation $\lambda = (\ln 2)/T_{1/2}$

If t_{ir} sample and t_{ir} standard are equals, formula (8) is reducing to formula (3)

For the analysis it have been used silver and gold chemically pure standards all the analysed samples being carefully weighed

First silver coins from the early Middle Ages, found in Transylvania have been analysed The results are given in Table 1

Table 1

Crt Nr	Coin type	Weight	Analysed content		
		(g)	Ag (%)	Au (%)	Cu (%)
1	Bela II (1131-1141)	0 423	88 5±11.5	0.7±0 1	7 0±1 1
2	Bela II (1131-1141)	0 396	89.5±10 5	1 3±0 2	9 5±1 4
3	Bela II (1131-1141)	0 383	87.8±12.2	1.6±0 2	9 5±1 4
4	Coloman (1095-1114)	0 791	87 9±12 1	0.3±0 1	8 9±1 3
5	Coloman (1095-1114)	0 368	97 2±2 8	0 6±0 1	7 2±1 1
6	Coloman (1095-1114)	0 624	82 4±12 4	0 7±0 1	8 1±1 2
7	Coloman (1095-1114)	0 343	97 8±2 2	0 4±0 1	9.0±1 4
8	Coloman (1095-1114)	0 351	86 6±13 4	0 3±0 1	9 1±1 4
9	Coloman (1095-1114)	0 437	95 8±4 2	0 4±0 1	4 4±0 7
10	Coloman (1095-1114)	0.774	83 4±12 5	0.7±0 1	9 0±1 4
11	Coloman (1095-1114)	0 483	83 4±12 5	0.6±0.1	9 8±1 5

Another analysed lot is made up of antique silver coins and jewels from Zalau Museum of History The results are shown in Table 2

Table 2

Crt.Nr	Archaeological object and the discovery place	Silver content (%)
1	Roman Denar (Magura Simleului)	86.9±13.0
2	Dacic Coin (Porolissum)	50 9±7 6
3	Roman Weding Ring (Porolissum)	100
4	Ear-ring (Magura Simleului)	74±11 1
5	Ring (Crasna)	77±11 6
6	Piece of silvered bracelet	7 8±1.2

Although it have been carefully studied all the extraction proceedings of interferences, the analysis is affected by errors between 10 and 15 percents. These errors can occur at silver determination because of massive diminution of radioactivity of ^{110}Ag isotope with $T_{1/2}$=24 sec although in the case of all the samples the disintegration time was standardized at 7 seconds.

One can notice an important fluctuation of the concentration in the case of repeated determinations on the same chain Other causes can be. faulty positions in the neutron flux of archaeological objects during the irradiation insufficient purity of standards thermal drift fluctuations of the monochannel selector's channels during the measurements

Conclusions Despite the difficulties, we succeeded in creating, by means of the above mentioned researches a N.A A. line for silver, gold and copper from a series of archaeological objects, a line that has already become a routine system

Acknowledgement. We would like to thank the Zalau History Museum and the National History of Transylvania Museum from Cluj-Napoca, for the furnished samples

We have benefited from discussions and suggestions from many of our colleagues, particularly Mr.A Ardevan our thanks are due to them also

REFERENCES

1. F Wideman, J Radioanal Chem , **55**, 271 (1980)
2 I Barrandon, J Radioanal Chem , **55**, 317 (1980)
3 C Cosma et al , Studia U B B , ser Physica, XXXI, 1 (1986)

4 L Daraban, C Cosma, T Fiat, J Radioanal Nucl. Chem Lett., **201**, 5, 447 (1995)
5 M Sælægean et al, în vol "First Romanian Conference on the Application of Physics Methods in Archaeology", 5-6 nov 1987, Cluj-Napoca, Romania, ed in 1988, pp 73-86
6 A Aspinal et al., Nature, **237**, 33 (1972)
7 O.W Thorpe et al, J Archaeol Science, **11**, 183 (1984)
8 K T Biró et al, Acta Archaeol Acad Sci. Hung, **38**, 17 (1986)
9 J L Joron, M Treuil, H Jaffrezic, J. Radioanal. Chem, **39**, 63 (1977)
10 A P Grimanis, M Vassilaki-Grimani, M.I Karayannis, J Radioanal Chem, **39**, 21-31 (1977)
11 J Diebolt, J C Ricg, J. Radioanal Chem, **39**, 9-20 (1977)
12 O Birgul, M Disksic, L Yaffe, J. Radioanal Chem, **39**, 45-62 (1977)
13 L Ryback, H U Nissen, in vol · Radiochemical Methods of Analysis, vol I, IAEA, Vienna, pp 105-107 (1965)
14 P A Schubiger, O Muller, W Gentner, J Radioanal. Chem., **39**, 99-112 (1977)
15 J Perdijon, *L'Analyse par activation*, Ed Masson et C-ie, Paris p 7 (1967)
16 I V Nednis, *Gamma izlucenie radionuclidov, primeniaemih v neitrons-aktivationom analize*, Ed "Zinate", Riga, p 139, 157, 159 (1987)
17 M A Bac et al, Izv Akad, Nauk SSSR, XXIV, nr 7, 818 (1960)
18 G Pálla, *Neutronfizika*, Ed Acad Kiado, Budapest, p 424 (1971)
19 Ch Chalauhi, E Hourani, Nucl Instr Meth, **200**, 553-560 (1982)
20 R VanLieshout et. al., Physica, **25**, 8, 703 (1959)
21 G Semenescu et al, *Fizica atomica si nucleara*, Ed tehnica, Bucuresti, 1976
22 B S Djelepov, A K.Peker, Shemi raspado radioaktivnih yader, Izd Akad. Naul SSSR (1958)
23 I A Kondurov, Y E Loginov, V V Martynov, P A Sushkov Izv Akad Nauk SSSR, ser fizicheskaya, **52**, 5, 864 (1988)
24 L Van der Zwan, Canad J Phys., **46**, 1527 (1968)

STUDIA UNIVERSITATIS " BABES-BOLYAI", PHYSICA, XL, 2, 1995

MANUFACTURING TECHNOLOGY OF THE Si(Li) DETECTORS

L.DARABAN[1], M D.CROITORU[1], V.SEVIANU[1], S.BOŞCĂNEANU[2], I CHEREJI[2]

ABSTRACT. Si(Li) detectors have been realized by compensating Si-p (ρ=600Ω cm) with Li ions The manufacturing technology is described in detail following the steps· mechanical processing of the silicon plates, chemical etching, lithium evaporation and diffusion together with the merit figures of the drifting and pasi-vation During the different steps, the detectors are tested by plotting the volt-amperic characteristic Finally X, α and β radiation spectrums have been obtained showing the performance of these detectors

Introduction. For measuring the energy of penetrating radiation (electrons, X and γ-ray, protons, etc) there is necessary to have a sufficient large sensible volume of detection [1] In the case of diffused p-n junctions there is a thick spatial charge region when the base materials have a large resistivity, because they work at large reverse potentials The obtaining of Si with large resistivity ($\rho \geq 10^4$ Ω cm) is a difficult technological problem and the reverse polarization potential that can be supported, before the excessive leakage currents, is about hundred of volts and depends appreciably on the surface conditions.

For example, the detectors with charged barrier at the surface where produced till now from Si-n,but recently, the using of the p-type silicon became advantageously [2] because.

1. Si-p can be produced with a better purity than Si-n, which is obtained by overcompensating the p silicon with n impurities and so the number of imperfections rises.
2 Si-p can be grown in monocrystals with low radial resistivity unlike Si-n
3. The thickness of the layer free of carriers in Si-p is approximately the half of the one formed in the p-type material for a given resistivity and reverse potential Simultaneous, the intensity of the electric field in the layer free of carriers for the p-type material, is larger and this is an important factor for the radiation spectroscopy
4 Si-p is a lot easier to obtain

A method to produce large sensible regions, starting with Si-p that has even low resistivity (ρ=10–100 Ω cm) is to compensate the carriers in excess, from a certain region of the base material, by doping it with lithium impurities (donor in Si) that has an activation energy of 0 03 eV[3]. By using this method, developed by Pell [4], the resistivity of

[1] *"Babeş-Bolyai"University, Faculty of Physics, Cluj-Napoca, Romania*
[2] *Institute of Isotopic and Molecular Technology, Cluj-Napoca, Romania*

compensated region might rise to $\sim 10^5$ Ω cm and its thickness may be over 10 mm A p-i-n structure is obtained This name comes from the presence of two junctions in the device. one, n^+–i, at the frontal surface and the other i–p on the back to the ohmic contact When a reverse potential is applied, the spatial charge region spreads very fast in to the "i" region and a subsequent increase of the potential value will not produce any variation of the thickness of the spatial charge region (and therefore of the semiconductor diode capacity) but only an intensification of the electric field that collects the charge produced by nuclear radiation ionization [5] Lithium is used for producing the p-i-n structures because the diffusion of other impurity type would mask the effect of the drift, when compensation is made on a bigger depth Being an interstitial impurity and having the largest diffusion constant, 10^7 times bigger[6] than that of the substitutional impurities (for example B or P) Initially, the acceptor ion is uniform distributed in the whole volume of the base material(Si-p) having an

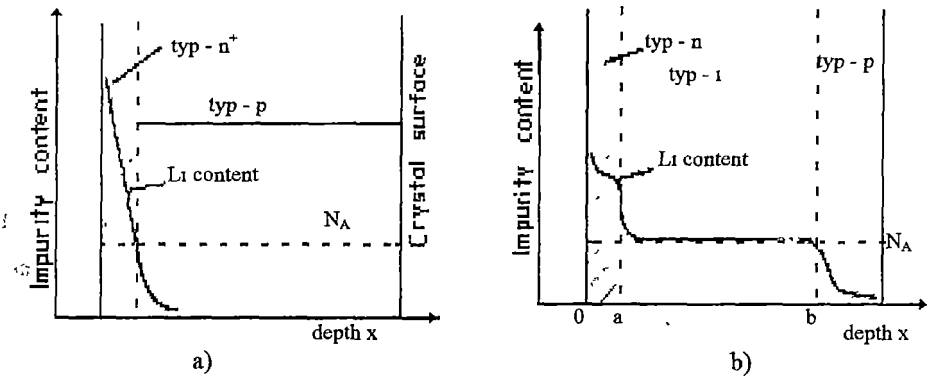

Fig. 1. Li ion distribution in Si-p. a) after diffusion, b) after Li ion drift

N_A acceptors/cm^2 level (Fig 1a)

By diffusing Li in to the surface (usually at temperatures between 350°–400°C) it will distribute into the crystal bulk by the law·

$$N_D = N_0 \exp\left(\frac{x}{2\sqrt{D_0 \cdot t_0}}\right) \qquad (1)$$

where D_0 is the diffusion constant of lithium in silicon, for the respective temperature and t_0 is the diffusion time

In this way, after a time t_0, a diffused linear graduated n-p junction is obtained, the plane of the stoichiometric junction being placed at a depth, x=a, from the surface (Fig 1)

If, to this junction, a reverse potential is applied (the second time) sufficiently high for the drift speed of the Li^+ ions to exceed the drift one, then the Li^+ ions are moved from the region rich in Li^+ ions to the region poor in Li^+ ions, through the region of the x=0 plane, where an electric field exists This ion movement is made with a reasonable speed in the when the temperature is sufficiently high, so the Li^+ ions have a considerable mobility Because Li has a great chemical affinity to oxygen, it is very important for the base material to have a low content of oxygen ($< 10^{15}$atoms/cm^3), otherwise, the ion mobility remains low, even at high temperatures, the oxygen impurities speeding up the precipitation of lithium and Cu impurities lowering it. The effect of copper (acceptor in Si), is very interesting, because he is an interstitial impurity (like lithium) and has great mobility [6] comparable with lithium's one, but with low solubility [7].

As a result of the Li ions drift in the proximity of the x=a plane (Fig 1), the uniformity of their concentration is produced at the $N_D=N_A$ level Indeed, if x<a, N_D can not be less N_A, because the acceptors in excess would modify the field configuration, so that $N_D=N_A$ For the same reason, an overcompensation ($N_D>N_A$) can not take place in the region x>a.

Therefore, an intrinsic region is produced between x=a and x=b (Fig 1b) whose thickness rises with the duration of the drift

It has been proved [1, 3, 5] that for constant potential V and temperature, the thickness compensated with lithium, d, varies with $t^{1/2}$, t being the time in which the drift was made

$$d = \sqrt{2\mu Vt} \qquad (2)$$

where m is the mobility, which depends on the temperature at which the drift was made.

We stress out that compensating the silicon by drifting lithium till the opposite surface can be used for building semiconductor detectors with charge barrier at the surface [8] and obtaining thus free of charge regions on large depths for the spectroscopy of the β radiation and high energy protons

Using the p-type front surface of the semiconductor detector as has the advantage of a better temporal response because of the difference between the mobility of electrons and holes [9] In this case the dead layer is lower than 0.05mm

Preparation of the start material. The selection of the start material is not so restrictive as to the surface charge barrier detectors because the acceptor impurities, indifferently of their concentration, will be easily disactivated by compensating with Li

Therefore, the publications that describe the manufacturing technology for the Si(Li) detectors present a large variety in choosing the resistivity r for the Si-p they use 100Ω cm [10,11], 50÷200Ω·cm [8], 200–600Ω cm [12], 10^2–10^4Ω cm [5], 40÷4 10^4Ω·cm [13] We have work with Si-p doped with boron (Romanian source) and having ρ=600Ω cm

The plates have been cut to the dimensions of 15x15mm^2, with a diamond disc Initially, the plates had a thickness of 3 mm and a plane surface with a roughness lower than 5mm after rectification of the silicon bar The crystal surface had to be well polished to obtain a uniform electric field Crystals grown after the <111> direction (parallel to the axis of the cylinder, the form under which the crystal is grown) are usually used, but other orientations may also be used [5].

To minimize the surface currents of the detector, the role of the center of the detector is separated from the margins by practicing a circular channel in the monocrystalin silicon plate and by building eventually, a guard ring [5,14] We have made a circular channel with a Ø=8mm diameter and 1 5mm deep, in the Si-p plate, with a wet 50μm abrasive metallic tube, (Fig.2)

After that, the crystal has been washed with double deionizated water and ethilic alcohol to remove the impurities generated during the mechanical treatment The Si-p was introduced after that in CP-4 (in a polyethylene vessel, a mixture was made containing the following parts 3.1 1 of HNO_3 HF CH_3COOH) for 2–3 minutes for chemical cleaning The plate was again washed in double deionizated water It is very important to avoid the contact of the plate with air because silicon fixes quick oxygen

Finally, the plate is stored in methanol (for avoiding contact with oxygen because lithium can be blocked at the surface of the crystal when reacting with oxygen) until lithium will be deposited on its surface

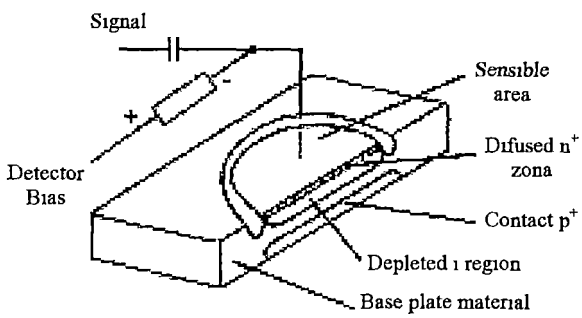

Fig 2. Cross section in Si(Li) detector

Diffusion of lithium.

Before realizing the intrinsic-compensated layer in Si-p by drifting lithium, it is necessary to build an n^+-p junction (n^+ means here that n is in excess) by the diffusion of lithium in to the material at high

temperatures Relation (1) gives [12] the diffusion time for a certain depth x=W established beforehand ·

$$t_{dif} = \frac{W^2}{2.4\ D} \tag{3}$$

where D is the diffusion coefficient of lithium in silicon at the working pressure. This coefficient can be calculated [13] with the relation

$$D_{Li \to Si} = 23\ \ 10^{-4} \exp\left(-\frac{15200}{RT}\right) (cm^2/sec) \tag{4}$$

or may be taken from table [6]

There are a few techniques for the diffusion operation of lithium One of them consists in the painting of the crystal surface with a mixture composed of metallic Li in suspension in mineral oil or vaseline, followed by an external heating (in a glass capsule with shlif) in argon stream The heating had to be made in two steps the first till 250-270°C to evaporate the oil and the second till 400-450°C for 5 minutes to diffuse the metallic lithium layer left (186°C m p) after the first heating step. This technique was used at large [4, 10, 11, 15-17] and we have used too at the beginnings, but we found out that, during the diffusion process, some little holes, like craters, arose on the silicon surface, which led, finally, during the short chemical attack with CP-4, to a nonuniform detector surface, because the corrosion rate depends on the lithium concentration on the surface The evaporation of lithium in vacuum, followed by diffusion, leads to a better quality of the surface layer [5, 8, 12, 13, 18-20], but this method is more complicated than the first Lithium is evaporated in vacuum better than 10^{-5} torr followed by a diffusion process in nitrogen atmosphere [8] at temperatures between 350°C and 400°C. We have successfully used this method, but prudence measures had to be to be taken against the spreading of metallic lithium out of the evaporation tantalum boat when connecting the heating current The lithium was pure and stored under argon. Evaporation started with a prolonged heating at a temperature under the melting point, followed by the evaporation process at (1372°C=b p of Li) The silicon plate was heated with an electric furnace heated at 350°C and a Pt-PtRh thermocouple was attached also to the plate The diffusion time was 5 minutes and the obtained diffusion depth was 0 1mm thick in the inner of the circular channel (Fig.2) The cooling had to be done very rapidly by turning the heating off and feeding pure argon in the bell jar after closing the high vacuum way After the diffusion process has ended the lithium in excess is washed in methanol The surface has to be smooth and matted; a metallic view shows the presence of insufficient diffusion and the diffusion process must be renewed. The plate must be stored in pure methyl alcohol, so the interstitial diffused lithium will not react chemically till the

ohmic contacts will be deposited (Usually gold contacts are used [5]) We deposited gold on both sides of the silicon plate (70mg/cm^2) by using a mask having the same window as for the deposition of lithium and the plate was heated at 100°C for obtaining a better adherence

We have noticed that the deposition of Al as drift contact is better because the aluminum film does not exfoliate at the drift temperatures(130°C) in the oil bath

In the literature there are some examples of using Ni contacts much durable than gold [13, 15, 18, 19] but difficult to obtain We made some attempts to obtain these contacts through a chemical method, the way it is described in [18,19], but they were to thin so we did not trust them

The n^+-p junction may be tested [16] by capacity and reverse current measurements but it is difficult to define a merit figure at this fabrication step, the basic requirements for good detectors being low potentials over the detector and big reverse current We tested the junction by making its potential vs current characteristic (Fig 3).

The drift of Li ion in Si-p. Like we sad before, the transport of the Li^+ ion from a crystal surface to another is made by polarizing properly (plus pole at the diffused contact) the junction The operation is made under controlled temperature conditions, in continuous current and by controlling the drift current, because a current density bigger than 50mA/cm^2 breaks through the junction The thermal running is very important If the junction is introduced in a silicon oil bath [11,22], the temperature in the central zone is bigger than the temperature of the extremities and so a slightly curved compensation profile of the impurities in the crystal is obtained Silicon oil, might be substituted with n-hexane [15] or liquid fluorocarbon [10] and used at their boiling points A plain layer compensated through drift can be obtained if both faces of the are maintained at high and constant temperature[5,16-19] between two metallic plates. These systems hold the drift

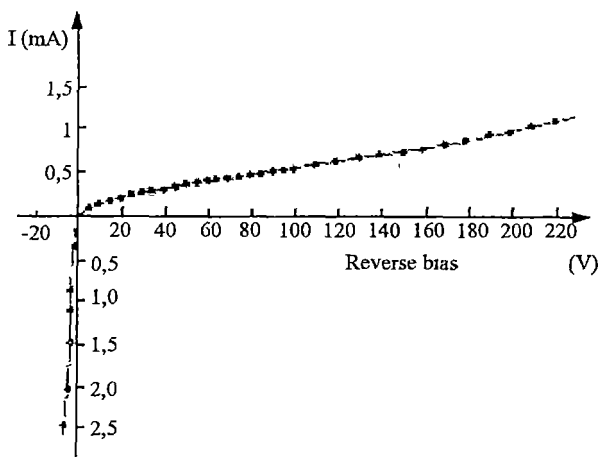

Fig. 3 . Volt-amperic characteristic of the detector after lithium diffusion

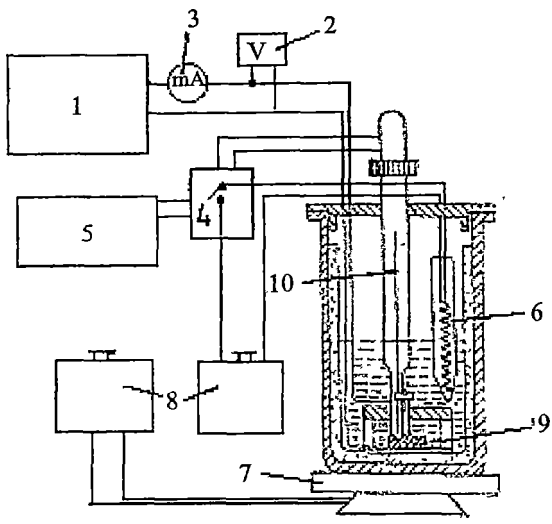

Fig 4. Experimental arrangement for drift in silicon
1-cc power supply Statron 4208, 2-voltmeter, 3- miliampermeter, 4-electronic command circuit of the heating, 5-power supply of the command circuit Multistab235, 6-heating resistor, 7-preheater, 8-autotransformers, 9-silicon plate, 10-contact thermometer

current at fixed values controlling the temperature or the power and disconnecting the system when the drifted region reaches the back of the plate It is also necessary to control the depth the Li ions have reached during the drift because if lithium would get to the opposite face it would form there an n-i-n structure When such a junction is polarized, one of the i-n junctions would be directly polarized and the other reverse polarized and the injected current given by the direct polarized junction would rise very much the noise of the detector. A sudden rise of the reverse current through the device may be used as an indication for the total compensation, followed by a redrift process

One of the methods for finding the depth of the lithium ions is to use the formula (2) But because during the drift the potential and the temperature have small variations and the concentration of the acceptors is not uniform, this method gives only approximate results Another method is to determine the depth of the compensated region by stooping periodically the drift for measuring the inverse current, noticing a reduction of the blocking current and a flattening of the characteristic line or by measuring the capacity of the junction at room temperature, because it is reverse proportional to the depth of the compensated zone[16] Other techniques, like the chemical one (plating with copper), are synthesized in paper [23]

For realizing the compensation with lithium, the detector has to be kept in a medium free of oxidant agents and heated at the drift temperature We used the method of drift at constant power [11, 22], using a apparatus where the crystal is placed in silicon oil (Fig 4) The crystal was mounted in a device and fixed with a screw and teflon isolators The whole ensemble was sank into a razoterm glass containing silicon oil and after that in brass container, to protect the detector from light when checking the potential v current characteristic during the different steps of the manufacturing The silicon bath contains also a

heating resistor(supplied from a autotransformator at 10V), closed in a quartz tube, working only for fine adjusting of the temperature and a contact thermometer preset for 130°C The container is seated on a electric boiling ring supplied by a autotransformer at 140V. The Si crystal will be polarized with drift potentials between 50V and 200V. The heating system has a precision of ±2°C when the drift power consumed by the detector is constant although the resistivity of the material rises. The depth of the compensated region can be calculated by using the nomogram in Fig 5 that was taken from [24]

Table 1 presents a state of the parameters of the apparatus during the drift and the depth of the compensated region in a Si plate, calculated with the nomogram (Fig 5)

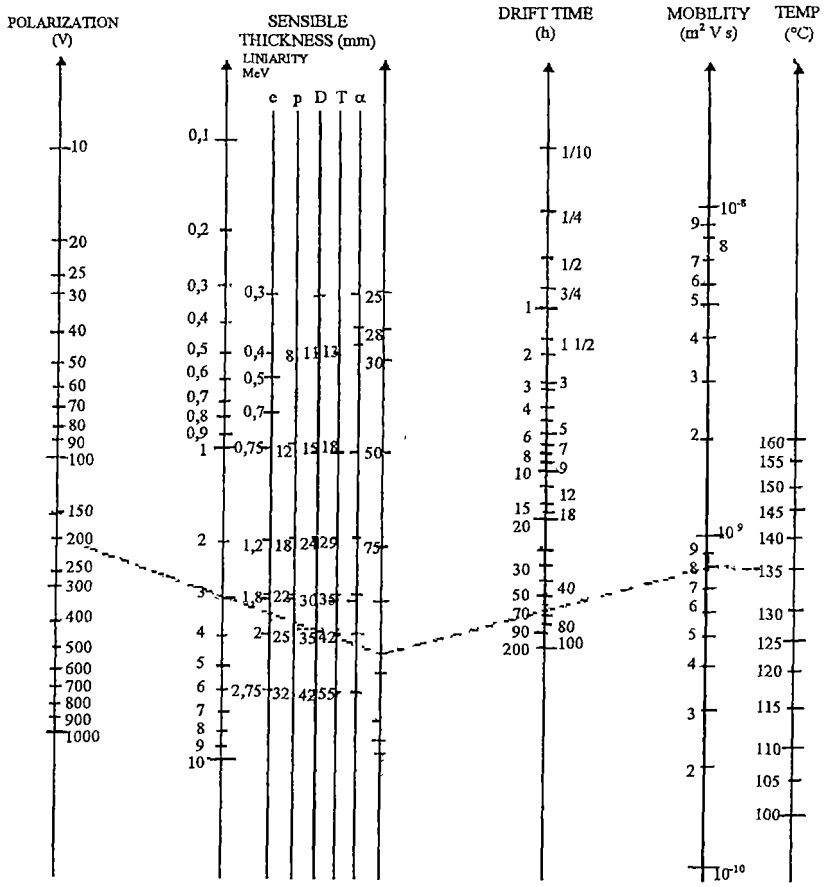

Fig. 5. Nomogram for the lithium compensation of the silicon detectors

Table No.1

Drift time intervals (h)	Reverse potential (V)	Drift current (decreasing) (mA)	Thickness of compensated region (mm)
2	50	20-16	0 2
2 5	70	25 5-20 5	0 27
2.5	90	25-24	0 29
1	100	19-16	0 2
3	100	15-9.5	0.4
2	150	16-14	0 35
1 5	200	24-18.5	0 3

total time.13 5h total thickness. 2.01mm

We have noticed that during the drift time in oil the detector was impurified, so we had to do a short cleaning with CP-4 and to redeposit the contacts for continuing the process

Between the different steps of the drifting some characteristic of the detector have been taken, to control the compensation with Li ions The final characteristic of the p-i-n diode looks very good (Fig 6).

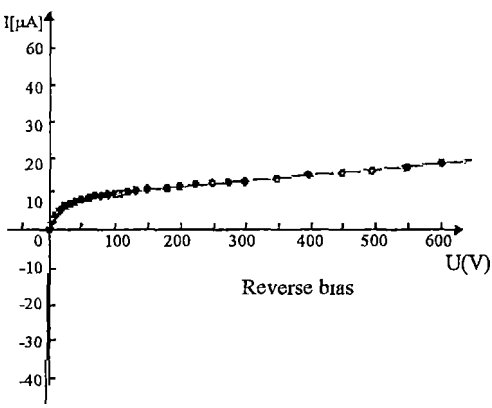

Fig 6 Volt-amperic characteristic of the Si(Li) detector at room temperature

The final step, after drifting, to improve the quality of the detector, is the clean-up operation. The Li^+ ions in excess (which did not pair with an acceptor atom) are brought back to the face n of the crystal For doing this, the detector is polarized with the plus pole on face p and minus pole on face n (the face through which Li was diffused) The potential applied during the clean-up was between 50V and 500V The temperature must not exceed 100°C, because over this limit, the bond between Li and acceptor impurities is destroyed by the thermal agitation and the then all lithium atoms are brought back During the clean-up, the current decreases because

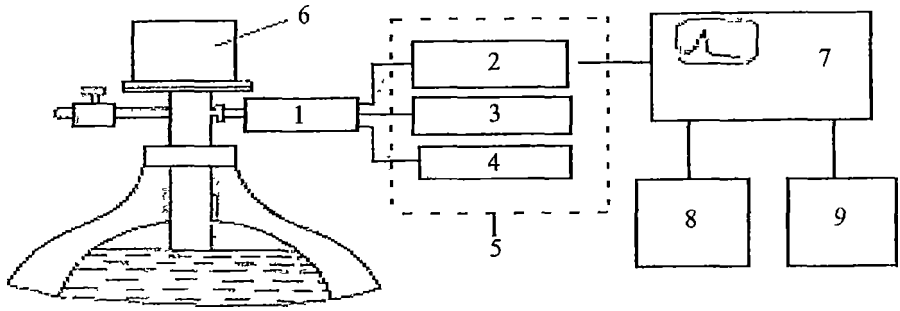

Fig. 7. Block scheme of the spectrometer with cooled Si(Li)

1- preamplifier type 1141FAN , 2- spectrometric amplifier type NE4658, 3-high voltage power supply type 1135FAN, 4-power supply for the preamplifier, type 1112FAN , 5- standard power supply type ST614 , 6- Si(Li) detector mounted in a cryostat with Be window , 7- multichannel analyzer type NTA1024 , 8-printer type NZ291 , 9- plotter type NE230

the resistivity increase The clean-up operation has to be done until the stabilization of the current is noticed

We kept a potential of 50V and a temperature of 100°C for several hours and after that, the potential was risen to 200V at room temperature After the clean-up operation, the quality of the detector has improved, the reverse current measured at 100V being 1mA We infer from this that the original silicon crystal was overcompensated ($N_D > N_A$)

The mounting of the detector was made as follows. fine silver wires where stuck with silver paste on the ohmic contacts, the other ends of the being soldered to gilded connectors, mounted on a polyethylene box On the back of the detector a metallic piece(pin-plug) was stuck with silver paste, for cooling

Testing the detector to nuclear radiation. The resolution of a detector depends on the signal to noise ratio By cooling the semiconductor detectors, the noise current due to the thermal generation of free carriers decreases very much The Si(Li) detector must not be cooled but during working and can be stored at room temperature unlike the Ge(Li) detector that has to be maintained cool all the time We cooled the Si(Li) by two methods · when measuring the charged particles, the cooling has been made with a Peltier element at -20°C (the Peltier cell is sufficiently, because the measured signals are large enough) , in other tests, a cryostat with a Be window (0 1mm thick and having a diameter ∅=10mm) was used, that cools the detector to liquid nitrogen temperature. The problem of constructing such cryostats is described elsewhere [25-29] The detector was mounted on the cold finger in the cryostat which was outgased in vacuum by heating it for 3 hours and than introduced in liquid

nitrogen in a dewar vessel when the final vacuum was 10^{-6}torr The first test was performed with the detector in X-rays (or low energy γ-rays) of 60keV, emitted by ^{241}Am Experimental setup is shown in Fig 7.

The detector was polarized with 600V and after cooling the low energy g-rays spectrum was taken (Fig 8)

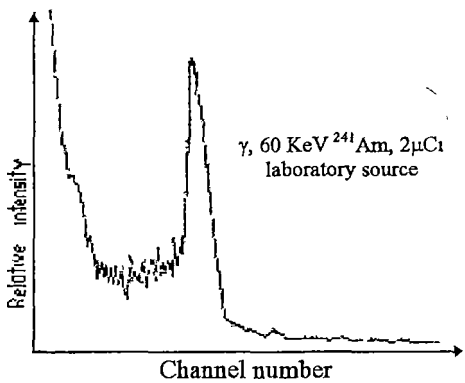

Fig.8. The spectrum of the 60keV γ-rays from ^{241}Am detected with the Si(Li) detector

The resolution of the detector was established to be 7keV at 60keV. We must mention that the signals generated by the radiation are very low and because of a 50 Hz electronic noise which generates microfonics, measurements at energies lower than 40keV where disturbed This noise is hard to eliminate because it is generated by the magnetic component of the electric network so the tests had to stop here

We noticed that the successive chemical attacks with CP-4 made the window so thin that a particles could be detected under certain conditions (Fig 9)

The signal produced by the α particles is larger and can be easily discriminated from the 60keV radiation background of the ^{241}Am source This test is enough to demonstrate how thin the entrance window on the n face of the detector is, because otherwise the 5 5 MeV in Fig 9 would have a "tail" This means that this detector could be used also for detecting a particles or protons generated by reactions with rapid neutrons in a target mounted in the front of the detector As a matter of fact our detector is sensing also electrons (Fig 10)

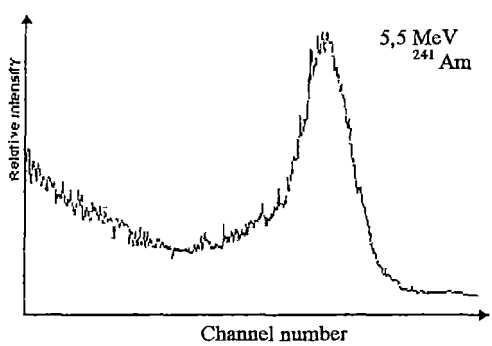

Fig. 9. The spectrum of the 5 5 MeV α particles from ^{241}Am detected at room temperature trough the thin window on the n side of the Si(Li) detector

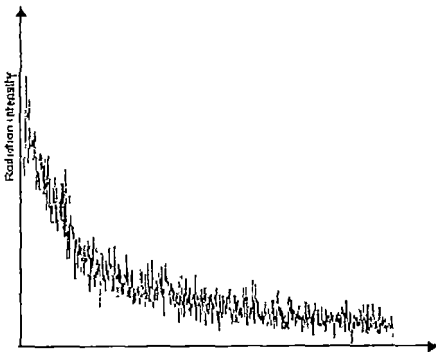

Fig. 10 The β spectrum from a ^{137}Cs source, measured differentially

Conclusions. We described in detail the manufacturing technology of the Si(Li)detectors The detectors realized through this method are very good for detecting X and low γ-rays, α and β particles The detectors are stable in time and their working service time is of a few years.

REFERENCES

1 D N Poenaru and N Vîlcov, *Măsurarea radiatiei nucleare cu dispozitive semiconductoare*, p 206, Ed Acad Bucuresti, (1967)
2 P J Matew and N G Chapman, Nucl Instr Met , **49**, 245 (1967)
3 S Deme, *Semiconductor detectors for nuclear radiation measurement*, p 60, 81, 94, 170, Ed Acad Kiadó, Budapest (1971)
4 E M Pell, J Appl Phys , **31**, 291 (1960)
5 F S Goulding, Nucl Instr Meth , 43, 1 (1966)
6 B I Boltaks, *Diffuzia v poluprovodnikah*, p 212, Gostatomizdat, Moskva (1961)
7 W L Hansen and B V Jarriet, Nucl Instr Meth , **31**, 301 (1964)
8 H M Murray et al , Nucl Instr Meth , 40, 330 (1966)
9 G Dearnaley and A B Whithead, Nucl Instr Meth , **12**, 205 (161)
10 C Chasman, J Allen, Nucl Instr Meth , **24**, 253 (1963)
11 C A J Ammerlaan, K Mulder, Nucl Instr meth , **21**, 97 (1963)
12 O A Matveev, C M. Rîbkin, At Energhia. **16**, 356 (1964)
13 C A Azimov et al , *Dinamiceskie haracteristiki neodnorodnîh poluprovodnikovîh struktur*, p 58, Izd FAN Uzbesk SSR, Taøkent (1975)
14 I I. Samueli et al , *Instrumentatia electronică în fizica nucleară*, p. 77, Ed Tehnică, Bucureşti (1972)
15 G Farzine et al , Kerntechnik, **15**, 27 (1973)
16 G Bertolini et al , Nicl Instr Meth , **32**, 86 (1965)
17 J H Elliott, Nucl Instr Meth , **12**, 60 (1961)
18 G Dearnaley and J C Lewis, Nucl Instr Meth , **25**, 237 (1964)
19 R A Ristener et al , Nucl Instr Meth , **56**, 55 (1967)
20 P E Gibbons, Nucl. Instr Meth , 16, 284 (1962)
21 W Schuler, Nucl Instr Meth , **60**, 278 (1968)
22 J W Harpster, Nucl Instr Meth , **48**, 175 (1967)
23 H J Erramnspe, Nucl Instr meth , 78, 175 (1970)
24 * Detecteurs semiconducteurs, Ed LA RADIOTECHNIQUE-COPRIM-RTC, p 145 (1966)
25 S Buhler and L Marcus, Nucl Instr Meth **50**, 170 (1967)
26. C Chasman, R A Ristenen, Nucl Instr Meth , **34**, 250 (1965)
27 C E Miner, Nucl. Instr Meth , **55**, 125 (1967)
28 J F Detko, Nucl Instr. Meth , **94**, 395 (1971)
29 R E Turcotte and R B Moore, Nucl. Instr Meth , **72**, 210 (1969)

STUDIA UNIVERSITATIS "BABES-BOLYAI", PHYSICA, XL, 2, 1995

LOCAL PLASTIFICATION OF HARD SHELLED SEMI-PRODUCTS

BICA IOAN[1**]

ABSTRACT. The work presents the experimental results concerning the local plastification with plasma of Diesel motor cylinders, using a specialized plasma generator

Description of the procedure Cylinders of Diesel motors are obtained through centrifugal chill casting of grey cast iron FCX 250 The marginal surfaces of the cylinders have surfaces of the high hardness (HB 250), for the reason the machine is operated under heavy duty

It is known [1] that the tensile strength of metals and metallic alloys decreases due to

$$\sigma_r = \sigma_{r_0} \bullet \exp\left[-m\left(\frac{T}{T_t}\right)^n\right] \tag{1}$$

temperature, pursuant to the law such as

where·

$\times \sigma_{r_0}$ -tensile strength of metal (or of the alloy) at environmental temperature,

$\times T_t$ -melting temperature of the metal,

$\times m$, n material constants,

In case of alloy steels, high alloy steels, cast iron etc the above mentioned material constants (1) have the values [2].

$$m = 12.5 \ , \ n = 3$$

According to (1), the main cutting force F_z decreases exponentially with the metal temperature T increases [1,4,5]

$$F_z = F_{z_0} \exp\left[-m\left(\frac{T}{T_t}\right)^n\right] \tag{2}$$

where

---

[1] *University of Timişoara, Faculty of Physics, Romania*

**The paper has been financed by ISIM Timisoara, Bv.Mihai Viteazu nr 30a (contract 1647/1088)

F_{z_0} main cutting force at ambient temperature.

Therefore that force F_z is a measure of the local plastification of the metal. The local plastification of the metal is obtained with plasma (Fig. 1). The plasma generator 1, with transferred arc, supplied by direct current from the current source 2, warms up locally (part MN)

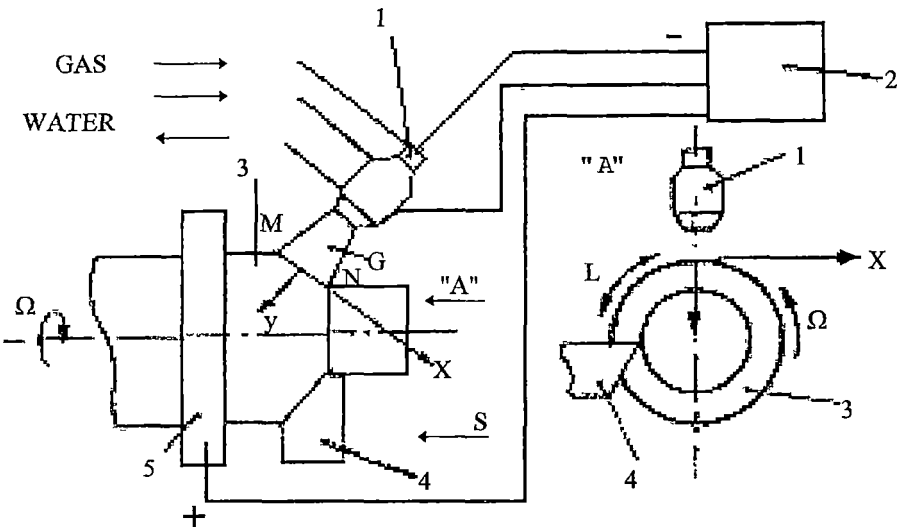

Fig. 1 Block diagram of the equipment used at the local plastification of hard shelled semi-products, Ω - circular speed of the semi-products.

the semi-product 3

The cutting tool roughs on a breadth b = MN and a pre-set depth T, the surface of the semi-product. The advance S of the cutting tool is the same with that of the plasma generator. The positive terminal of the current source is connected to the collector brush 5. So the electric circuit is closed and therefore the electric supply of the plasma (position 6 in Fig 1)

The distance on the circumference of the semi-product between the plasma generator 1 and the cutting tool 4 is L

The theory shows that in case of a plasma generated by a DC electric arc with a circular anode spot, the temperature distribution in the coordinates x and y (Fig 1) is as 5·

$$T(x,y) = \frac{0\ 16P\eta}{\lambda L}\sqrt{\frac{a_0}{a_0 + k_1}}\exp(-10^4 \bullet k_1 y^2) \qquad (3)$$

where

P - power in plasma

η - local heating efficiency

λ - thermic conductibility of metal.

The magnitude a_0 is the (confinement) coefficient of the plasma

It depends on the intensity E of the axial electric field, the electroconductibility σ_0 of the plasma and on the intensity I of the electric discharge current [5]

$$a_0 = \pi \sigma_0 \frac{E}{I} \tag{4}$$

$$k_1 = \frac{v}{4\omega L} \tag{5}$$

The maximum of k_1 is obtained from [5]

where

v - tangent speed of the part,

ω - thermic diffusibility of the metal (or of the alloy)

It can be noticed in (3) that the reaching the temperature T at the plastification of the metal is conditioned by the power p of the plasma, nature of plasmagenous gas through σ_0, the distance generator - machine part through the election of the dimension E, on the material of the semi-product through ω and λ and respectively on the position of the plasma generator set for the cutting tool by the dimension L

The plasma generator. The plasma generator is designed for the conversion of electric energy given by the source in thermic energy of the plasma.

In Fig 2 we see the plasma generator used at the local plastification of hard shelled semi-products.

It consists of two groups of different elements electrode 1 with fixing tweezers and the cooling chamber 3, and respectively the nozzle 4 with the cooling chamber The two compounds are isolated one of the other through the ceramic insulators 6 and 7 The plasmagenous gas (argon) penetrates through the pipe 8, pressure is equalized in the equalization chamber 9 and then it comes out into the space electrodenozzle through the space between the tweezers 2 and the cooling chamber 3.

The pressurized cooling water is introduced through the tube 10, and then arrives through ramifications into the cooling chambers 3 and 4 The water out of the cooling spaces is evacuated

by tube 11 Spacers 12 maintain equidistant the plasma generator water and gas supply tubes

The protection of the generator compounds occurs through metal sleeve 13, insulated by the nozzle trough an insulation of mica (position 14 in Fig 2) The plasma generator flexible pipes are protected by the metal case 15 It's small size (see Fig 2) allows it's utilization for the

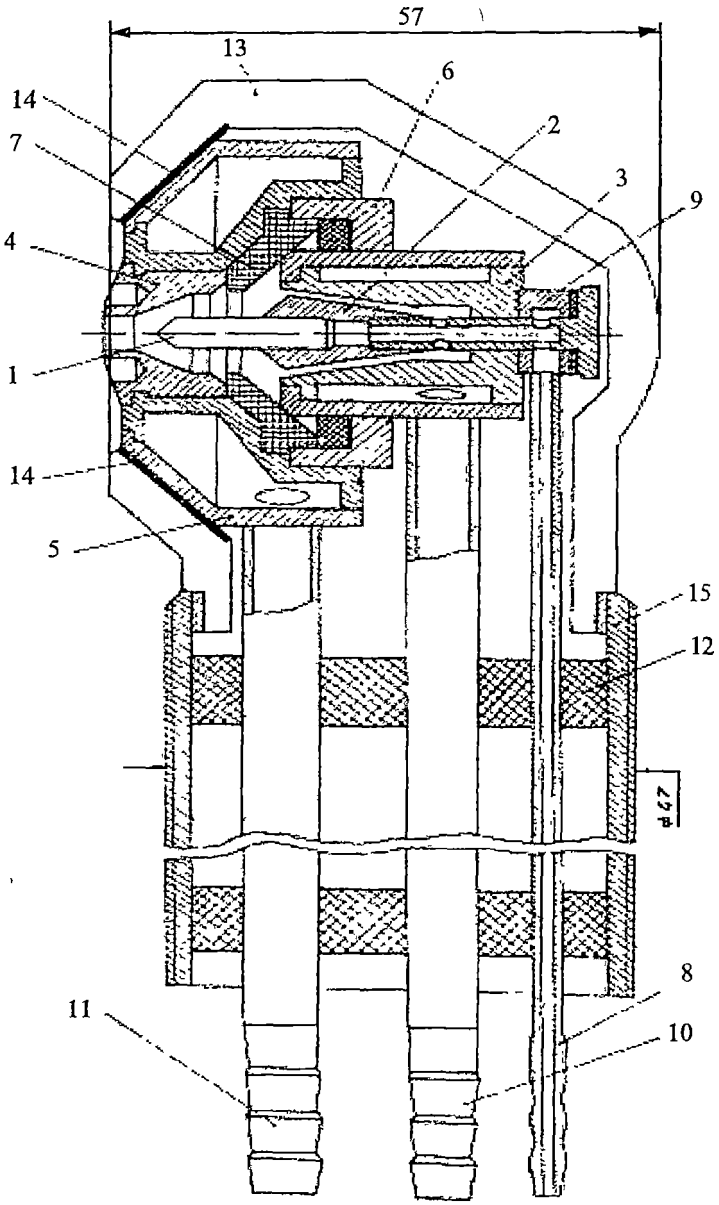

Fig. 2. The plasma generator

local plastification with plasma, inside Diesel's cylinder sleeves

Experimental results and conclusions. The testing equipment used at the local plastification of marginal surfaces at Diesel cylinder sleeves is shown in (Fig 1). The plasma generator used is shown in (Fig 2)

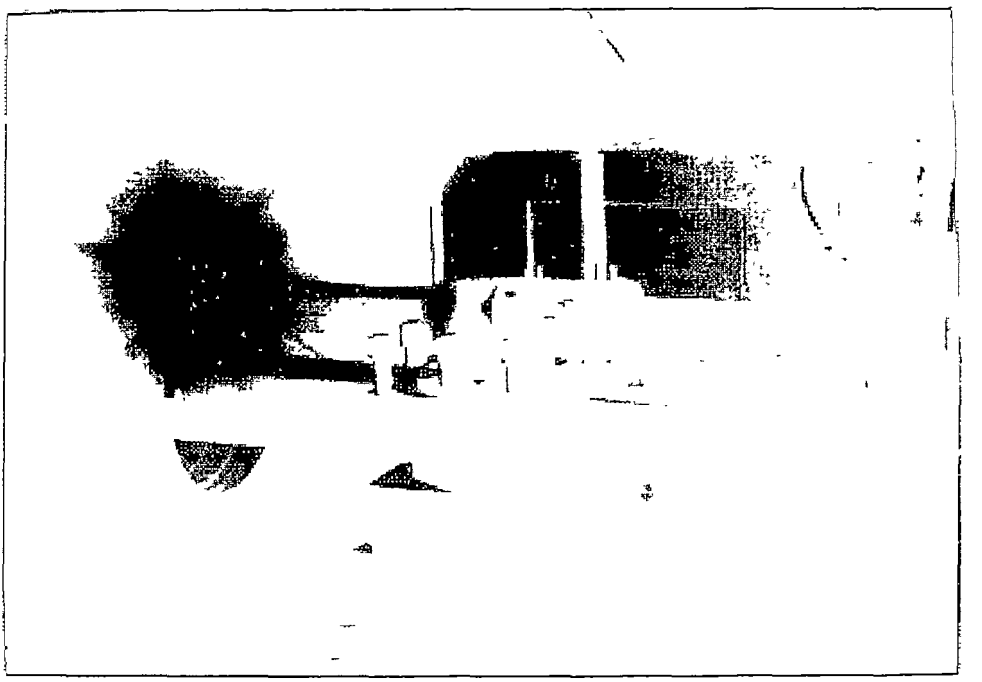

Fig. 3. Aspect during the local plastification with plasma, inside the semi-product Diesel engine cylinder sleeve

Figure 3 shows an aspect during the experiments The diesel engine cylinder sleeve is sized 240 / 209x460mm It is casted centrifugally according to the MAN 380 3 standard having at surface a hardness of at least 250 HB. The plastification temperature of the material is about 900K [5]

For measuring the main cutting force, as a measure of the materials plastification, it has been used a lathe tool having inside tensometric sensors (Fig 4). The machine-tool used is of type SP 630 The lathe tool is reinforced with plates 2 of metal carbide K 10 [3,4]

Into the tool's body are practiced a transversal and a longitudinal aperture The first one is necessary for the emplacement of the sensors, and the second one is designated for the afferent lays. The assembly in (Fig 4) foreseen with the spring gaiters 3, holding screws 4 and 5 and respectively the socket bung 6 The connecting diagram between the socket bung 6 and the sensors is shown in (Fig 5), strain gauges (tensometric sensors)

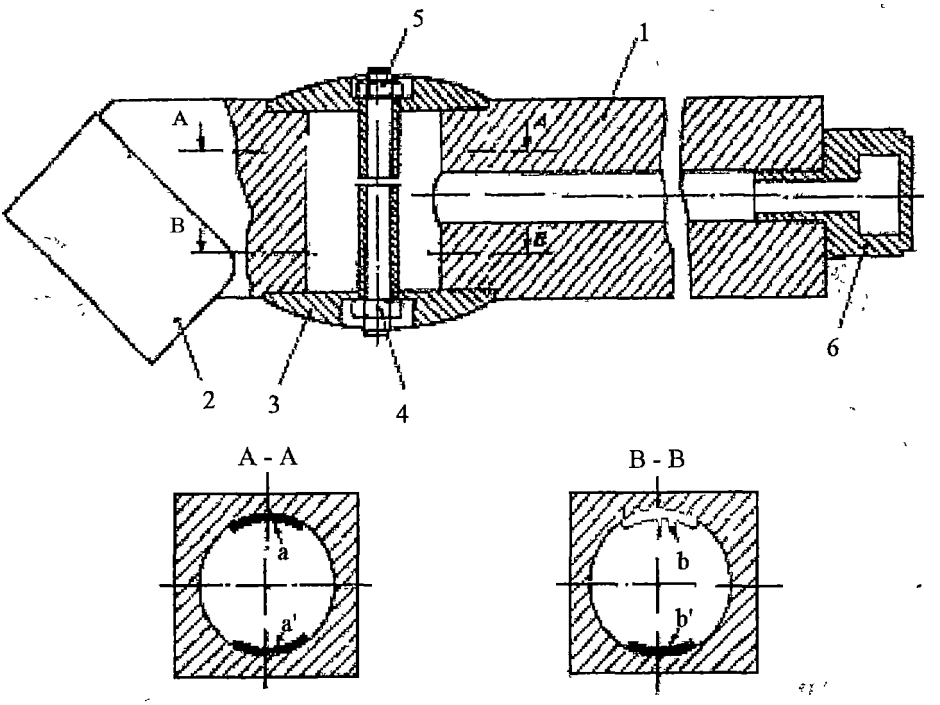

Fig 4. Lathe tool fit out with tensometric sensors

The signal received from the tensometric bridge is processed by a recording amplifier, prior gratuated

At a argon plasma power (151/min) of 13 KW, obtained with the plasma generator in Fig 2 (nozzle diameter of 6 mm) the cutting force decreased from 356 51 daN to 230.56 daN (Fig 6).

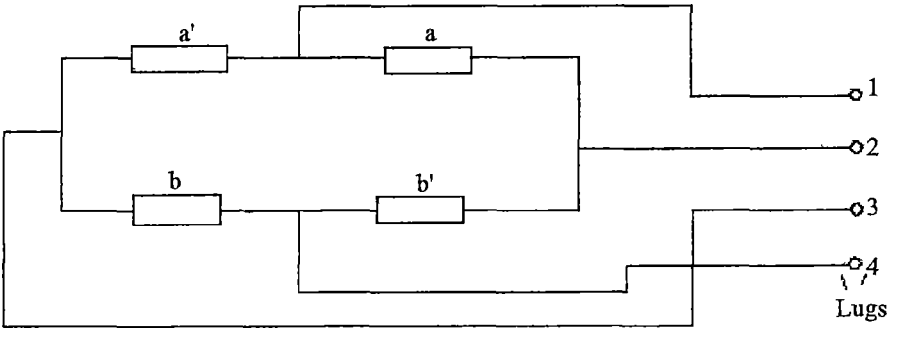

Fig. 5. Connecting diagram of the strain gauges in order to measure the force F_z

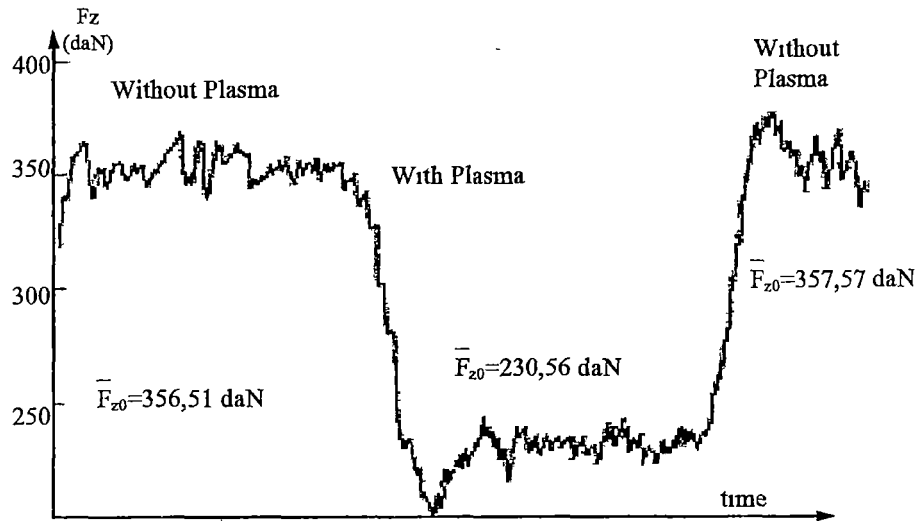

Fig. 6. Time emphasizing of the cutting forces at plasmaless machine processing (F_{z0}) and respectively at machine processing using plasma (F_z)

We remark that the semi-product in the tool-machine jaw has a speed $\Omega = 40$rev / min, the advance of the cutting tool is of 0 28 mm/turn and the cutting depth is $t = 4.5$mm In the impact zone plasma - metal the measured temperature is 1473 K.

The roughing zone remains at a temperature of about 400 K.

Of (Fig 6) it can be observed that the metal is plastified in plasma and the main cutting force decreases with about 46 %

Acknowledgements Thanks to Mr Cheveresan Traian, main researcher at ISIM Timisoara for the realization of the plasma generator and respectively to Mr Grigoriu Theodor, main researcher for the performing measurement for the cutting forces.

REFERENCES

1 D N Klauci, *Energomasinostroemie*, 7 (1984), 26 - 27
2 A N Reznikov, *Energomasinostroemie*, 11 (1981), 26-18
3 I Bica, T. Udoi, T Grigoriu, Symposium "Tehnologii neconventionale", Baza Academiei Romane, Timisoara 30-31 may 1986 Proceedings pag 123-128
4 I Bica, G. Mucsy, T Udoi, Symposium "SITNECI" Birlad 1988, Proceedings pag 255 - 262
5 I Bica, Doctoral thesis, University of Timisoara 1991






STUDIA UNIVERSITATIS "BABES-BOLYAI", PHYSICA, XL, 2, 1995

STUDY OF WIG ARC STARTING IN AC

I. BICA[1]

ABSTRACT. The paper present the experimental research about ignition and stability of the WIG arc in AC

Theoretical introduction The WIG arc is an electrical discharge in an inert gas medium, between a wolfram electrode an a metal piece (Fig 1) The pressure of the inert gas is at least equally to the atmosphere pressure In AC the wolfram electrode and also the metal piece are connected at the output of a step-down transformer (380 V_{ac}/ 80 V_{ac} with a descendent characteristic "V - A") (fig 1) From electrical point of view the arc WIG in AC shows a capacitive character impedance

$$Z_a = R_a - jX_a \tag{1}$$

where

R_a = ohmic resistance

X_a = arc reactance

The voltage U_a applied to the arc WIG determinate the appearing of a current of intensity I_a along the arc As a consequence of the phenomena between the electrode 1 and 2 the ionized gas is transformed into plasma (pos 3 - Fig 1) The current I_a through has a time variation similar to that of voltage U_a At passing through zero of I_a the arc WIG extinguishes

Reignition of the WIG arc requires a starting voltage [1,2]

$$U_z = V_i \bullet \frac{p \bullet d}{A + \ln(p \bullet d)} \tag{2}$$

where

V_i = ionization potential of the inert gas (V_i = 13,56 V - for Argon)

p = pressure of the inert gas, torr

d = distance between the electrodes, mm

A = a constant depending of the nature of electrodes and also of the plasmagenous gas

The dependence of the starting voltage U_z from the product between the pressure p of the

[1] *University of Timisoara, Faculty of Physics, Romania*

inert gas and and the distance d between the wolfram (W) Nickel (Ni) resp of iron electrodes is presented in (Fig 2)

At metal processing by arc WIG the minimal distance between the Wolfram electrode and piece has to be d > 3 mm. From Fig 2 it yields that the voltage U_z in Argon, at a pressure of 760 mm Hg is of about 3 KV and linearly with d The U_0 voltage of the current source respectively voltage of the current source respectively voltage U_n on the arc WIG meet the condition.

$$U_0, U_a \gg U_z \tag{3}$$

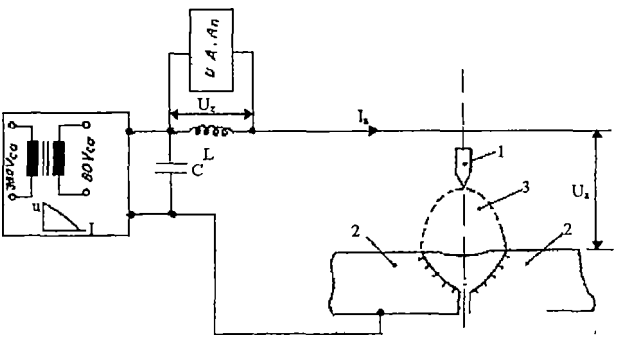

Fig 1. Basic electrical diagram for AC supply of the arc WIG

As a consequence of the inequality (3) the arc WIG does not start For starting the WIG arc in AC it is required superposing a voltage U_z over the voltages U_0 and U_a of a WIG source, as shown in Fig 1 For protection of source WIG, the signal U_z has to be of high frequency (f>1 MHz) The elements L and C (Fig. 1) protect the WIG source from the high frequency signal given by the arc starting device (D A.Ar)

AC WIG arc starting device. The basic electrical diagram of the AC WIG arc starting device is presented in Fig 3 The operation mode of D.A Ar, referring to Fig 3 is as follows The device presented in Fig 3 is fed at a voltage U_{a1} = 220 V_{ac} The static contactor with triac V_6 conducts when the voltage on the capacitor C_1 reaches the starting voltage UB_0 of the diac V_5 - as well in the

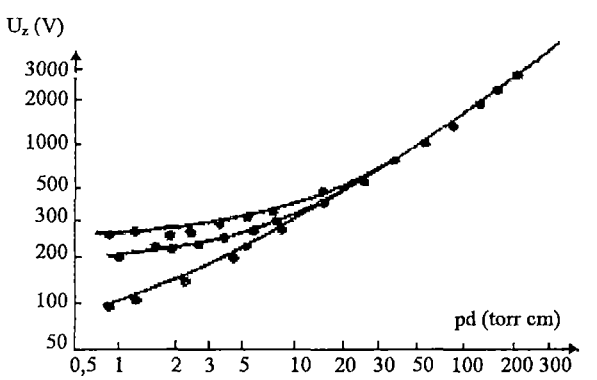

Fig. 2. Dependence of the starting voltage U_z of the product between the pressure p of the inert gas and the distance d between electrodes

positive semi-period but also in the negative semi-period of the supply voltage 4

Through the phase difference circuit C_1 - R_2 there is set the start angle of triac V_6

$$tg\phi = \omega C_1 \bullet R_1 \quad (4)$$

where ω - AC pulsation.

The voltage applied on the serial oscillating circuit L_p - C_3 being significantly deformed, will contain a high number of harmonics.

The oscillated circuit L_p - C_3 will enter the resonance on one of the harmonics of which the frequency is.

$$f_0 \approx \frac{1}{2\pi\sqrt{L_p \bullet C_3}} \quad (5)$$

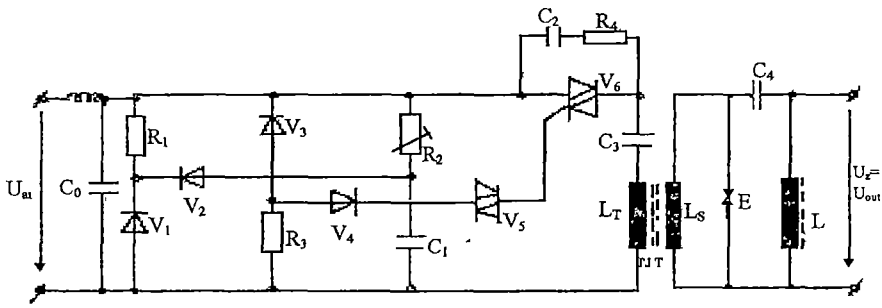

Fig.3. Basic diagram of D A Ar [3]

where

L_p = inductance of the primary winding of the high frequency transformer

C_3 = capacity of the series capacitor

The number of pulses during a semiperiod of the supply voltage is

$$N_1 = \frac{10 \bullet \theta}{\pi} \bullet f_0 \quad \text{or} \quad N_1 = \frac{\tau}{T_0} \quad (6)$$

where

$\theta + \pi - \phi$ - is the conduction angle of the triac

$f_0 = \frac{1}{T_0}$ - is the oscillation frequency of the serial oscillating circuit L_p-C_3.

The pulse amplitude of the oscillating circuit are increased by a factor of K through the high voltage transformer (T I T) shown in Fig. 3:

$$K = \frac{n_s}{n_p} \quad (7)$$

where

n_s = number of turns in the secondary winding

N_p = number of turns in the primary winding

$$10 R_1 \bullet C_1 = R_2 C_1$$
$$10 R_3 \bullet C_1 = R_2 C_1 \quad (8)$$

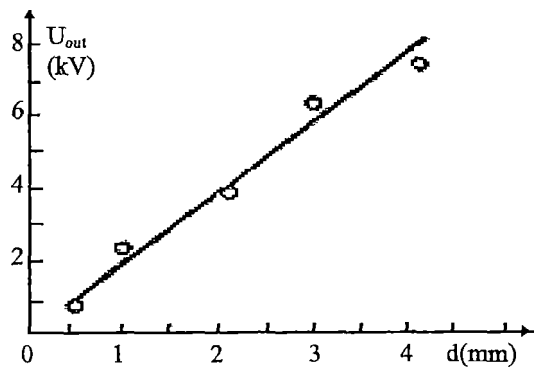

Fig. 4. D A Ar output voltage variation as a function of the distance d_E between the eclators.

Elimination of the electric hysteresis phenomenon is obtained by meeting the conditions [4]

For meeting the condition (8) the opening pulses of the triac V_6 are given the same moment on the sine curve of the supply voltage The circuit R_4-C_2 protects the triac V_6 at overvoltage

The voltage supplied by TIT is applied to the scintillation oscillating circuit The scintillation oscillating circuit is cons-tituted by the spark gaps E, the capacitor C_4 and the coil L [4] The coil L has a protective role for the WIG supply source (Fig 1) The oscillation frequency of the scintillation oscillating circuit is

$$f = \frac{1}{2\pi} \bullet \frac{1}{\sqrt{L \bullet C_4}} \quad (9)$$

and the oscillator output signal power is

$$P = f_0 \bullet C_4 \bullet U_{out}^2 \quad (10)$$

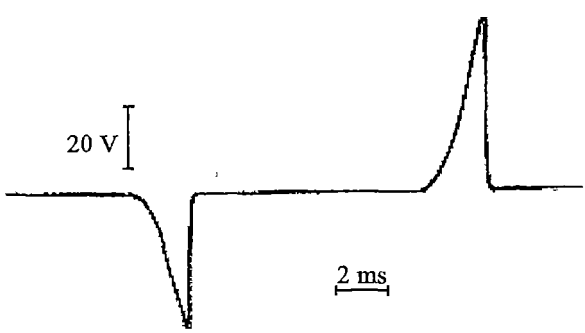

Fig. 5. Time variation of the control voltage on the gate of the triac [6]

Experimental results and conclusions The voltage U_{out} at the output of the starting device, which had been measured using the sphere eclators method [5] The sphere eclators measure the maximal voltage pulse value The measurements have been performed with spark gaps with

diameters of 20 mm and also a radioactive cell ^{85}Kr

It has been observed the modification of the output voltage U_{out} as a function of the distance d_E between the spark gaps E Experimental results are synthesized in Fig 4 The linear dependence of the voltage U_{out} of the distance d_E allows the control of starting voltage of the WIG arc The conduction time, corresponding to the angle of the triac V_6 in a semiperiod of the alternating supply voltage is of 2 ms (Fig 5)

The frequency of electrical oscillations in the circuit C_3 - L_p is F_0 = 1 MHz (Fig 6) As a consequence the number of high frequency pulses (Fig 7) over a semiperiod of the voltage calculated by expression (6) is $N_1 = 2$ The frequency of signal (Fig. 7) obtained at the output O A Ar is f = 5 MHz

The study of the connecting mode of the WIG source and that of the D A Ar. to the electricity supply net has been done using the connection given in Fig 8 S.WIG - WIG source , D A Ar. - arc starting device, L, C - protecting elements for the WIG source, C_1, C_2, C_3 - Capacitive voltage divider

1	2	3	4
R	N	R	S
R	N	S	R
R	N	S	T
R	N	T	S
R	N	R	T
R	N	T	R

Table 1

The connecting mode of the WIG source at the three-phase supply net (R, S, T) and also the connecting mode of D A.Ar at the single phase electricity supply net is according to Table 1

Electricity supply output terminals of table 1 correspond to those in fig 8 (1 - 2 = supply D A Ar , 3 - 4 = WIG source supply)

They have been displayed on an oscilloscope and photographed the WIG source output voltage and pulses obtained at the output of the electric arc starting device

If U_{RN} is the D A Ar supply voltage and U_{RS}, U_{SR}, U_{ST}, U_{TS}, U_{TR} and U_{RT} the WIG source supply voltages, then the high frequency high voltage pulses are phase

Fig. 6 Electrical oscillations in the primary winding of the high voltage transformer TIT

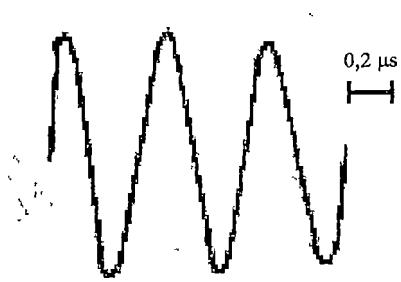

Fig. 7. Form of efficient signal at D A Ar output (f=5 MHz) [6]

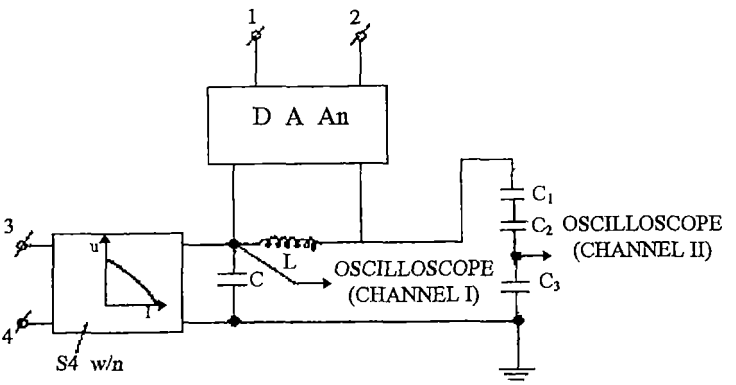

Fig. 8. Principal electrical diagram of the connection used for study of WIG arc starting in AC

displaced from the current through the arc WIG, as shown in Fig 9 In Fig 9 there has been assumed that, the current through the arc WIG in, in a prime approximation, in phase with the voltage at the terminals of the WIG source There has been found by experiment that approximation does not affect the results of the measurements

On the experimental data it yields that high frequency high voltage are applied at the moment of passing through zero of the discharge current only in the cases corresponding to Fig 9 is according to Fig. 9-f

In the oscillating circuit C_4-L the capacitor C_4 has values of hundreds of picofarads The

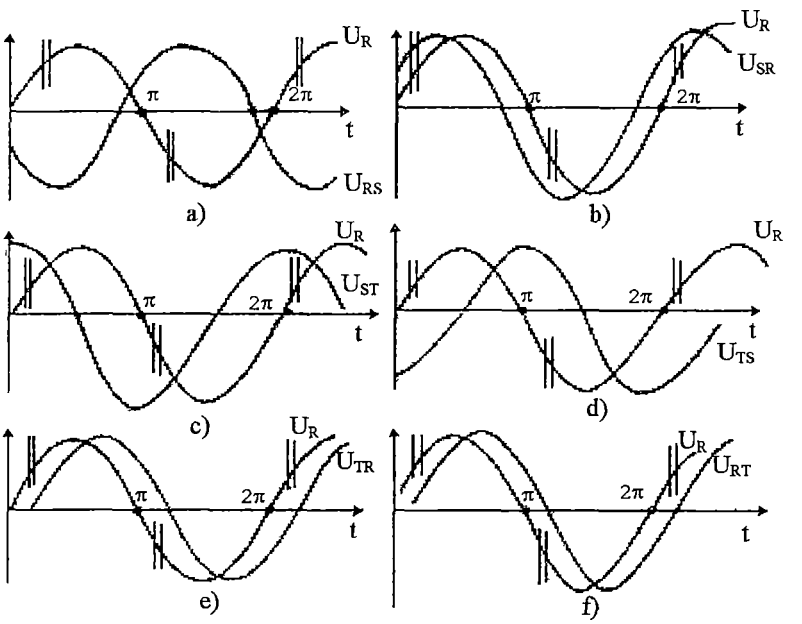

Fig 9. High frequency high voltage pulses (vertical lines of the semisinusoid U_R) related to the no load voltage U_{RS}, U_{SR}, U_{ST}, U_{TS}, U_{TR} and U_{RT} of the WIG source

power P in pulse of the high frequency high voltage signal for the value rank of the output voltage has a maximal value of 32 W (fig 10)

By connecting D A Ar to the supply voltage (as in fig. 9-e or as in fig.9-f) and selecting a power P for the high frequency voltage, by adjusting the distance d_E, due to concrete technological requirements , the WIG arc is easily started and burns stable

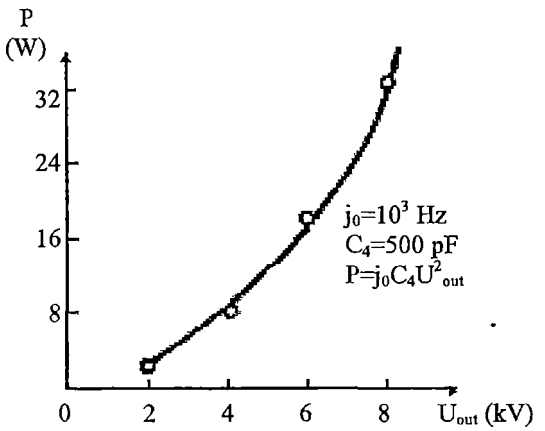

Fig. 10 Variation of the power P in pulse of the high frequency high voltage signal as a function of the output voltage U_{out} of D A Ar

Acknowledgements. The paper has been prepared with financial assistance of TES SA Timisoara, Avenue Mihai Viteazul 30b, according to the cooperation agreement No 130/04 05 1992

I also wish to express may gratitude to Prof Dr Titihazan Viorel of the Technical University in Timisoara for high voltage measurements

REFERENCES

1 B Tareev , *Physics of dielectric materials*, Mir Publishers Moskow, 1975
2 J F Lancaster, *The Physics of Welding*, Program Press, Oxford 1984
3 I Bica, G Mucsy - Patent RO No 83348/1983
4 H Lilem , *Thyristor et triacs*, Ed Rodio, Paris 1971
5 Fl Tanasescu, *High voltage electric measurements*, Vol III, Ed Tehnică, Bucharest 1971
6 I Bica, Annals of the University in Timisoara, Series Physical Sciences 27 (1989), 51 - 54










STUDIA UNIVERSITATIS "BABES-BOLYAI", PHYSICA, XL, 2, 1995

DOUBLE-EXCITATION OF HELIUM BY FAST CHARGED PARTICLES

L. NAGY[1], D BODEA[1]

ABSTRACT. The double-excitation cross sections of the helium to the *2s2p* state by proton and antiproton (electron) impact have been evaluated. We have used a perturbation expansion in the projectile-electron interaction, and have included in our calculations the first-order (shake) and the time-ordered second-order (TS2) terms Electron-electron interactions have been approximated with a screening potential Our results are in good agreement with the experimental data and the close-coupling calculations [8]

Introduction. Two-electron transitions in fast collisions with charged particles have been studied by various groups in the past several years both theoretically [1-11] and experimentally [12-15] These studies yield information on the dynamics of the electron-electron interaction since two-electron transitions are dominated by the electron-electron interaction in very fast collisions At moderately fast velocities, a two-electron transition may be described [1] in terms of a coherent sum of first and second order terms in a Born expansion in the interaction strength (i e projectile charge), Z

The square of such a first plus second order amplitude yields a Z^3 contribution to physical observables such as transition probabilities and cross sections Since the uncorrelated contribution to the second order amplitude does not contribute to the Z^3 term, such observable Z^3 effects may also be classified as a dynamic correlation effects

The most investigated atom for two-electron processes was the simplest two-electron system, the helium atom Calculations were made for the double ionization [3,4], ionization excitation [11] and for double excitation [2,8] Fritsch and Lin [8] have made coupled-channel calculations for the double excitation of the helium by differently charged projectiles to four different final states Their results are in fair agreement with the experimental data Straton and McGuire [2] have made a perturbation expansion in the projectile-electron interaction. The second-order amplitude includes a time-ordering term, leading to interference between the first and second-order amplitude However, their results does not agree with other calculations and the experimental data

We have developed a similar method (using perturbation expansion) for the calculation of

[1] *Babeş-Bolyai University, Department of Atomic and Nuclear Physics, 3400 Cluj-Napoca, Romania*

We have developed a similar method (using perturbation expansion) for the calculation of the cross sections for two-electron processes [10,11]. The calculation of the time-ordered second-order amplitude is made directly We have published our results for the ionization-excitation [11] of the helium

In the present paper we report our calculations for the double excitation of the helium by fast charged particles impact. We have investigated collisions ranging from asymptotically large velocities, where double to single excitation cross section ratios tend to a constant to moderately high velocities where Z^3 term occur

Theory. For the calculation of the double-excitation cross section of the helium by charged particles impact we treat the projectile as a classical particle with a straight line trajectory, $\mathbf{R}(t) = \mathbf{b} + \mathbf{v}t$ and treat the electronic evolution separately [16]. The interaction of the projectile with the two electrons is considered as a perturbation

$$V(t) = V_1(t) + V_2(t) \tag{1}$$

The wave function of the two-electron system is approximated as a product of one-electron wave

$$H^0_{exact} = -\frac{1}{2}(\Delta_1^2 + \Delta_2^2) - \frac{Z_T}{r_1} - \frac{Z_T}{r_2} + \frac{1}{r_{12}} \tag{2}$$

functions Thus, instead of the exact unperturbed Hamiltonian of the two electrons, namely

$$H^0 = -\frac{1}{2}\Delta_1^2 - \frac{Z_T}{r_1} + V_2(r_1) - \frac{1}{2}\Delta_2^2 - \frac{Z_T}{r_2} + V_1(r_2) \tag{3}$$

the states are approximately described by a sum of one-electron Hartree-Fock Hamiltonians

Here $V_2(r_1)$ is the screening potential for the electron 1 created by the electron 2 and $v_1(r_2)$ is the screening potential for the electron 2 created by the electron 1 The screening potentials are different for the initial and for the final states.

Because in the initial state we have two electrons in the same (1s) state, the effect of electron symmetry may be ignored In this paper we have investigated the excitation to the *2s2p* state, which is described as a product of a *2s* and a *2p* wave functions

The first-order amplitude, with a single interaction with the projectile is.

$$\begin{aligned} a^{(1)} = -i < f_2^{s'} | i_2 > \int_{-\infty}^{+\infty} dt\, e^{i(E_f - E_0)t} < f_2^{p} | V_1(t) | i_1 > \\ -i < f_1^{p'} | i_1 > \int_{-\infty}^{+\infty} dt\, e^{i(E_f - E_0)t} < f_2^{s} | V_2(t) | i_2 > \end{aligned} \tag{4}$$

where for the initial state, i, we consider a wave function consisting of a *1s* orbital only, neglecting

double excited state while E_0 is the ground state of the helium

Because the initial and final states has different Hamiltonians, the overlap integrals in (4) can be nonzero The first-order term in the amplitude can be regarded as a shake-up contribution.

In our second-order term the transition is caused by two consecutive projectile-electron interactions. We keep track of the time-ordering· the energy transfer to the individual electron depends on the order of the interactions [7]. Theoretically there are an infinity of intermediate states, but we keep only two. electron 1 in the final and electron 2 in the initial state, and vice versa.

Let ΔE_s and ΔE_p denote the excitation energies for the two possible simple-excited states (in this case one electron is in the ground state, so the screening potential is $v_{ground}(r)$) The energy transfer to the second excited electron is $\Delta E_s'$ or $\Delta E_p'$ which are different from ΔE_s respectively ΔE_p The relations between the two energie transfers are

$$E_f - E_0 = \Delta E_s + \Delta E_p', \text{ or } E_f - E_0 = \Delta E_p + \Delta E_s'$$

So we have

$$\Delta E_p' = E_f - E_0 - \Delta E_s \text{ and } \Delta E_s' = E_f - E_0 - \Delta E_p$$

The second-order amplitude may now be written as follows

$$\begin{aligned} a^{(2)} = & -\int_{-\infty}^{+\infty} dt\, e^{i(E_f - E_0 - \Delta E_s)t} < f_2^{p'} | V_2(t) |_{12'} > \\ & x \int_{-\infty}^{t} d't\, e^{i(\Delta E_s)t'} < f_1^{s} | V_1(t') |_{1_1} > \\ & -\int_{-\infty}^{+\infty} dt\, e^{i(E_f - E_0 - \Delta E_p)t} < f_1^{s'} | V_1(t) |_{1_{1'}} > \\ & x \int_{-\infty}^{t} d't\, e^{i(\Delta E_p)t'} < f_2^{p} | V_2(t') |_{12} > \end{aligned} \tag{5}$$

where the unprimed wave functions are calculated in a screening potential created by the other electron in the ground state, while the primed wave functions are calculated with the other electron in the final state

For a given state the first-order amplitude is purely imaginary The second-order amplitude, because of the time-ordering term, is complex. Interference occurs between first-order and second-order amplitudes, so we obtain different cross sections for positively and negatively charged projectiles.

The cross section can be calculated by integrating the square of the amplitude over the impact parameters,

$$\sigma = 2\int |a^{(1)} + a^{(2)}|^2 d^2b$$

where the factor 2 stands for the two possible equivalent final states electron 1 excited in the 2s

where the factor 2 stands for the two possible equivalent final states electron 1 excited in the 2s state and 2 excited in the 2p state, or 2 excited in the 2s state and 1 excited in the 2p state

Results and discussion. We have made calculations for the excitation of the *2s2p* state of the helium atom by positively and negatively charged particle impact. The initial state is described by Hartree-Fock wave functions [17] and the final state by a product of two hydrogenic wave functions In the intermediate state the inner electron is taken in a hydrogenic state, the excited one is screened [17]. In the calculation of the amplitudes and cross sections, integrals over angles were performed analytically, while the radial intergrals in the matrix element, the integrals over time and the impact parameter were performed numerically

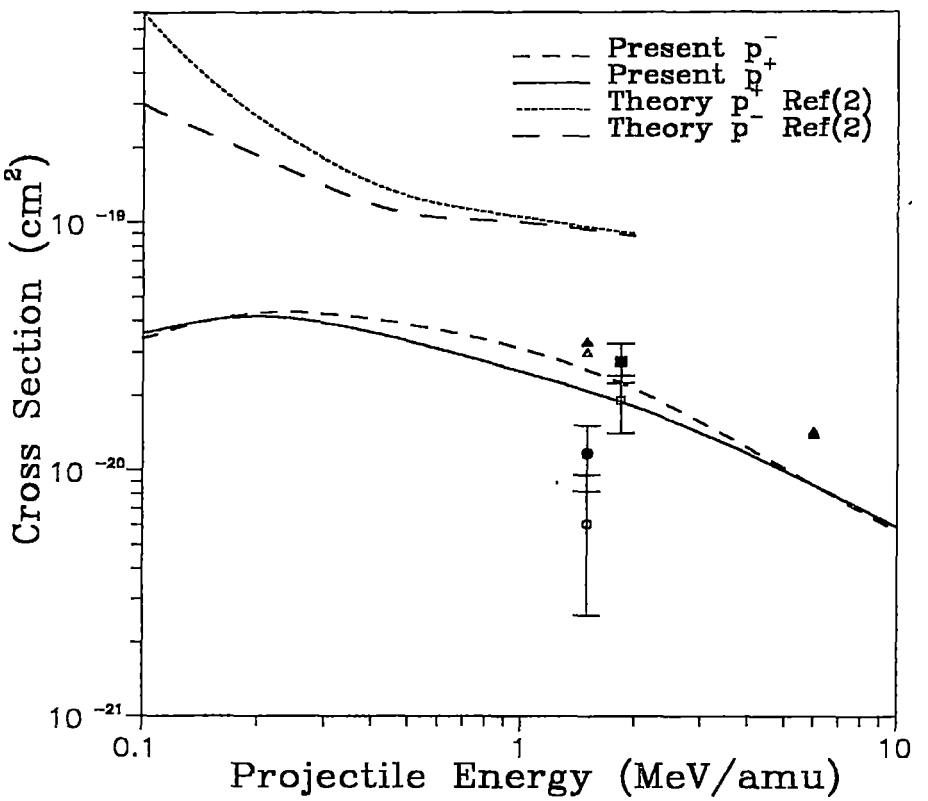

Fig.1. Double excitation cross section of the helium by charged particle impact as a function of projectile energy Circles represents experimental data of Giese et al [14], squares are the data of Pedersen and Hvelplund [13] and triangles the theoretical results of Fritsch and Lin [8] Open symbols stand for proton impact, full symbols for equivelocity electron impact

Figure 1 shows our calculated double-excitation cross section as a function of the projectile

Giese et al [14], and the theoretical calculations of Fritsch and Lin [8] and McGuire and Straton [2] The data are for protons of given energy and for the same velocity electrons The experimental data of Pederson and Hvelplund [13] represent a sum of the $2s2p(^1P)$ and the $2p^2(^1D)$ cross sections, other data are for the excitation of the $2s2p(^1P)$ alone In the energy range between 200 keV and 5 MeV our cross sections for negatively charged particle (antiprotons or same velocity electrons) are higher than the cross sections obtained with proton projectiles, in agreement with the experimental data and the coupled-channel calculations of Fritsch and Lin [8] The absolute value of our results are between the experimental data of Giese et al [14] and the theoretical results of Fritsch and Lin [8] On figure 2 is represented the relative importance of the two considered mechanisms, shake-up (first-order term) and TS2 (second-order term) As it was expected, the second-order cross section falls down more rapidly with the energy than the first-order one, and is negligible at high projectile energies. At 100 keV the two mechanisms have the same importance

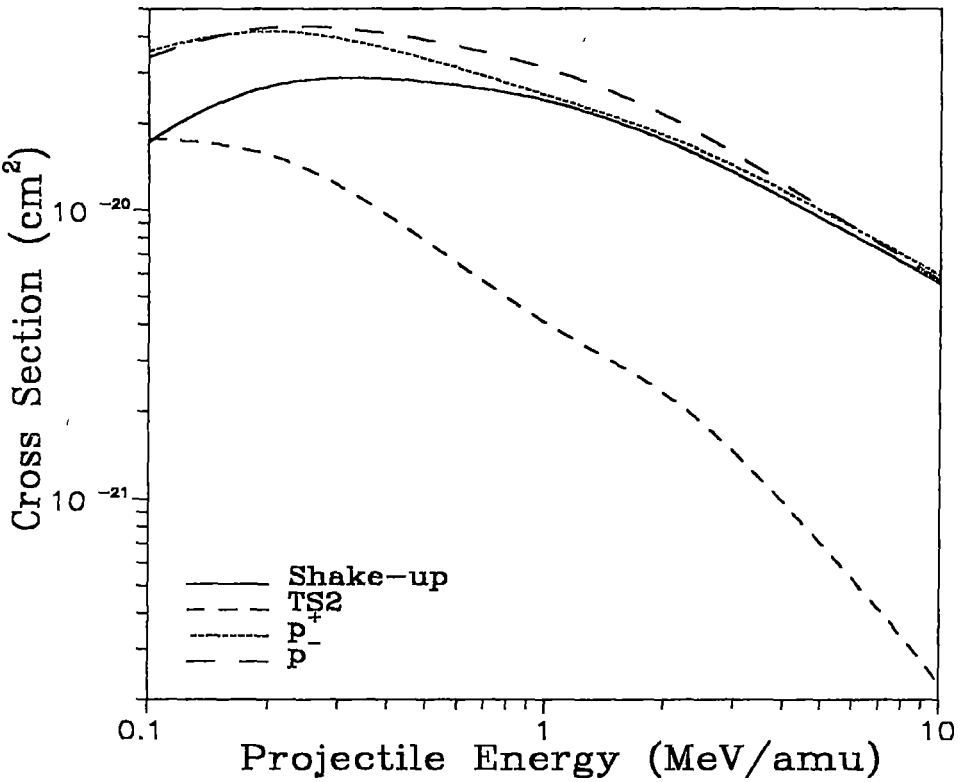

Fig 2. The contributions of the first and second-order amplitudes to the double excitation cross sections to the $2s2p$ state of the helium by proton and antiproton impact as a function of the projectile energy

We can conclude that our calculated cross sections for the double excitation of the helium to the *2s2p* state are in good agreement with the available experimental data, in spite of the fact that for the description of the two-electron states we have used simple product wave-functions We obtain higher cross sections for negatively charged projectiles than for positive ones in agreement with the experiments and the coupled-channel calculations of Fritsch and Lin [8] We have get this dependence of the cross section on the sign of the charge of the projectile due to the interference of the shake-up (first-order) and the time-ordered TS2 (second order) amplitudes Further studies should reveal the importance of the (here neglected) electron-electron correlations in the double excitation process.

REFERENCES

1 J H McGuire, Adv At Mol. Opt Phys **29**, 217 (1991)
2 J H McGuire and J C Straton, Phys Rev A **43**, 5184 (1991)
3 J F Reading and A L Ford, J. Phys. B **20**, 3747 (1987)
4 A L Ford and J F Reading, J Phys B **27**, 4215 (1994).
5 R E Olson, Phys Rev A **36**, 1519 (1987)
6 L Vegh, Phys Rev A **37**, 992 (1988)
7 L Vegh, B Sulik and N Stolterfoht, Phys Rev A **51**, 3129 (1994)
8 W Fritsch and C D Lin, Phys Rev A **41**, 4776 (1990)
9 F Martin and A Salin, J Phys B **28**, 639 (1995)
10 L Nagy and L Vegh, Phys. Rev A **50**, 3984 (1994)
11 L Nagy, J Wang, J C Straton and J H McGuire, Phys Rev A **52**, R902, (1995)
12 L H Andersen, P Hvelplund, H Knudsen, S P Moller, A H Sorensen, K Elsner, K G Rensfeld and E Uggerhoj, Phys Rev , A **36**, 3612 (1987).
13 J O P Pedersen and P Hvelplund, Phys Rev Lett **62**, 2373 (1989)
14 J P Giese, M. Schulz, J K Swensen, H Schoene, M Benhennu, S L Varghese, C R Vane, P F Dittner, S M Shafroth and S Datz, Phys Rev A **42**, 1231 (1990)
15 S Fulling, R Bruch, E. A Rauscher, P A Neil, E Trabert, P H Heckmann and J H McGuire, Phys Rev Lett **68**, 3152 (1992)
16 JH McGuire and O L Weaver, Phys Rev A **34**, 2473 (1986)
17 E Clementi and E Roetti, At Data Nucl Data Tables **14**, 177 (1974)
18 P M Morse, L A Young and E S Haurwitz, Phys Rev **48**, 948 (1935)

STUDIA UNIVERSITATIS "BABES-BOLYAI", PHYSICA, XL, 2, 1995

MNR OBSERVATION OF THE RESIDUAL DIPOLAR INTERACTION IN MOLTEN POLYBUTADIENE

M Todica[1]

ABSTRACT. The superposition property of the relaxation curves of the transversal magnetization and the specific properties of the pseudo-solid echoes, were used to demonstrate the existence of the residual dipolar interaction between the protons attached to the polymeric chain

Introduction. It is well known that the relaxation function of the transversal magnetization is a rich source of information concerning the local and long range properties of polymeric chain Generally the mathematically expression of this function is not simple, because the relaxation of the transversal magnetization is a complex process governed by the interaction between the protons attached to the polymeric chain.

In many cases it is very difficult to find the exact form of this function, but some conclusions about the relaxation process can be disclosed by analyzing the properties of relaxation curves For instance, the superposition property of the relaxation curves, in association with the pseudo-solid behavior were utilized to demonstrate the existence of the residual dipolar interaction, [1]

In this work we are interested to analyze the properties of the relaxation curves, in order to characterize the relaxation mechanism

Experimental. We studied two polybutadiene samples, PB1507 and PB1009, kindly supplied by the Manufacture Michelin, France The microstructure and the molecular mass of two samples were M_n=190000 g/mole, 40% in vinyl conformation, 36% in trans conformation, 24% in cis conformation and T_g=202K for PB1507, M_n=70000 g/mole, 8% in vinyl conformation, 54% in trans conformation, 38% in cis conformation and T_g=175K, for PB1009

All the measurements were performed using a CXP Bruker spectrometer working at 45 MHz, in the temperature range of 250 K to, 344 K The relaxation of the transversal magnetization was observed using the Carr-Purcell sequence, [2], and the pseudo-solid echoes

[1] Faculty of Physics, "Babeș-Bolyai" University, 3400 Cluj-Napoca

were observed using the following pulse sequence: $[p/2]_y$ - $[t$- $(p)_y$ - $t]_n$ - $[p/2]_x$ - $[t$ - $(p)_y$ - $t]_k$ - echo, [3]

Results and discussion. Some typical relaxation curves of the transversal magnetization, for many temperatures, are shown in Fig 1

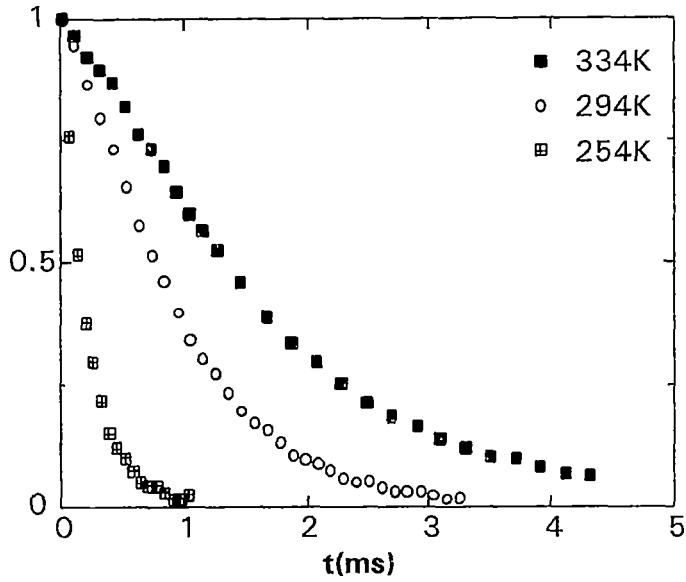

Fig 1 The relaxation curves of the transversal magnetization observed for the PB1507 sample for some temperatures

The relaxation curve in not a simple exponential function We observed a radical change of the shape of these curves in the vicinity of one characteristic temperature for each sample, which was called *"reference temperature"*, T_{ref} The values of these temperatures are T_{1ef}=294 K for PB1507 and T_{ref}=264 K for PB1009. These temperatures were higher than the glass transition temperature, of about 90 K, so that T_{ref}-T_g=const

For temperatures higher than T_{ref}, the relaxation curves obeys to a superposition property For instance we can consider $f_1(T_1,t)$ the relaxation function corresponding to the temperature T_1 and $f_2(T_2,t)$ the relaxation at T_2, where $T_2 > T_1 > T_{ref}$ Apparently $f_1(T_1,t)$ and $f_2(T_2,t)$ are two different functions In our case we can superpose these curves by dividing the time scale with a constant factor S, named *"superposition factor"*, so that $f_1(T_1,t)=f_2(T_2,t/S)$, Fig 2

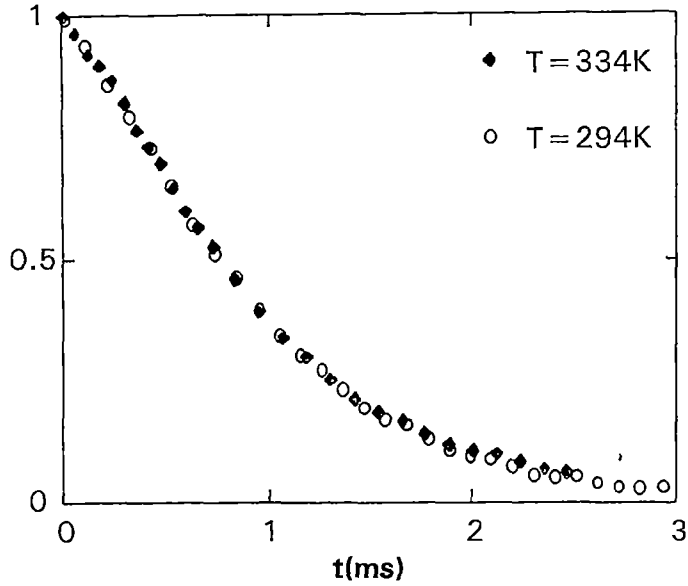

Fig. 2 The superposition of the relaxation curves observed for the PB1507 sample above T_{ref}.

The temperature dependence of the superposition factor is shown in Fig 3 Then we can affirm that these functions have the same mathematically expression That means that the relaxation of the transversal magnetization, for temperatures higher than T_{ref}, is governed by the same mechanism.

When the temperature is lower than T_{ref}, the superposition property is not respected and the relaxation curves have different mathematically forms We can conclude that the mathematically expression of the relaxation function change in the vicinity of T_{ref} and thus the relaxation mechanisms are different for temperatures uppers and lowers than T_{ref} T_{ref} is then an important parameter which denote changes in the relaxation properties

The dominant mechanism which govern the relaxation of the transversal magnetization is the dipolar interaction between the protons attached to one polymeric chain, but this interaction is affected by two main factors the temporary junctions between two different chains and the dynamics of skeletal bonds. The temporary junctions induces an orientation order of the conformational fluctuations, and thus an anisotropy of the monomer rotations As a results, the dipolar interaction is not averaged to zero. This residual dipolar interaction determine the pseudo-solid behavior of the relaxation function, [4] In this case the pseudo-solid echoes have specific properties

- the intersection of two echoes generated at instants $t=t_1$ and $t=t_2$, must occur at $t=t_1+t_2$ where $t_1=2tn_1$ and $t_2=2tn_2$
- the slopes of the relaxation function and of the echoes function must be symmetric at the origin of the echo, [3]

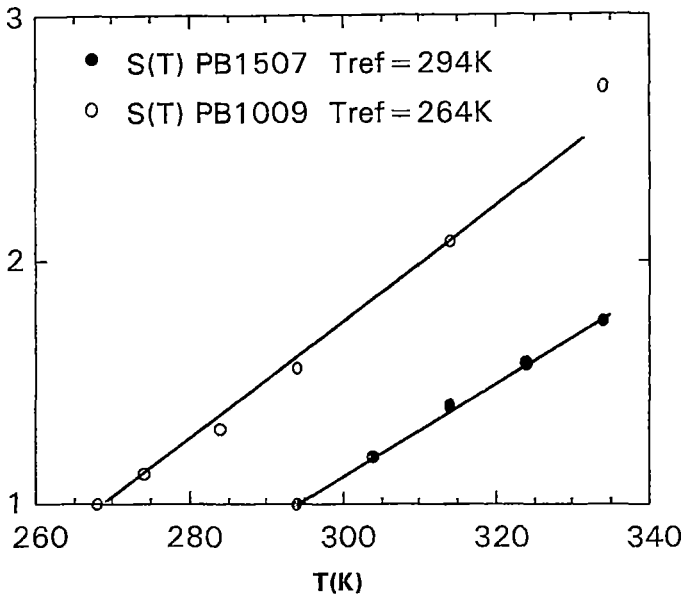

Fig 3 The temperature dependence of the superposition parameter observed for the PB1507 and PB1009 samples

When $T > T_{REF}$, we observe the pseudo-solid echoes with specific properties for both polymers, PB1507 and PB1009, Fig 4. The relaxation of the transversal magnetization is governed in this case by the residual dipolar interaction

When the temperature is lower than T_{ref}, the pseudo-solid echoes do not respect the specific properties This situation is illustrated in Fig 5 We observe again that the T_{ref} is the macroscopic parameter which mark changes of the properties of the pseudo-solid echoes

We can explain this behavior if we suppose that the relaxation function can be expressed as a product of two other functions $M_X(t)=M_X^e(t)*F_e(t)$ The function $M_X^e(t)$ is associated with the asymmetry of monomeric units rotations and distort the pseudo-solid echoes $F_e(t)$ determine the pseudo-solid behavior of the relaxation function and reflects the dynamics of the skeletal bonds, [5] The function $F_e(t)$ depends upon the spectral density of

thermal energy $J(w_0t_c)$, where w_0 is the Larmor frequency and t_c is the correlation time of the molecular motion

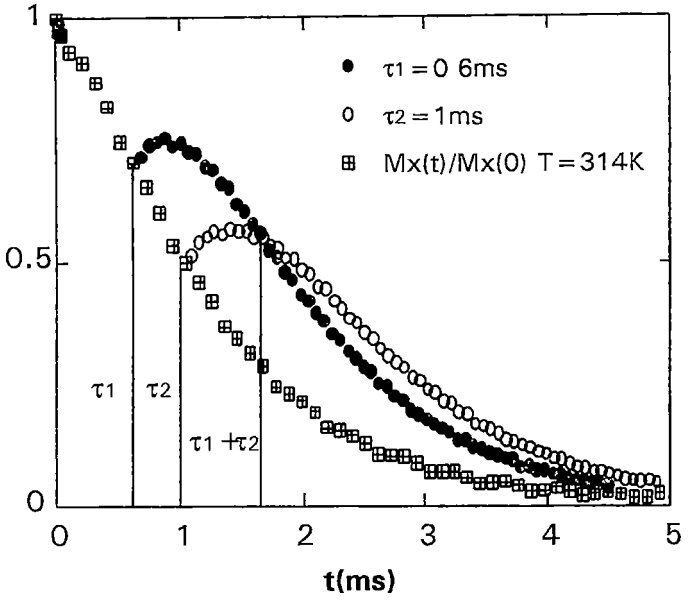

Fig. 4 The pseudo-solid echoes, with specific properties, observed for the PB1507 sample above T_{ref}, (T=314K)

For lower temperatures that T_{ref}, the correlation time t_c is very long and the function $F_e(t)$ has the major contribution on the total relaxation function $M_X(t)$ For this reason the pseudo-solid echoes do not respect theirs specific properties and the relaxation function do not obey to the superposition property When the temperature increase, the correlation time diminish and the function $F_e(t)$ is very long, practically constant in comparison with the function $M_X^e(t)$. In this case the function $M_X^e(t)$ has the major contribution to the total relaxation function $M_X(t)$. The relaxation curves obey to the superposition property and the pseudo-solid echoes have specific properties, [6]. The relaxation of the transversal magnetization is governed by the residual dipolar interaction when $T > T_{ref}$ We associate the change in the dominance of one of the two functions $F_e(t)$, or $M_X^e(t)$, with the reference temperature Also the superposition of the relaxation functions is observed in correlation with this temperature. We can associate the two observations to established the dominance of the residual dipolar interaction For this, it is not necessary to observe the pseudo-solid echoes for each temperature, it is sufficiently to test the superposition property of the relaxation

for each temperature, it is sufficiently to test the superposition property of the relaxation functions and then it is necessary to observe the pseudo-solid echoes for some temperatures in the superposition domain If the pseudo-solid echoes have the specific properties, then the relaxation is governed by the residual dipolar interaction In the contrary case, the relaxation is affected by the dynamics of skeletal bonds

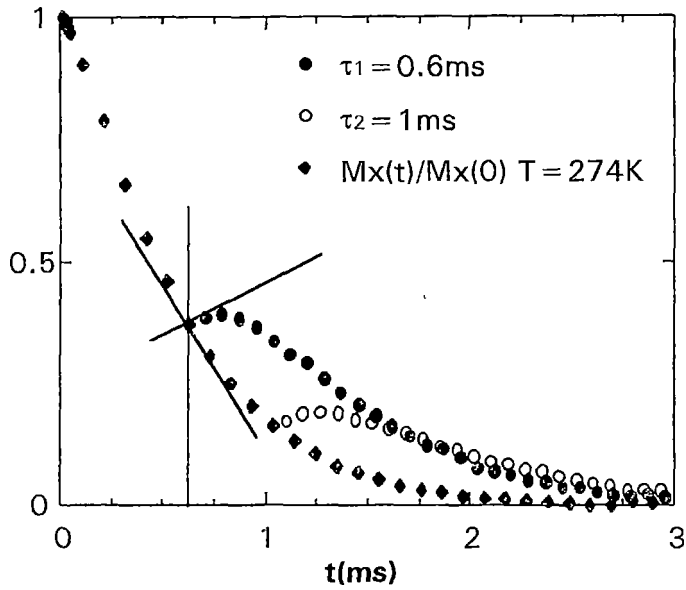

Fig 5 The pseudo-solid echoes observed for the PB1507 sample,
for temperatures lower than T_{ref}, (T=275K)
The slopes of the echoes and the relaxation curves are not symmetric

Superposition of the relaxation functions associated with the observation of the pseudo-solid echoes, is a simple way to characterize the relaxation mechanism

We analyzed also the superposition of the relaxation functions and the properties of the pseudo-solid echoes for the PB1009 sample. We observed the same behavior as in the case of the PB1507 sample. The reference temperature is T_{ref}=264 K, so that T_{ref}-T_g=91 K For $T > T_{ref}$, the relaxation functions obey the superposition property and the pseudo-solid echoes have specific properties, Fig 6. This properties were not observed for temperatures lower than T_{1ef}

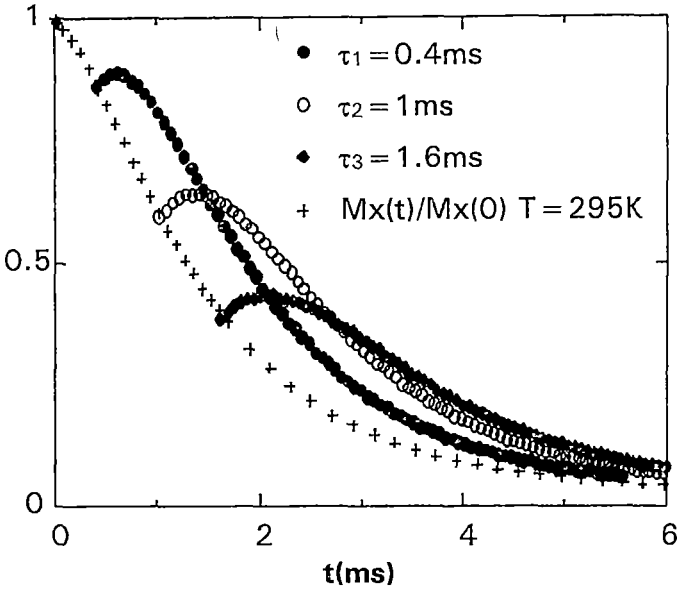

Fig 6 The pseudo-solid echoes with specific properties, observed for the PB1009 sample, above T_{ref}, (T=295K)

The samples PB1009 and PB1507 have different microstructures and different molecular masses, but the general behavior of the relaxation functions is the same in both cases We can conclude that the analysis of the relaxation functions previously described, is a general way to observe the residual dipolar interaction

Conclusion. The relaxation curves of the transversal magnetization observed in molten polybutadiene, obey to a superposition property This property is observed for temperatures higher than a characteristic temperature for each polymer, called reference temperature, T_{ref} The superposition property indicate that different relaxation curves can be described by the same mathematical expression. In this case the relaxation of the transversal magnetization is governed by the same mechanism

The existence of the pseudo-solid echoes with specific properties, indicate that the dominant mechanism of the relaxation is the residual dipolar interaction between the protons of one polymeric chain This echoes were observed for temperatures higher than T_{ref} For temperatures lowers than T_{ref}, the superposition and the specific properties of pseudo-solid

echoes were not observe and the relaxation of the transversal magnetization is affected by the dynamics of skeletal bonds

The observation of the superposition of the relaxation curves and the observation of the pseudo-solid echoes with specific properties, is a simple way to demonstrate the existence of the residual dipolar interaction

REFERENCES

1 J P Cohen-Addad, A Labouriau, J Chem Phys, 93, 4,15, 1990

2 H Y Carr, E R Purcell, Phys Rev, 94, 630, 1954

3 J P Cohen-Addad, C Schmit, Polymer, 29, 883, 1988

4 J P Cohen-Addad, *NMR and Fractal Properties of Polymers Liquids and Gels*, Pergamon Press, London, 1992

5 J P Cohen-Addad, E. Soyez, A Viallat and J P Queslel, Macromol, 4, 25, 1992

6 M Todica, These, Univ Joseph Fourier, Grenoble, 1994

STUDIA UNIVERSITATIS "BABES-BOLYAI", PHYSICA, XL, 2, 1995

6 MeV ELECTRON BEAM CALIBRATION FOR GE SATURN 41 ELECTRON LINEAR ACCELERATOR

Gy. Hegyi[1], Maria Gherasim[2], Alexandra Lup[2], V. Simon[2]

ABSTRACT Calibration data for 6 MeV electron beam of GE Saturn 41 electron linear accelerator are reported Absorbed radiation doses in a PMMA phantom for radiation fields ranging from 4x4 cm up to 30x30 cm, obtained by applying additional tungsten plate applicators at distances of 9 5 cm in X direction and 13 cm in Y direction above the irradiated surface in the plane of isocenter as well as output factors for therapeutic fields are investigated The results indicate that the absorbed doses in a certain irradiated volume are limited by the irradiation field dimensions It is also evidenced an asymmetry of the output factors for irradiated fields of same surface but of different dimensions

Introduction The use of electron beams in radiotherapy requires to establish the proper method in order to obtain a therapeutical beam with very exactly known parameters (field dimensions, given dose etc) The desired parameters are practically obtained by means of electron beam calibration. The beam calibration method consists of two stages (1) dose measurement in a certain reference point in an irradiated phantom and (2) the relative dose determination in the reference point in other conditions than the reference ones For the second stage it is necessary to determine the output factor and the depth dose absorption curve On the other hand the electron beam depends on type of linear accelerator, on transport phenomena inside the beam, on beam profile flattening system as well as on collimating system The results regarding the calibration of the locally unexplored 6 MeV electron beam, interesting for certain treatment techniques, provided by a GE Saturn 41 linear accelerator, are presented in this paper

Experimental. The results presented in this study were obtained using a General Electric (GE) Saturn 41 linear accelerator providing electron beams with energies ranging from 6 to 15 MeV The electron beam generated by the acceleration system is flattened by

[1] Ion Chiricuță Institute of Oncology , Cluj-Napoca, Romania
[2] Faculty of Physics, Babes-Bolyai University, Cluj-Napoca, Romania

means of a two scattering foils system The first foil has the scattering role while the second one has the beam profile flattening role for the whole irradiation field [1, 4] Therefore in the output of the accelerator head a divergent and uniform electron beam is obtained The expansion of the irradiation field was limited by the field collimators (40x40 cm) disposed in the accelerator head and by the additional tungsten applicators (30x30 cm) disposed outside the linear accelerator at 9.5 cm in X direction and 13 cm in Y direction above the irradiated surface in the plane of isocenter The set up of the PMMA phantom was controlled by a laser beam system The source surface distance (SSD) was 100 cm The 6 MeV electron beam calibration was accomplished using the absorbed dose method [2] in a reference point in the PMMA phantom, at a depth of 1 1 cm The absorbed dose was measured first in the reference field and then it was measured for all accessible fields of dimensions ranging between 4 and 30 cm along OX and OY directions The reference field size was selected as 10x10 cm

The absorbed doses measurements were carried out by means of a UNIDOS dosimeter with PTW 0 3 cm^3 Normal M 233332 type ionisation chamber [2] Pressure and temperature corrections were operated

Results and discussion. The air as integral part of the experimental structure used in our calibration experiments scatters nearly the right amount of electrons back into the beam The interactions of the electron beam with the air in the space between the irradiation head and the irradiated surface and with the field limitation system determine the scattering of a part of electrons and consequently the alteration of their energy [3, 4] These scattering processes determine a contamination of the primary radiation beam with low energy electrons The average energy of the scattered electrons going back into the beam represents about 40% of the average energy corresponding to the electrons from the primary radiation [4] . The contribution of the scattered low energy electrons to the primary electron beam leads to hot spots along the field edges Consequently the irradiated field surface can increase much above the useful field surface The scattered electrons represent a contamination for the primary election beam One of the effects of this contamination consists of the irradiation field broadening, much above the desired surface In order to avoid the undesired

contamination of the primary electron beam with low energy electrons outside the desired irradiation field, additional external field limiting applicators are used to introduce a minimal electron scattering outside the electron beam The field limiting applicators may be plates or cylinders The used plate applicators introduce an additional flattening that can vary considerable with the distance from the end of the applicators to the irradiated surface because of a fraction of the scattered electrons. The electron beam must be collimated close to the irradiated surface and the beam cross section should be significantly wider than the geometric beam in order to obtain a balance at the edge of the beam between electrons scattered into and out of the beam

In the treatment with electron beams the specification of the therapeutical range according to the international medical requirements [1, 5] is needed The 6 MeV electron beam calibration was accomplished by absorbed dose and output factor determination The absorbed dose was measured first in the reference field and then it was determined for all accessible fields of dimensions ranging between 4 and 30 cm along OX and OY directions The results are given in Table 1 They indicate that for given field dimensions the absorbed doses are different for interchanged sizes

The output factors summarised in Table 2 were obtained as ratio between the absorbed doses in different extended fields and the absorbed dose in the 10x10 cm reference field One remarks that the output factor for a xxy field has not the same value with that of the Table 2 yxx field This effect may be assigned to the fact that the two applicators in OX and OY directions are in different planes The output factors dependence on x respectively y dimension of the irradiated field are represented in Figures 1 and 2 for two particular cases The same dependences may be obtained for any other field dimensions combination

Table 1. The absorbed doses (in Gy) for different irradiated field surfaces.

y/x [cm]	4	5	6	7	8	9	10	12	15	18	20	25	30
4	2.946	3.101	3 214	3 308	3 384	3 446	3 499	3 552	3 598	3.637	3 664	3 707	3 731
5	3 124	3 329	3 319	3 444	3 526	3 597	3 641	3 729	3 785	4 307	3.832	3 925	3 959
6	3 339	3 524	3 624	3 699	3.829	3 812	3 906	3.967	3 995	4 o6	4 08	4 12	4 158
7	3 675	3 638	3 823	3.915	3 995	4 029	4 095	4 176	4 235	4.267	4 31	4 422	4 413
8	3 636	3 806	3 953	4 041	4 13	4 18	4 248	4 331	4 378	4 413	4.455	4 565	4 548
9	3 721	3 913	4.004	4 138	4 219	4 298	4 331	4 341	4 378	4.499	4 529	4.67	4 678
10	3 847	4 053	4 18	4 285	4 375	4 455	4.522	4 575	4 636	4 685	4 742	4.79	4.839
12	3 973	4 18	4 323	4 434	4 52	4 596	4 655	4 718	4 78	4 839	4 901	4.959	5 021
15	4 106	4 268	4.409	4.512	4 619	4 702	4 775	4 854	4 921	4 976	5 044	5.097	5 149
18	4.293	4 417	4.544	4 635	4 733	4 807	4 873	4 96	5 026	5 101	5 14	5.226	5 266
20	4 211	4 426	4.556	4 682	4.781	4.846	4 923	5 001	5 08	5 137	5 201	5 275	5 331
25	4 338	4 559	4 699	4 821	4.93	5 024	5 099	5 18	5 259	5 322	5 38	5 469	5 495
30	4 477	4.67	4 841	4 946	5 068	5 156	5.254	5 305	5 404	5 465	5 551	5 649	5 686

Table 2. The output factor, f, for different irradiated field surfaces

y/x [cm]	4	5	6	7	8	9	10	12	15	18	20	25	30
4	0 6515	0.6858	0 7107	0.7315	0 7483	0 7621	0 7738	0 7855	0.7957	0 8043	0 8103	0 8198	0.8251
5	0 7121	0 7375	0 7618	0 7828	0 801	0 8167	0 8308	0 845	0 8582	0 8706	0.8797	0.8892	0 8967
6	0 7596	0.8005	0.8226	0 8392	0 8569	0.8709	0.885	0 8985	0 9091	0 9191	0 9279	0 9368	0.9407
7	0 8339	0.8523	0 9711	0 887	0 9047	0 9188	0 9334	0 9447	0.9578	0 9693	0 9788	0 9881	0 9971
8	0 8253	0 8629	0 8932	0 9149	0 9345	0 9509	0.9628	0 979	0 9894	1 0015	1 0108	1 0219	1 027
9	0 8441	0.8866	0 9155	0 9363	0 9564	0 9717	0.9812	0 9923	1 0049	1 0161	1 0316	1 0429	1 0557
10	0 8507	0 8963	0 9244	0 9476	0 9675	0 9852	1	1 0117	1 0252	1 036	1.0487	1 0593	1 0701
12	0 8786	0 9244	0 956	0.9805	0 9996	1 0164	1 0294	1 0433	1 0571	1 0701	1 0838	1 0966	1.1103
15	0 908	0 9438	0.975	0 9978	1.0215	1 0398	1 0559	1 0734	1 0882	1 1004	1.1154	1 1272	1 1387
18	0 9494	0 9768	1 0049	1.025	1 0467	1 063	1 0776	1.0969	1.1115	1 128	1 1367	1 1557	1 1645
20	0 9312	0 9788	1 0075	1.0354	1 0573	1 0716	1 0887	1.1059	1 1234	1 136	1.1502	1 1665	1 1789
25	0 9593	1 0082	1.0391	1 0661	1 0902	1 111	1 1676	1 1455	1 163	1 1769	1 1897	1.2094	1 2152
30	0.99	1 0327	1 0705	1 0938	1.1207	1 1402	1 1619	1 1732	1.195	1 2085	1 2276	1 2492	1.2574

Table 3

x (y) [cm]	4	5	6	7	8	9	10	12	15	18	20	25	30
a	1°24'	1°45'	2°6'	2°27'	2°48'	3°9'	3°30'	4°12'	5°15'	6°18'	7°	8°43'	10°
b	1°27'	1°49'	2°11'	2°33'	2°55'	3°16'	3°39'	4°22'	5°28'	6°33'	7°6'	8°4'	10°5'

One remarks from the shape of these curves that the absorbed doses are increasing with the irradiated field dimension, but for large values of the field dimensions the absorbed doses

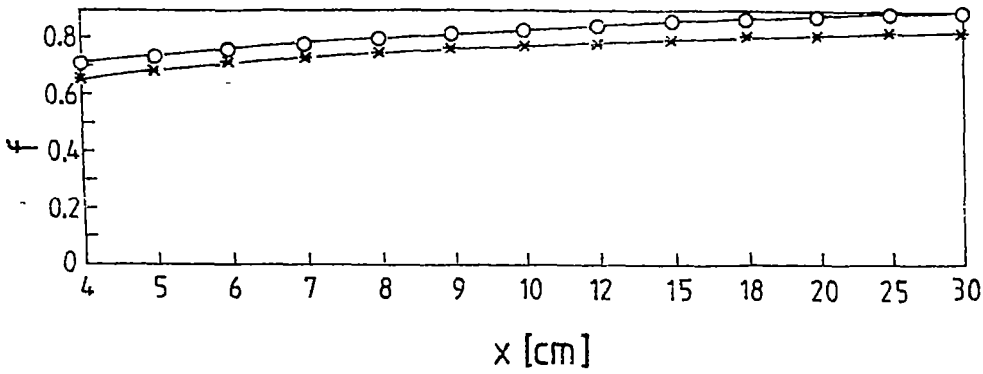

Fig.1 Output factor dependence on the x dimension of the irradiated field for y = 4 cm (*) and y = 5 cm (o)

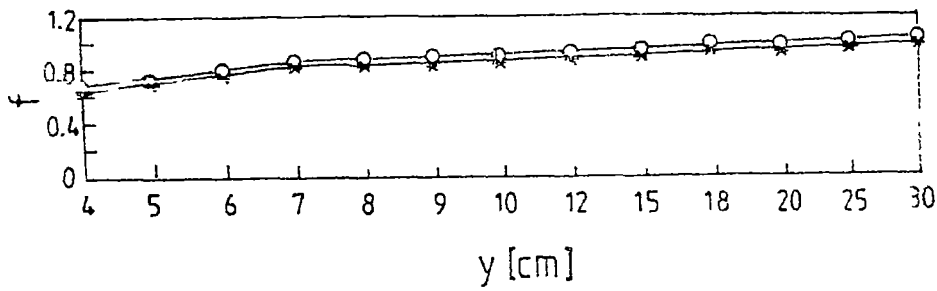

Fig.2 Output factor dependence on the y dimension of the irradiated field for x = 4 cm (*) and x = 5 cm (o)

remain practically unmodified. These results could be explained by he fact that as the field dimension exceeds the electrons path, for the considered electron beam, the electrons which are the furthest scattered relative to the dose measurement point do not contribute to the absorbed dose in that point Consequently the dose in a given point cannot exceed a certain limit by increasing of the irradiated field dimensions

Conclusions. The results obtained in this study are applied in the radiotherapy with 6 MeV electron beam provided by a GE Saturn 41 linear accelerator The experimental data evidence an asymmetry of the output factors for irradiated fields of same surface but of different dimensions The asymmetry is determined by the electron scattering on the

additional applicators One also observes that the absorbed dose in a certain point of the irradiated surface has a upper limit regardless of the irradiated field dimensions increase

REFERENCES

1 ICRU, *Radiation Dosimetry Electron Beams with Energies between 1 and 50 MeV*, Report 35, Bethesda, 1984

2 IAEA, *Absorbed Dose Determination in Photon and Electron Beams*, Report 277, Vienna, 1, 1987

3 F H Attix, *Introduction to Radiological Physics and Radiometry*, AWiley -Interscience Publication, J Wiley & Sons, New York Chichester Brisbane Singapore,1986, p 114

4 A Brahme, *Design Principles of Therapeutic Electron and Photon Beams*,Karolinskaia Institute, Stokholm, 1982, p 36

5 J R Horan, Health Physics, 52, 2, 141 (1990)






În cel de al XL-lea an (1995) *Studia Universitatis Babeș-Bolyai* apare în următoarele serii:

matematică (trimestrial)
fizică (semestrial)
chimie (semestrial)
geologie (semestrial)
geografie (semestrial)
biologie (semestrial)
filozofie (semestrial)
sociologie-politologie (semestrial)
psihologie-pedagogie (semestrial)
științe economice (semestrial)
științe juridice (semestrial)
istorie (semestrial)
filologie (trimestrial)
teologie ortodoxă (semestrial)
educație fizică (semestrial)

In the XL-th year of its publication (1995) *Studia Universitatis Babeș-Bolyai* is issued in the following series:

mathematics (quarterly)
physics (semesterily)
chemistry (semesterily)
geology (semesterily)
geography (semesterily)
biology (semesterily)
philosophy (semesterily)
sociology-politology (semesterily)
psychology-pedagogy (semesterily)
economic sciences (semesterily)
juridical sciences (semesterily)
history (semesterily)
philology (quarterly)
orthodox theology (semesterily)
physical training (semesterily)

Dans sa XL-e année (1995) *Studia Universitatis Babeș-Bolyai* paraît dans les series suivantes:

mathematiques (trimestriellement)
physique (semestriellement)
chimie (semestriellement)
géologie (semestriellement)
géographie (semestriellement)
biologie (semestriellement)
philosophie (semestriellement)
sociologie-politologie (semestriellement)
psyhologie-pédagogie (semestriellement)
sciences économiques (semestriellement)
sciences juridiques (semestriellement)
histoire (semestriellement)
philologie (trimestriellement)
théologie orthodoxe (semestriellement)
éducation physique (semestriellement)

CONTENTS

43 904